THE EFFECTS OF MICROSTRUCTURE ON THE MECHANICAL PROPERTIES OF HARD TRANSITION METAL SILICON NITRIDE NANOCOMPOSITE COATINGS

by

JESSICA MOONEY

Presented to the Faculty of the Graduate School of

The University of Texas at Arlington in Partial Fulfillment

of the Requirements

for the Degree of

DOCTOR OF PHILOSOPHY

THE UNIVERSITY OF TEXAS AT ARLINGTON

DECEMBER 2013

Acknowledgements

I would like to graciously thank Dr. Efstathios I. Meletis, who advised this work. Without his guidance, the results presented in this document could not have been obtained. I would also like to thank my committee members, Dr. Aswath, Dr. Jiang, Dr. Liu, and Dr. Luo for providing additional guidance and for taking the time to involve themselves in my work.

I'd like to acknowledge and thank the National Science Foundation's Louis Stokes Alliance for Minority Participation (LSAMP) for funding this work for 2 years from 2010 through 2012, as well as for providing career development tools and workshops, a generous living stipend, and conference travel allowances, serving to greatly enhance my graduate education experience.

Each and every one of my lab mates receives thanks for their advice, assistance, training, and camaraderie during my time as a graduate student. Special thanks go to Jie He and Minghui Zhang for their assistance with the TEM work presented in this work, Adam Smith for his assistance and training with the Nano-Indenter, Yishu Wang for his assistance with XPS, and Anna Zaman for her help and scientific curiosity with the TaSiN work.

Additional thanks are given to my family, and especially my husband for his constant support throughout the course of my graduate studies.

November 23, 2013

Abstract

THE EFFECTS OF MICROSTRUCTURE ON THE MECHANICAL PROPERTIES OF HARD TRANSITION METAL SILICON NITRIDE NANOCOMPOSITE COATINGS

Jessica Mooney, PhD

The University of Texas at Arlington, 2013

Supervising Professor: Efstathios I. Meletis

In this body of work, the examination of two different transition metal silicon nitride (MeSiN) systems using two different methods of physical vapor deposition (PVD) allowed for the development of a detailed understanding between the processing conditions, the micro-scale and nano-scale morphology, and the mechanical properties of the as-deposited thin film nanocomposite coatings. TiSiN coatings processed using the high-energy Arc deposition technique had hardness values of up to 33.6 GPa, and a previously unidentified (TiSi)N FCC crystalline phase, likely present due to the amounts of energy employed during coating processing, was discovered via intensive low angle X-Ray diffraction (XRD) and high resolution transmission electron microscopy (HRTEM) study. Coating morphology was columnar, and the presence of nano-scale subgrains within the columns was established, with increasing Si content within the coatings serving to reduce and refine both column and subgrain microstructure.

TiSiN coatings prepared in the Surface and Nano Engineering Laboratory (SaNEL) via reactive PVD magnetron sputtering had even more impressive mechanical properties, with refinements to deposition parameters and the coating microstructure

yielding thin film materials up to 38.9 GPa in hardness. Relationships between the preferred orientation, the presence of the (TiSi)N FCC crystal structure, the hardness, and the residual stress of the coatings were discovered and explored in detail, with the overwhelmingly present trend of higher hardness and higher degree of (200) FCC texturing being correlated with lower residual stresses and less prominent presence of Si incorporation into the FCC TiN crystal lattice. Morphology was again columnar, with nano-scale subgrain presence detected within the columns.

The knowledge gained via the study of the TiSiN system was used to select initial processing conditions for another type of MeSiN coating, TaSiN. Initial coatings possessed hardness ranging from 20-25.5 GPa, and displayed excellent oxidation resistance after ambient air annealing at 550˚C. Continued study of this system is ongoing, but preliminary recent results suggest that the refinement of the structure to include a combination of FCC, hexagonal, and orthorhombic TaN crystalline phases serves to increase TaSiN coating hardness to levels of approximately 33 GPa.

Table of Contents

List of Figures

List of Tables

Chapter 1

Introduction

1.1 Introduction and Motivation

Materials for use in extreme environments have attracted significant scientific attention for decades. Of particular interest are coating materials displaying high hardness and ability to resist oxidation at elevated temperatures. Special attention has been applied to transition metal silicon nitride systems. In one such system, TiSiN, theoretical modeling suggests that hardness of 100 GPa is possible with a two phase composite system of nanocrystalline TiN and amorphous Si_3N_4. [1-9] Pioneer work by Veprek suggests that such incredible hardness can be achieved with the presence a single monolayer of the amorphous Si_3N_4 phase surrounding nano-scale crystalline TiN grains. [2-4, 6, 7, 10-13] While Veprek's nc-TiN/a-Si_3N_4 model is frequently cited in the literature in the discussion of high hardness films, a lack of detailed TEM analysis is reported. Such analysis is imperative to gain a clear understanding of the relationship between hardness and detailed microstructural characteristics and to test Veprek's proposed nc-TiN/a-Si_3N_4 structure. In addition to high hardness, TiSiN nanocomposite coatings are able to withstand oxidation at higher temperatures than single phase TiN coatings; the addition of an amorphous Si_3N_4 phase has been shown to increase the oxidation temperature from 400˚C to about 600˚C. [14] While this improvement in oxidative resistance is significant, the performance of TiSiN films in terms of high temperature oxidation resistance is still lacking current technological needs.

Recent evidence shows that Ta, another transition metal, has the potential to allow for high temperature oxidation resistance when incorporated into transition metal silicon nitride coatings. [11, 15-19] While early TaSiN coatings were nearly completely amorphous and were used as diffusion barriers in electronics, more modern iterations of

this material consisting of a combination of nanoscale crystalline and amorphous phases have been shown to be resistant to oxidation at very high temperatures. TaSiN coatings with high amorphous content have been tested at temperatures up to 1350˚C. They display superior oxidation resistance with no significant weight gain due to oxidation, but these coatings lack the enhanced hardness present in TiSiN coatings. [14, 15, 20] Detailed microstructural analysis is needed to gain a better understanding of the relationship between the microstructue of TaSiN composite coatings and their properties. This study will help to advance the knowledge of the challenges which exist in the effort to develop nc-TaN/a-Si_3N_4 coatings with a monolayer-thick amorphous phase. Such application of Veprek's model of hardness enhancement to the TaSiN system has the potential to create revolutionary coatings with both high hardness and excellent high temperature properties.

1.2 Research Objectives

TiSiN shows great promise as a high hardness coating, but its high temperature oxidation properties are not satisfactory above temperatures of approximately 600-800˚C. The TaSiN system, on the other hand, has lower values for hardness but displays excellent oxidation resistance at temperatures exceeding 1350˚C. TiSiN will be used as a model system to gain a fundamental understanding of the relationship between morphology and film properties within the nc-MeN/a-Si_3N_4 system (where Me is a transition metal), and this knowledge will be applied to the TaSiN system to investigate the potential for coatings for use in extreme environments displaying both enhanced hardness and superior resistance to oxidation at elevated temperatures. Methods used to produce MeSiN coatings include Chemical Vapor Deposition (CVD) and Physical Vapor Deposition (PVD). PVD methods include techniques such as evaporation, arc deposition, and magnetron sputtering. [3-5, 7, 11] It has been established that PVD

methods such as magnetron sputtering are capable of producing coatings with high levels of purity and refined microstructure.

The specific objectives of this study are:

1. Gain fundamental knowledge of the relationship between microstructure and properties of PVD TiSiN films (arc and magnetron sputtered).
2. Use the knowledge gained with the TiSiN system to investigate another high potential transition metal silicon nitride film, TaSiN, with the overall goal of developing the fundamental knowledge to synthesize advanced hard, high temperature resistant coatings.

1.3 Dissertation Overview

This dissertation consists of seven chapters. The following is an outline and brief summary of each chapter included in this document.

Chapter 1, Introduction: This chapter introduces the main motivations and objectives behind the work, as well as providing a brief introduction to the current knowledge in the state of MeSiN coatings.

Chapter 2, Literature Review: This chapter gives detailed background information on the current works published in terms of processing conditions and mechanical properties of MeSiN coatings, as well as offering a detailed review of the Magnetron Sputtering PVD process used to synthesize TiSiN and TaSiN coatings.

Chapter 3, Thin Film Synthesis and Characterization: This chapter describes the process by which films were deposited using two different processes: Arc Sputtering, and PVD Reactive Magnetron Sputtering. In addition, details are provided regarding the

characterization methods and processes used including X-Ray diffraction (XRD), nano-indentation, high resolution transmission electron microscopy (HRTEM), X-Ray photoelectron spectroscopy (XPS), tribometry, and surface optical profilometry.

Chapter 4, Microstructure and Property Investigation of Arc Deposited Titanium Silicon Nitride Coatings: This chapter describes a portion of the collaboration with Cheng et al. A detailed study of the microstructure of TiSiN films with low and high Si content were explored using HRTEM, nano-indentation, and XRD. The relationships of properties such as grain size, grain boundary definition, and mechanical properties are discussed.

Chapter 5, Relationship of Microstructure and Mechanical Properties in PVD Magnetron Sputtered Titanium Silicon Nitride Thin Films: Detailed analysis of TiSiN films produced at the Surface and Nano Engineering Laboratory are presented in this chapter. Mechanical properties such as hardness, residual stress, and wear resistance are examined with respect to processing conditions and microstructure properties such as crystalline phases present, grain size, and morphology, as studied by TEM.

Chapter 6, Relationship of Microstructure and Mechanical Properties in PVD Magnetron Sputtered Tantalum Silicon Nitride Films: TaSiN films processed using similar parameters as those discovered in the TiSiN study to produce high hardness films were examined. Results correlating processing conditions, mechanical properties, and microstructure are presented in this chapter, as well as results from a preliminary oxidation study.

Chapter 7, Conclusions: Findings throughout the study regarding the nanoscale morphology and the mechanical properties of the coatings are summarized in this chapter.

Chapter 2

Literature Review

The search for appropriate materials to fulfill evolving needs for tools, weaponry, and technology has occurred throughout human history. The engineering of new materials is one of the oldest recorded applications of science, and historical periods such as the stone age, the bronze age, the iron age, and the steel age are even named for the class of material which dominated the technological advances of the era. In modern materials science, composite materials and nano-scale materials have gained attention for the development of a vast array of new material with applications including but not limited to the miniaturization of electronics, the development of high-tech biomaterials, and the creation of materials for use in extreme environments. In particular, the search for coating materials having excellent mechanical properties for use at high temperatures has made use of technology in both composite and nanoscale materials science and remains a fascinating area for future study and advancement of the knowledge of high hardness coatings.

2.1 Intrinsically Hard Materials

The hardness of a material is defined by its ability to resist plastic deformation upon mechanical loading. Crystalline, intrinsically hard materials such as cubic boron nitride (c-BN) and diamond, with hardness of > 46 GPa and >70 GPa respectively, achieve high hardness due to strong covalent bonding and high coordination number in all three directions. [21] Cubic boron nitride is a man-made material which is easily manufactured using sintering processes. It is frequently used in abrasive applications.

Diamond has a coordination number of 4 and is made up of strong, nonpolar, covalent bonds. It is a metastable, high pressure, high temperature carbon based

material. [22] Although diamond is the hardest known intrinsically hard material, it has severe limitations including high cost and oxidation at temperatures above 800˚C. [23]

Although leading experts in the field believe that diamond will remain the most intrinsically hard material, much effort has been devoted to the processing and understanding of new, high-hardness materials, especially for use as tribological coatings. Therefore, much of the recent research in the field of high hardness coatings focuses on the development of thin film materials which can maintain their mechanical properties at high temperatures. In particular, Transition Metal Silicon Nitride (MeSiN) coatings have attracted particular interest due to their intriguing mechanical and thermal properties.

2.2 MeSiN Coatings

Tribological coatings are often applied in a thickness of no more than a few microns to tools or parts which will experience high amounts of friction and wear. The excellent mechanical properties of the tribological coatings help to protect the underlying surface from repeated applied mechanical damage. Titanium Carbide coatings were first developed in the 1960's, and were deposited by CVD. They became the earliest tribological coatings to gain widespread industrial use. [24] Less than 2 decades later, Titanium Nitride (TiN) coatings were developed via methods such as PVD and were quickly developed to become commercially available. While both TiC and TiN coatings remain relevant today as tribological coatings, significant efforts have been made to adjust the chemical composition, processing methods, and overall performance properties of these materials in order to fit a wide variety of materials application needs. [6, 18, 24-33]

2.2.1 Early improvements to Tribological Coatings

Shortly after the development of TiN as a tribological coating, variations on the composition and chemistry were developed to tailor the material properties as needed for various applications. Titanium Carbon Nitride (TiCN) coatings were developed to combine the good thermal and hardness properties of TiN coatings with the superior adhesion properties of TiC coatings. [24] Typically TiCN coatings display about 80% higher hardness as compared to TiN, as well as a reduced coefficient of friction. Both of these properties improve the overall utility of the material as a tribological coating. [34-37] Additional improvments were made with the introduction of TiAlN coatings, which raised the oxidation resistance by approximately 200˚C, as compared to the previous TiN coatings. [14, 38, 39] Other advancements to the field of tribological coatings for use in extreme enviroments have included but are not limited to TiBCN, SiBCN, TiAlN/CrN, as well as various transition metal nitrides and multilayer composites with transition metals such as Ti, Zr, Cr, W, Ta, Mo, and Nb. [16, 26, 28, 38, 40-45]

2.2.2 Mechanism of Hardness Enhancement in TiSiN Coatings

Transition metal nitrides such as TiN have a reported hardness of 18-21 GPa, and they can resist oxidation to temperatures of approximately 500˚C. [15, 16] More recently, Si has been incorporated into TiN coatings, resulting in both increased hardness and increased oxidation resistance. In fact, TiSiN coatings have reported hardness in the range of 40-50 GPa, and they are capable of resisting oxidation at temperatures reaching 650-700˚C. [13, 15, 16, 46-49] It is believed that this hardness enhancement is a result of a combination of factors including Si refining the crystalline structure, helping to induce a nanoscale morphology, as well the ability of the amorphous Si_3N_4 at the grain boundaries to effectively trap dislocations within the material. [23, 27, 38, 50-52]

2.2.2.1. Hardness Enhancement due to Nanoscale Morphology

Materials such as transition metal nitrides which are not intrinsically hard can see significant enhancement of their mechanical properties with the manipulation of their grain size and morphology. According to the Hall Petch relation, hardness increases with decreasing grain size for single phase materials within the micro and nano-scale regime, until the grain size reaches a diameter of about 10 nm. At this point, there is a sharp drop off in hardness with further decrease in grain size. This relationship can be seen in Figure 2-1. While Hall Petch traditionally applies to single phase materials, the concept has also proven useful in the study of composite coating materials. [3, 4, 6, 7, 11] In transition metal silicon nitride coatings with nanoscale grain size, the amorphous Si_3N_4 grain boundary phase contributes highly to the material properties. It is thought that a single atomic monolayer of this amorphous phase may actually enhance the hardness, since a dislocation formed in the nano-crystalline component of the material cannot propagate into the amorphous phase. [1, 3-5, 53]

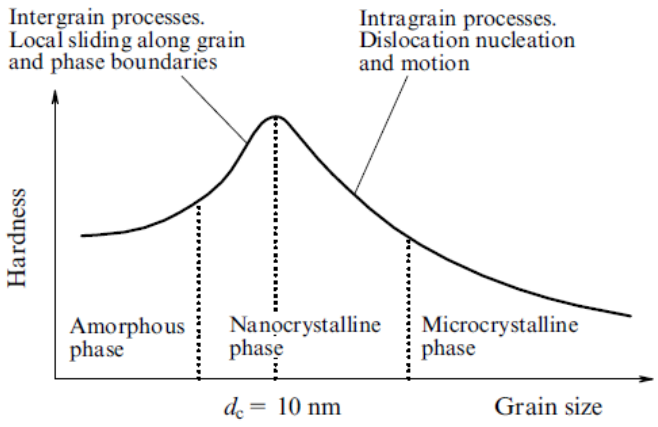

Figure 2-1 Hall Petch Relationship between hardness and grain size

A basic understanding of the relationship between deposition techniques and film morphology for single phase materials is presented in Thornton's classical work. Thornton shows a clear relationship between the grain morphology in PVD coatings, the working pressure during deposition, and the ratio of the substrate temperature during deposition to the melting temperature of the compounds being deposited (T/T_m), Figure 2-2. [54, 55] The incorporation of additional elements and the formation of a second phase has been found to cause further grain structure refinement and lower T/T_m ratios. In addition, applying a substrate bias results in bombardement with a more energetic plasma that can even further reduce the processing temperature and cause microstructure refinement. In fact, work within the TiSiN system suggests that a temperature of at least 550˚C, a high N_2/Ar ratio, and a low working pressure are all necessary to achieve the nanocomposite morphology associated with hardness enhancement. [3, 6, 11]

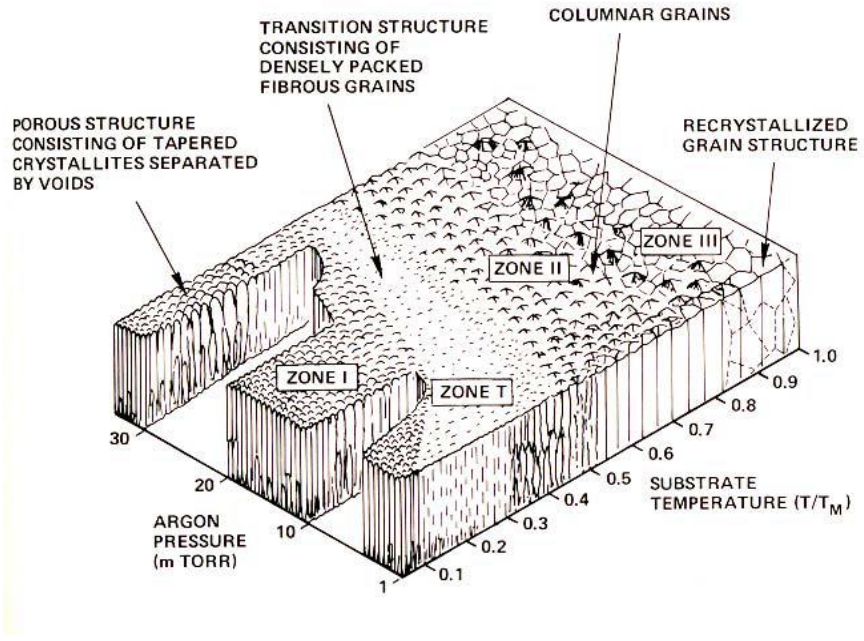

Figure 2-2 Model relating deposition conditions to film morphology [54, 55]

Pioneer work in this field by Veprek suggests that this mechanism of hardness enhancement is due to a spinodal decomposition that occurs during phase seperation within the ncTiN/Si_3N_4 system, resulting in spontaneous nucleation of TiN grains with nanoscale dimensions of typically 8-10 nm in diameter surrounded by a single monolayer of amorphous Si_3N_4, Figure 2-3, instead of the typical columnar structure. [1, 13, 48]

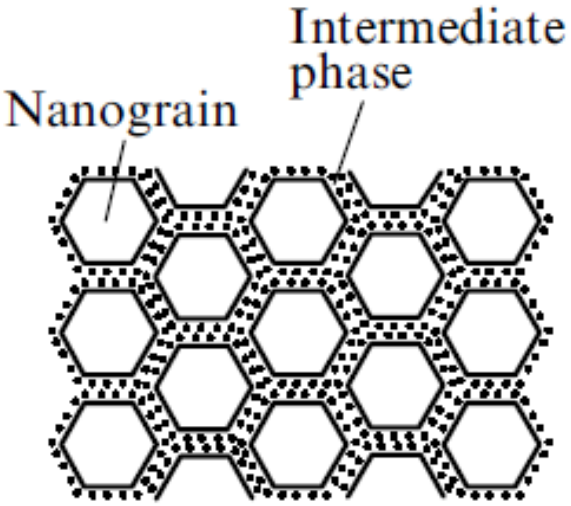

Figure 2-3 Schematic diagram showing the proposed structure of nc-TiN/a-Si_3N_4 with an amorphous monolayer between nanoscale TiN grains [48]

It is believed that with sufficiently high deposition temperature of 500-550˚C, this nanoscale morphology is achieved by way of spinodal decomposition. Spinodal decomposition was first suggested by van der Waals, and it refers to the situation in which the second derivative of pressure with respect to volume is negative. Thus, there is no barrier to nucleation in this type of transformation. This results in a system which is inherently unstable, and, the result is the rapid un-mixing of a solution consisting of two mixed phases with zero activation energy. This “uphill” diffusion will continue to take place, decreasing the total free energy of the system, until the equilibrium conditions (TiN and Si_3N_4 in this case) are reached. This is much different than typical methods of

nucleation of crystalline phases, which require overcoming a substantial initial free energy barrier in order for nucleation or initial grain growth to occur. In addition, nucleation may happen only a very few times, or possibly even only once, since the nucleation of additional grains may rapidly occur in the areas immediately surrounding the initial grain. Conversely, spinodal decomposition may occur continuously and simultaneously in different physical locations throughout the coating deposition process. This type of mechanism is known for producing materials typically consisting of very fine grains, which have been shown to enhance the mechanical properties of the material.

Figure 2-4 on page 12 shows the theoretically calculated chemical spinodal for TiSiN deposited at 600˚C. In methods such as CVD or PVD Magnetron sputtering, where the flux of the Ti, Si, and N atoms to the substrate surface are random, a solid solution is believed to form in the initial stages. [13, 50, 51, 56] If the deposition temperature is sufficiently high as to allow the spinodal decomposition proposed in the literature, then the formation of a strong nanocomposite structure will occur during the coating deposition process. It has been shown that this decomposition is kinetically controlled by bulk diffusion, since the decomposition of the mixed phases is faster than Si diffusion. [6, 12, 13, 25, 31, 56] The formation of the two distinct phases via this mechanism should result in equi-axed nano-scale crystalline regions with clearly defined grain boundaries.

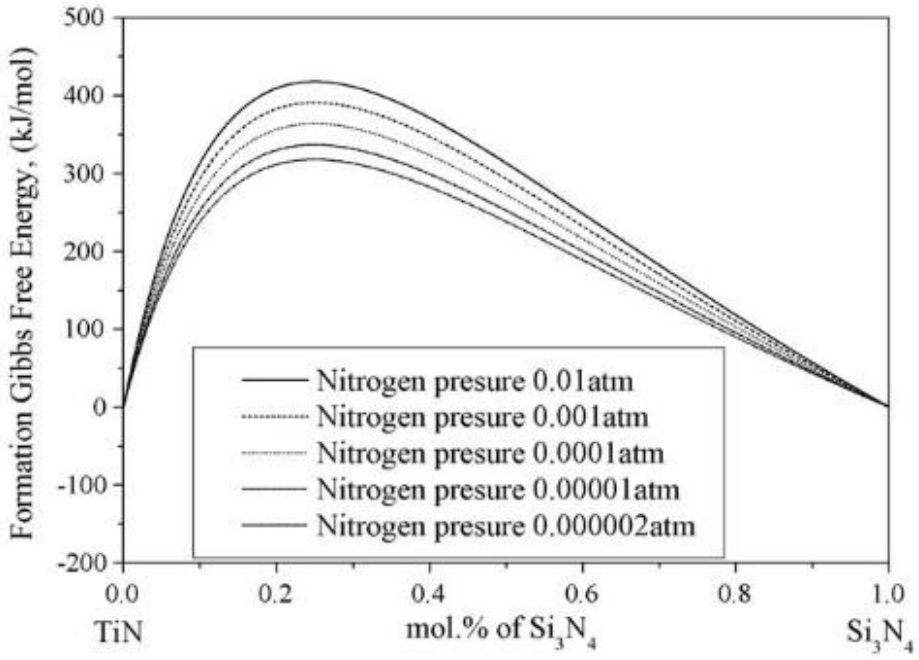

Figure 2-4 Chemical Spinodal of the TiSiN system at 600˚C for various pressures of N_2 gas [1, 48]

2.2.2.2 Hardness Enhancement due to Si content

In addition to grain size, Si content is also a key factor in coating hardness. The approproate Si content to achieve this single layer around each TiN grain is reported to be between 5-12 at %, although the exact amount varies dependinding on the average grain size. [7, 57-61]. This relationship can be seen in Figure 2-5 on page 13.

Several reports in the literature have claimed to achieve the previously mentioned nc-TiN/a-Si_3N_4 microstructure. In fact, reported hardness of over 40 GPa via CVD [11] and over 50 GPa via PVD have been reported, See Table 2-1 on page 13. [11, 62]

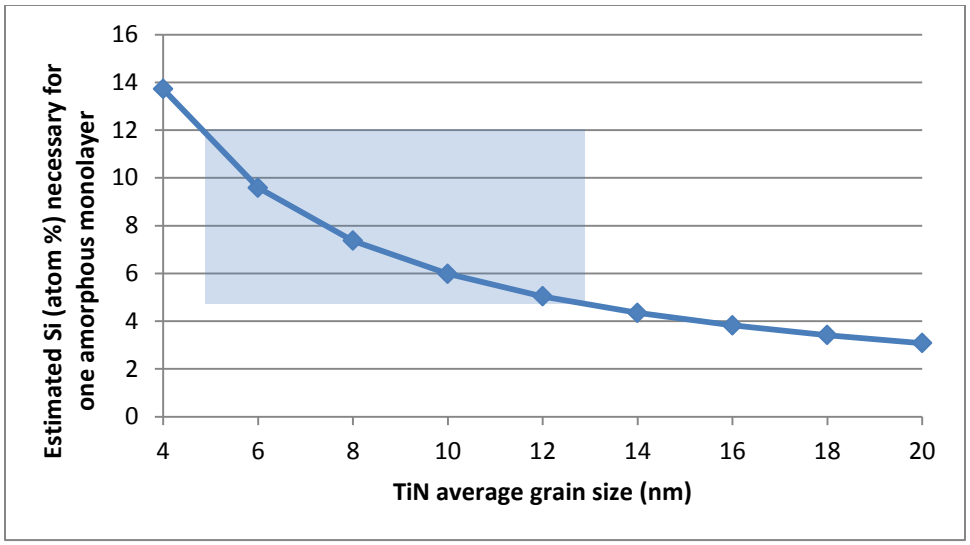

Figure 2-5 Estimated necessary Si content (at %) in order to form a monolayer of amorphous Silicon Nitride layer surrounding each TiN grain, as it varies with TiN grain size, where the shaded region represents the range of desired Si content and TiN grain size

Table 2-1 Literature review of hardness of TiSiN PVD films

Hardness (GPa)	Deposition Method	Author	Year	Reference
30	Reactive Magnetron Sputtering	Prochazka, et al	2004	[48]
37	RF Sputtering	Nose, et al	2003	[59]
38	DC Magnetron Sputtering	Kim, et al	2002	[62]
40	DC Magnetron Sputtering	Ribiero at al	2004	[29]
50	Arc Sputtering	Cheng et al	2008	[46, 63]

However, in certain cases these films may contain additional, undesirable phases. For example, ternary systems such as the nc-TiN/a-Si_3N_4/a-$TiSi_2$ and quaternary systems such as nc-TiN/a-Si_3N_4/a-$TiSi_2$/nc-$TiSi_2$ may show extremely high hardness, but these ternary and quaternary systems display lower resistance to oxidation and lower

thermal stability. [11] In addition, these ternary and quaternary TiSiN compounds are prone to Oswalt ripening over time, resulting eventually in a coarser grain structure and reduced coating hardness. [21] Other sources mention the formation of crystalline TiSiN phases in which Si atoms replace Ti atoms within the FCC TiN lattice. [9, 46, 60, 63-65] While many TiSiN films of high hardness are reported in the literature, a lack of comprehensive TEM analysis exists to investigate the microstructure responsible for these desirable enhancements in material properties. In addition, reports do not currently exist for the production and study of TiSiN films produced via magnetron sputtering at low deposition pressure (5 mTorr), high temperature (550˚C), and varying substrate bias. Such analysis is necessary to understand the mechanism of hardness enhancement at the atomic scale and to shed more light on the behavior of the proposed nc-TiN/a-Si_3N_4 microstructure. [46, 60]

2.2.3 Oxidation Resistance in MeSiN Coatings

While the TiSiN system shows extraordinary ability as a high hardness coating, the thermal stability and oxidation resistance of this material are not sufficient for high temperature applications. On the other hand, TaSiN coatings are of particular interest due to their ability to resist oxidation at elevated temperatures, up to at least 1350˚C. [15, 16, 20] A comparison of the high temperature resistance of many different types of coatings is shown in Figure 2-6 on page 15. [15, 16] While a small increase in mass is noted at 1100˚C, the TaSiN coating does not undergo the rapid increase in mass associated with oxidation as the other films do. Instead, after a small initial increase in mass, the film remains stable up to the maximum temperature tested, 1350˚C. [14, 15]

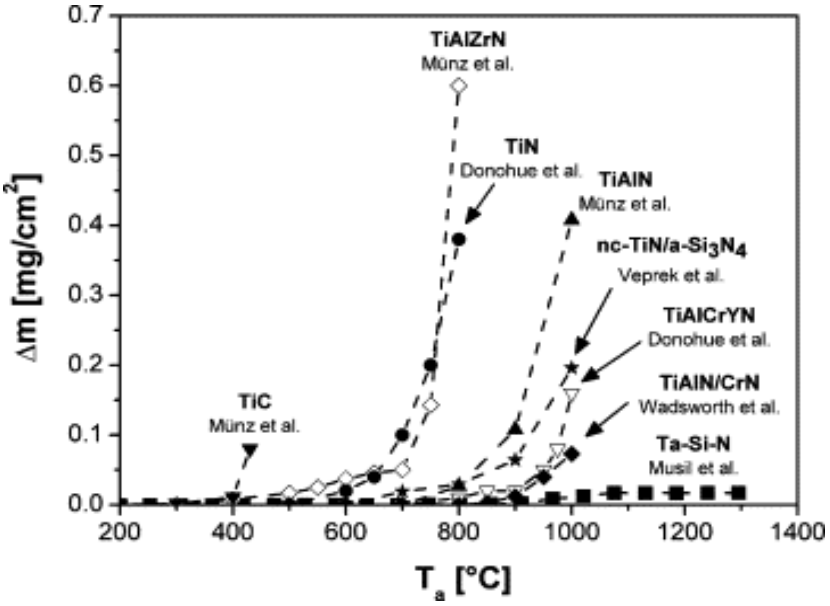

Figure 2-6 Oxidation resistance of various high temperature coatings

[33]

The proposed mechanism for oxidation of amorphous TaSiN coatings with high Si content suggests that at 1100˚C, Oxygen diffuses and reacts with Ta, forming a stable, passive tantalum oxide layer of a few hundred nanometers in thickness at the film surface. This oxide layer acts as a barrier to subsequent oxidation. At 1300˚C, XRD shows the formation of oxides, and there is a clear change in the morphology of the film's surface after annealing to 1300˚C, but the film remained mechanically intact. [18, 66, 67] Cross sectional SEM micrographs from this study can be seen in Figure 2-7 on page 16.

Most publications report the TaSiN system as either completely amorphous or as a mixed system composed of Ta-Si, Ta-N, and Si-N compounds. [15, 68, 69] Some compounds tend to crystallize such as TaN_x and $TaSi_x$, and others such as Si_3N_4 and SiN_x are amorphous. [15, 68, 69] Reported TaSiN systems displaying high temperature oxidation stability have a much higher amorphous content than the TiSiN system, and

films with Si content greater than 40 at % exhibit the highest resistance to oxidation, but these high amorphous content films have hardness values less than 30 GPa. [15-17, 47]

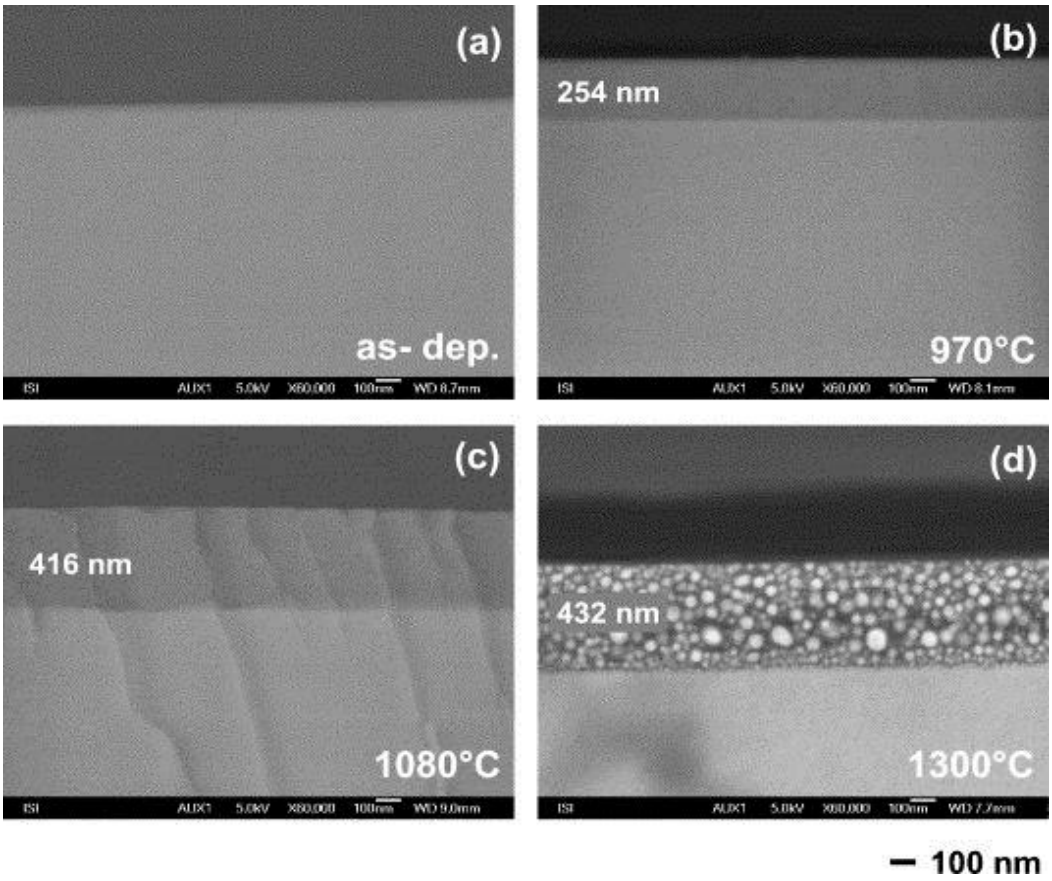

Figure 2-7 Formation of an oxide layer on high Si content TaSiN film surface at various annealing temperatures (a) as deposited, (b) 970˚C, (c) 1080˚C, (d) 1300˚C, all annealed in air. [15]

TaN however, is a compound which can achieve very high hardness values when deposited under the appropriate conditions. Tantalum nitride phases, when deposited via sputtering techniques, can vary greatly depending on the experimental synthesis conditions. Some compounds typically present using low N_2 flow and low substrate deposition temperature such as hexagonal Ta_2N have a theoretical hardness

value of only 15 GPa. Others present at higher N_2 flow and higher substrate temperature such as orthorhombic Ta_4N and FCC TaN have theoretical hardness values of 61 and 50 GPa, respectively, although other researchers have reported the FCC TaN phase in the range of 20 GPa based on experimental data. [70, 71] The hexagonal phase of TaN has been experimentally reported at values up to 39 GPa. [71] Comparatively, the hardness of TiN is about 20 GPa. Thus, a great potential for the development of new materials and coating for use in extreme environments is present. By applying the knowledge gained with the study of the nc-TiN/a-Si_3N_4 system, the development of new TaSiN materials not currently reported in the literature may be achieved. With decreased Si content and lower overall amorphous content within the film, it is possible that these materials might both mimick Veprek's proposed microstructure for hardness enhancement and achieve thermal stability and oxidation resistance at high temperatures.

2.3 Physical Vapor Deposition

PVD methods are commonly used in the manufacture of thin film coatings. There are three main categories of PVD, including evaporation, ion plating, and sputtering. Different varieties of each of the previously mentioned technologies have been developed for various coating applications. While the focus of this research is coatings prepared via PVD sputtering, it is important to point out that all forms of PVD share the following three basic steps in coating formation. First, the material(s) to be deposited must be put into a vapor phase. This can be accomplished via methods such as sputtering, evaporation, or other chemical vapors or gasses. Next, the vapor species must be transported to the substrate on which it is to be deposited. In the case of sputtering, this occurs through creation of a plasma containing the ionized atoms of the material to be sputtered as well as the ionized sputtering gas. The final step in all forms of PVD is the nucleation and growth of a film or coating on the substrate. [72]

2.3.1 PVD Magnetron Sputtering

Sputtering can be defined as the ejection of atoms or particles from a target or cathode via excitation from energetically excited particles which are at or near room temperature. [73] The ejection of target atoms during the sputtering procedure takes place in several steps. Free electrons present within the sputtering chamber will be accelerated away from the negatively charged cathode. Some of these electrons then collide with the gas sputtering species, such as Ar. The accelerated electrons eject an electron from the Ar atom at the point of the collision, resulting in an electron and an Ar^+ ion. The Ar^+ ions are then drawn towards the negatively charged cathode at an accelerated rate. When the Ar^+ ions strike the target, the target material is excited, and thus evaporated, through a physical momentum exchange. The ejected atoms or articles are then deposited onto a substrate or anode. [72] While this process is occurring, a number of free electrons and ejected electrons will collide with Ar^+ ions to form neutral Ar atoms. When the energized electron returns to a ground state, a photon is released in the reaction, thus resulting in the glow of light associated with plasmas. Since this process is physical in nature instead of chemical or thermal, a wide variety of materials can be coated or deposited via this method. A schematic of this phenomenon can be seen in Figure 2-8 on page 19.

Two main drawbacks associated with sputtering including slow deposition rate and a decline in quality of the deposited film can easily be averted with the use of magnetrons at the location of the target material. In magnetron sputtering, a magnetic field is applied at the cathode in order to help to increase both deposition rate and deposition quality. The applied magnetic field serves to “trap” electrons in a region directly above the cathode. This accomplishes two things. Having the electrons heavily concentrated in one region increases the number of collisions between electrons and Ar

atoms, thus increasing deposition rate of the target material. In addition, it ensures that the bombardment of the substrate surface with electrons is greatly reduced, thus enhancing the quality of coated films. [72, 73]

In magnetron sputtering, either a DC or an RF source may be applied to the cathode in order to produce coatings. In the case of metals, DC is typically used. For insulating materials however, RF may be used. In the case of either DC or RF sputtering, a number of different variations to the basic PVD magnetron sputtering process may be employed according to specific coating needs. Basic parameters which can affect

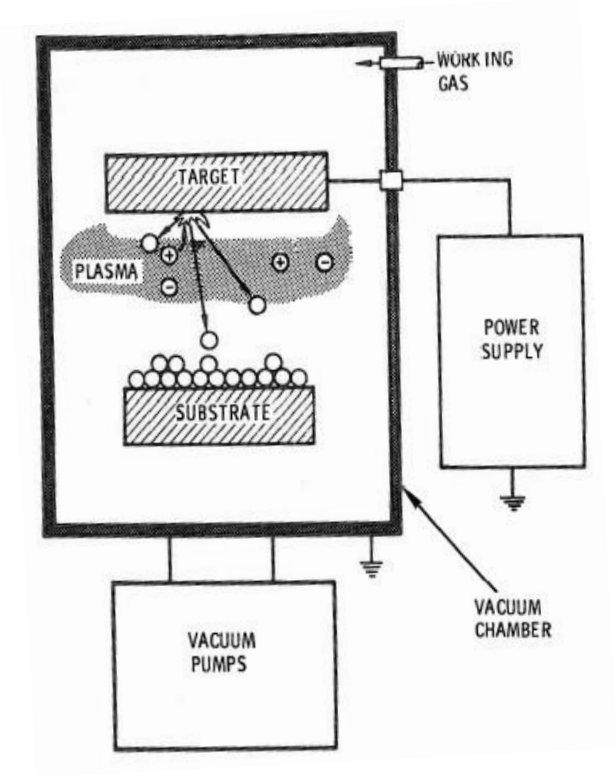

Figure 2-8 Schematic representation of sputtering system [68]

deposition rate, composition, and microstructure include but are not limited to target to substrate distance, power or voltage applied to the target(s), power or voltage applied to

the substrate, working pressure of the chamber during sputtering, flow rate of the sputtering gas or gasses, substrate temperature, and substrate rotation. Targets may consist of single elements or of compounds, and several targets can be used in unison or sequentially to obtain either an alloy film or a compositionally layered coating, respectively. Gasses such as O_2 or N_2 can be introduced into the chamber during a process called reactive sputtering to incorporate these atoms into the coating material. In addition, a bias applied to the substrate can encourage the bombardment of the substrate with ions during the deposition process; this can lead to re-nucleation events refining the microstructure, morphology, and composition of the coating. [72, 73]

Chapter 3

Thin Film Synthesis and Characterization

Preliminary TiSiN studies involved the characterization of coatings produced via Arc deposition method in collaboration with Cheng et al. [46, 60] These films were examined due to their high reported values of hardness to gain insight into the relationship between microstructure and mechanical properties. Further studies of TiSiN coatings involve synthesis via magnetron sputtering, followed by detailed characterization. Diffractive methods including XRD and HRTEM were used to gain a detailed understanding of the crystal structure and nanocrystalline morphology of the coatings as they relate to their properties. XPS was used to understand the composition and chemical states of the elements at or near the surface of the coatings. Nanoindentation, tribological wear testing, and optical profilometry aided in the understanding of the mechanical properties including the hardness, wear resistance, and coefficient of friction of the deposited coatings. Knowledge gained during the processing and characterization of TiSiN films that served as a model system was then used to deposit and study preliminary TaSiN coatings.

3.1 Synthesis of MeSiN Thin Films

The synthesis of MeSiN films was carried out with two deposition methods. First, a study in collaboration with Cheng et al was carried out on TiSiN deposited via Large Area Filtered Deposition (LAFAD) Arc Sputtering. These coatings were then analyzed in detail, with the goal of understanding the relationship between the morphology at the nanoscale and the high reported hardness of these coatings. Next, Reactive PVD Magnetron Sputtering was used to deposit MeSiN films including TiSiN and TaSiN, and to obtain films with desirable properties.

3.1.1 Large Area Filtered Deposition Arc Sputtering

A LAFAD system was use to deposit TiSiN coating of varying Si content. A schematic diagram can be viewed in Figure 3-1 on page 22. [64]. Two TiSi targets were placed on opposite ends of the plasma guide chamber, and deflecting coils located in the same plasma guide chamber were used to direct the ions 90° into the circular deposition chamber. Once the ions are steered into the chamber, a set of scanning focusing coils adjusts the surface area in the vertical direction for deposition onto the substrate. Concurrently, the arc column within the system is controlled in the horizontal direction by a magnetic field. This experimental setup leads to enhanced metal vapor ion yield and and suppression of turbulent plasma.

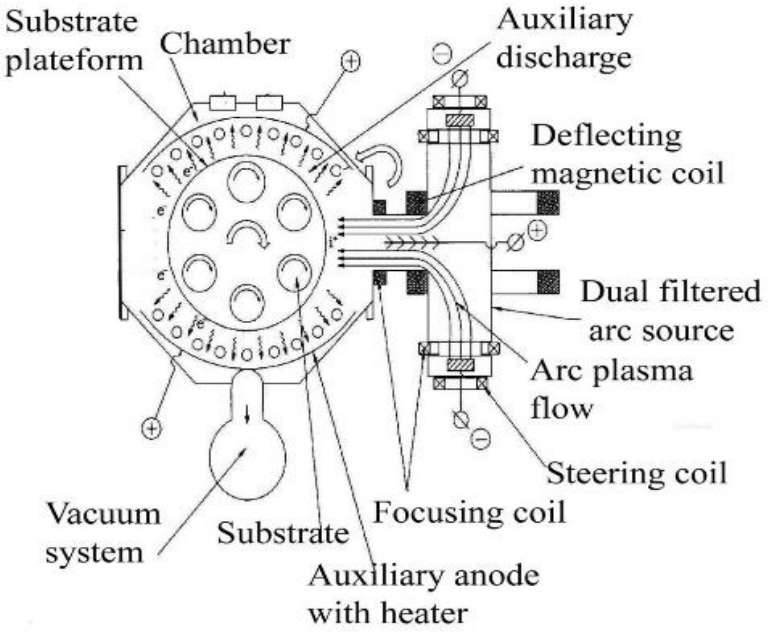

Figure 3-1 Schematic representation of the LAFAD Sputtering System used to deposit Arc TiSiN Low Si and High Si coatings

TiSiN coatings varying in Si content were deposited on 17-4 stainless steel substrates as described in [60]. TiSi targets with varying Si contents of 5%, 10%, 15%,

and 20% (at%) were used to control the Si content in the films, Figure 3-1(b), page 22. To improve the adhesion of the TiSiN coatings, a gradient layer of TiSi and TiSiN was deposited by increasing the N_2 content in the chamber gradually. This coating was deposited to a thickness of about 200 nm. Immediately following the gradient layer, TiSiN coatings were deposited with a thickness of 2-2.5 μm. A deposition pressure of 0.2 Pa, substrate bias of -40 V, and deposition temperature of 350 °C were the parameters used to deposit the coatings.

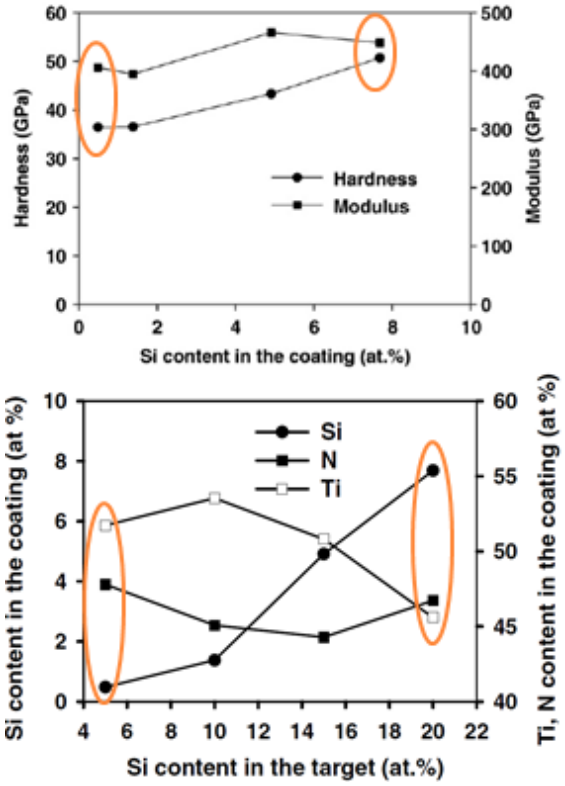

Figure 3-2 TiSiN coatings deposited via Cheng at al. a) Hardness and modulus as a function of Si content, b) atomic content as a function of TiSi target composition [28, 31-33]

The coatings created using the 5 wt% Si target (noted as low Si) and the 20 wt% Si target (noted as high Si) were selected for further analysis in this study in order to gain

an understanding of how the Si content and the associated changes in the microstructure contribute to the mechanical properties of these coatings. The variation of the mechanical properties as a function of Si including hardness and modulus can be seen in Figure 3-2(a) on page 23.

3.1.2 DC and RF Reactive Magnetron Sputtering

DC and RF Reactive Magnetron Sputtering was used to synthesize MeSiN thin films. Because this lab-built sputtering system in the Surface and Nano Engineering Laboratory (SaNEL) is very versatile and a large number of experimental parameters including pressure, gas mixture, power to the magnetron (DC and RF), substrate bias, substrate temperature, target material, distance between the target and substrate, and substrate rotation can easily be varied, samples with a wide array of material characteristics can be processed.

3.1.2.1 DC and RF Reactive Magnetron Sputtering System

MeSiN thin films were deposited using a home-built PVD Reactive Magnetron Sputtering System with DC and RF capabilities. A schematic diagram of this system including all power supplies, pumps, valves, heating, cooling, gas flow, and control elements is shown in Figure 3-3 on page 25, and a photograph of the system in the SaNEL laboratory is shown in Figure 3-4 on page 26.

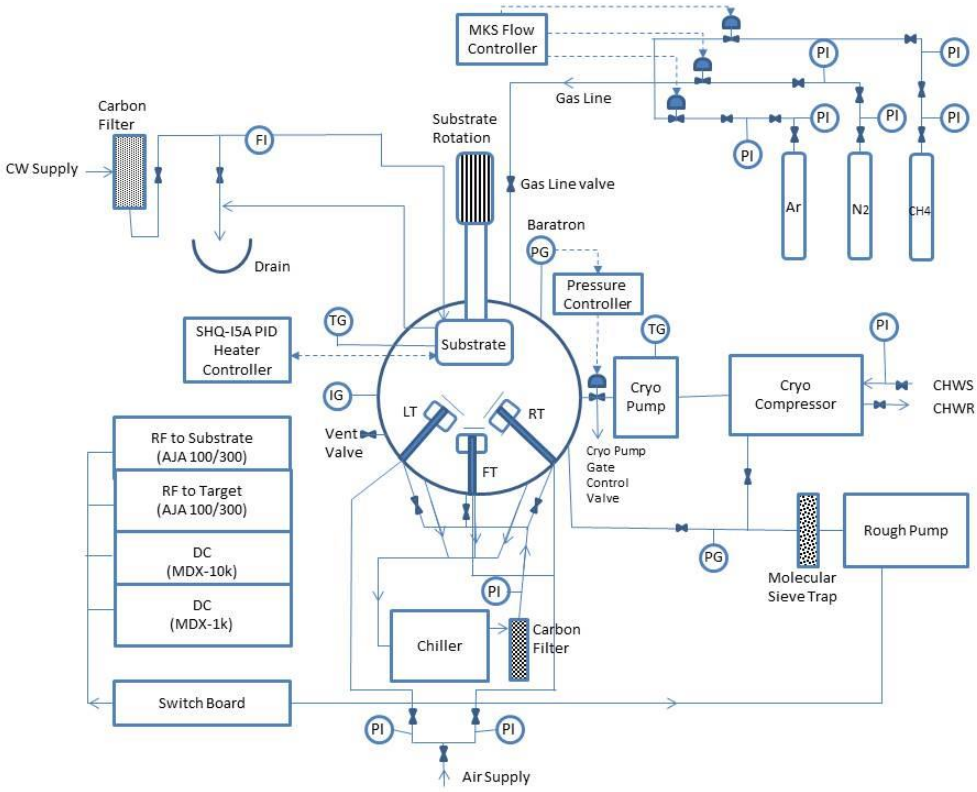

Figure 3-3 Schematic diagram of the PVD reactive magnetron sputtering system

Although the operating procedure can vary based on the specific needs of a particular experiment, the following describes the basic procedure for operation of the SaNEL sputtering system. The sputtering system is pumped down to a pressure of about 20 mTorr using a rough pump with a molecular sieve trap. The pressure in the lines between the rough pump and the cryo pump is measured by a pressure gauge and displayed on the front of the frame supporting the chamber. After pumping down the system with the rough pump, a cryo pump and cryo compressor (cooled by a chilled water supply) are used to achieve a base vacuum level in the range of 10^{-7} Torr. This pressure is measured using an Ion gauge and displayed on a corresponding digital readout. After obtaining an appropriate base pressure, a single gas or a combination of the available gasses including Ar, CH_4, O_2, or N_2 can be flown into the chamber. Their

flow rate is adjustable and can be controlled precisely by mass flow controllers. The cryo pump and a Baratron pressure gauge located within the deposition chamber work together to maintain the working pressure at a user specified value during the coating deposition.

Figure 3-4 Lab-Built PVD reactive magnetron sputtering system in Surface and Nano Engineering Laboratory

This system consists of a deposition chamber containing three magnetron guns with adjustable shutters and a rotating substrate platform. DC or RF power can be applied from any of the available power supplies to any of the three guns or substrate interchangeably, based on the specific coating properties desired. This allows for great versatility in magnetron sputtering deposition since a wide variety of materials including both conducting and insulating materials can be sputtered. In addition, the presence of

multiple, adjustable height and angle magnetron guns within the chamber as well as multiple power supplies allows the user to sputter from multiple targets simultaneously, allowing for excellent flexibility in coating content and morphology. If desired, the temperature of the substrate during the coating deposition process can be precisely controlled with a substrate heating element. Cooling of the magnetrons in order to prevent damage to the magnets is accomplished with the incorporation of a closed loop water chilling system, and the substrate rotation electronic device is kept cool using an open-loop filtered tap water supply.

Figure 3-5 Lab-Built PVD Reactive Magnetron Sputtering System in Surface and Nano Engineering Laboratory

See Figure 3-5 for a photograph of the inside of the sputtering chamber and Figure 3-6 for a photograph of the two racks containing the power supplies, digital controls, and digital readouts for this sputtering chamber.

Figure 3-6 Power Supply and Control Panel for PVD Reactive Magnetron Sputtering System in SaNEL

3.1.2.2 DC and RF Reactive Magnetron Sputtering Experimental Conditions

Experimental sputtering conditions were specifically selected based on a thorough review of the literature and several preliminary experiments designed to gain an understanding of sputtering rate vs. pressure and/or power to the magnetron guns. Because MeSiN composite thin films' properties degrade significantly with the presence of only trace amounts of oxygen impurities, achieving a low base pressure is of high importance. The base pressure should be in the range of 10^{-7} Torr. TiSiN and TaSiN coatings are typically prepared with a Si target, reactive nitrogen gas sputtering, and either a Ti or a Ta target, respectively. In the case of TiSiN coatings, the pressure of the N_2 must be high enough within the chamber to obtain the proper stoichiometry required within the film, but not so high as to poison the targets used in the deposition. [22, 72] Typically when depositing TiSiN coatings, the N_2 makes up approximately 13-20% of the total gas flow, with the remainder of the gas flow being Argon. The target to substrate distance is typically between 6-10 cm, and a negative bias is typically applied at the substrate in order to limit the incorporation of oxygen atoms within the coatings. [48, 62, 74] Also, an applied bias has been shown to produce an energetic plasma that can refine the film microstructure, increasing nucleation and re-nucleation rate and breaking up the columnar structure due to re-sputtering effects. In addition, it has been shown that the substrate temperature during deposition is very important in order to obtain the previously discussed nanocrystalline structure. Some nc-TiN/a-Si_3N_4 coatings have been created by PVD using deposition temperatures of 200°C and 150 mm between the target and the substrate. [62] Other sources claim that the minimum temperature required for deposition of composites using PVD which have full segregation between their TiN and Si_3N_4 phases, stoichiometric formation of TiN, and hardness enhancement is 500-700°C,

and that a distance of less than 10 cm between the substrate and the target is required to have sufficient plasma density at the substrate. [3, 75]

After an extensive review of the literature, conditions were determined experimentally in our lab in order to develop films with high hardness. For all experiments to be discussed, a low base pressure in the range of 10^{-7} Torr was achieved before film deposition, and a low working pressure of 5 mTorr was used in an attempt to limit the impurities present in the coatings. Each of the targets, as well as the substrate was cleaned for 1 minute with Argon plasma before beginning the film deposition. The gas mixture flown into the chamber was 80% Ar and 20% N_2, with both gases being ultra-high purity (99.999%) grade. Si wafer substrates were loaded onto a heated, rotating substrate holder. Rotation was applied to ensure uniform deposition from the two magnetron guns involved in the depositions. The substrate heater was carefully calibrated in house using an external thermocouple so that the precise temperature of the substrate for any given set point on the manufacturer's thermocouple was known, see Figure 3-6. As per this calibration, the set point programmed to the substrate holder device was 650˚C in order for the substrate to reach an actual temperature of 550˚C. Bias ranging from -100 V to -500 V was applied at the substrate to determine the effect of bias voltage on the film morphology and microstructure. The magnetron guns were positioned so that the targets were approximately 10.5 cm from the surface of the substrate. A Ti or Ta target was loaded into the front magnetron, and 150 W DC power was applied in the case of the Ti target. 150 W, 100W, 70W, and 50W were applied to the Ta target, in various experiments. A Si target was loaded into the left magnetron, and RF Power varying between 30-60 W was applied. All films were deposited to approximately 600 nm - 1 µm in thickness. Depositon time was varied between 1.5 and 4

hours, with increasing time for increasing substrate bias, in order to achieve the film thickness.

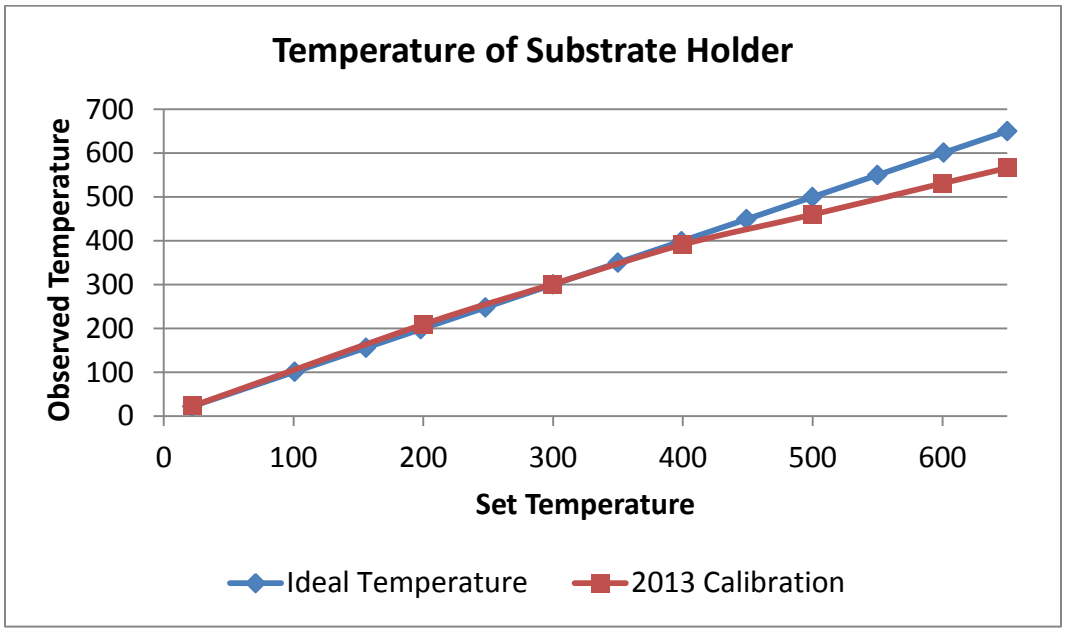

Figure 3-6 Calibration curve for substrate holder ideal vs. observed temperature

3.2 Characterization of MeSiN Thin Films

Complementary characterization techniques were used to study in detail the microstructures of the produced films. XRD analysis provides crystal structure and phases present. TEM and HRTEM provide detailed information regarding substructure and phases present at higher resolution. XPS yields information regarding the atomic composition and chemical states present within the films. Additional, supplementary information was obtained from scanning electron microscopy (SEM), electron dispersive spectroscopy (EDS) and surface optical profilometry. A detailed microstructure understanding is expected to emerge from these studies.

Nanoindentation provides knowledge of the mechanical properties of the coatings including hardness and reduced modulus values. Tribological wear testing provides information such as impact resistance and frictional wear.

3.2.1 XRD

X-Ray Diffraction was carried out on a Bruker D-8 Advance X-Ray Diffractometer with a Cu Kα radiation source and a wavelength of 1.54 Å. The acceleration voltage and filament current were set at 40 kV and 40 mA, respectively. A small step size of 0.03° and a high dwell time of 2 seconds were used in order to obtain high resolution scans. The scans were run several times using the auto-repeat option to minimize the noise present in the final data. Various scan types including θ-2θ scans and low angle detector scans were performed to identify crystalline phases present in the MeSiN films. In addition, the Scherer formula, Equation 1 below, was used to estimate grain size within the films. In this formula, τ represents the grain size, K is a dimensionless shape factor, λ is the wavelength of the X-Ray, β is the full width at half maximum (FWHM) of the peak, obtained from the XRD Commander software, and θ is the Bragg angle of the diffraction peak.

Equation 1: Scherrer formula for estimation of grain size

$$\tau = \frac{K\lambda}{\beta cos\theta}$$

3.2.2 XPS

A Perkin-Elmer Phi 560 XPS/Auger system with an Al Kα source with a characteristic voltage of 1253.6 eV was used to characterize the surface of the deposited films. The surface was sputtered with Ar^+ for a short amount of time (sputter time was dependent on total film thickness) in order to remove surface contaminants of C and O. Survey scans were conducted to determine chemical composition in terms of atom % in

the range of 0-600 eV with 0.2 eV steps. High resolution scans for the Ti, Ta, Si, and N peaks were performed in some cases to provide insight into the chemical state of the elements within the film. The XPS spectra for the films were calibrated using the C 1S peak at a binding energy of 284.5 eV.

3.2.3 Nanoindentation

A Hysitron Ubi 1 Nanoindenter was used to determine the hardness of the deposited films. Hardness tests were carried out with a cube corner tip. For films having high surface roughness, the films were imaged with the nanoindentation tip, and the flattest areas were carefully selected for indentation to avoid effects from the surface roughness on the measurements. Depth controlled indentations were performed at less than 10% of the total depth of the film in order to avoid hardness effects from the underlying substrate. All films presented in this work were mounted onto magnetic disks using crystal bond, since mounting with Carbon tape was found to negatively impact the hardness valued obtained. The elastic modulus and hardness were recorded for 9 indentations within a 20 x 20 μm region, and the average and standard deviation of the data set were calculated.

3.2.4 Tribological Testing

A pin-on-disk apparatus was used to further understand the mechanical properites of the as deposited MeSiN coatings. A 6 mm alumina ball was used with 1 N of force. The sliding distance was 200 m. Coefficient of friction, penetration depth, and overall wear rate were determined from this study. Wear rates were determined by taking four 2-D profiles of the wear track using the optical profilometer. The area under each of these four profiles was calculated, and the average value of the four sample areas was taken. Then, the area was multiplied by the circumference of the wear track to

find the wear volume, and divided by the sliding distance and load to obtain a wear rate in mm^3/Nm.

3.2.5 Optical Profilometry

A Veeco NT-9100 Optical Surface Profilometer was used to gain supplementary data for this research work. The equipment was used with a 5X and 20X objective to gain an assessment of film thickness by calculating the step height between the film and the non-deposited substrate. In addition, the R_a value for surface roughness was obtained for each MeSiN film deposited, and the profiles of the wear tracks created during the tribological study were examined in detail. R_a is a calculation of surface roughness which uses the arithmetic average of the absolute values of the height of the sample to estimate the roughness of a surface via Equation 2, below:

Equation 2: Calculation of surface roughness, R_a

$$R_a = \frac{1}{n}\sum_{i=1}^{n}|y_i|$$

In each case, 2-dimensional and 3-dimensional surface profiles were obtained. In addition, the optical profilometer was used to determine the stress present in the as-deposited coatings. With the presence of residual stress within the TiSiN films, some curvature will be induced onto the Si wafer. The difference in the curvature of the wafer before and after MeSiN coating deposition was measured using the profilometer, then used to calculate the stresses present within each film using Stoney's Equation, Equation 3 below, where E_s, d_s, and v_s are the Young's modulus, thickness, and Poisson's Ratio of the Si (100) substrate, respectively, d_f is the thickness of the film, and R is the delta radius of curvature between the Si wafer before and after film deposition.

Equation 3: Stoney's equation, for estimation of residual stress based on Si substrate radius of curvature

$$\sigma_f = \frac{E_s d_s^2}{6(1-v_s)} * \frac{1}{d_f} * \frac{1}{R}$$

3.2.6 SEM and EDS

A Hitachi S-3000N Variable pressure SEM with an attached EDS was used to obtain further supplementary data for MeSiN films. A high vacuum setting, a working distance of 15 mm, and an electron voltage of 10-15 keV were used to obtain images of the surface morphology of the coatings as well as comparatively assess the chemical content (at %) of the films.

3.2.7 HRTEM

A Hitachi H-9500 High Resolution TEM with an attached EDS was used to gain a detailed understanding of the microstructure and crystalline phases present in the MeSiN films studied. Cross Sectional and Plan View TEM samples were prepared of various coatings. Low magnification images were captured to assess the overall morphology through the thickness of the film, and high resolution images were used to understand the nanoscale structure of the films and analyze the lattice fringes to determine the orientation of the crystal structures present. Electron diffraction patterns (EDP) were used to identify the crystal structure of both individual grains and of the overall nanocrystalline samples.

Chapter 4

Microstructure and Property Investigation of Arc Deposited Titanium Silicon Nitride Coatings

4.1 Introduction

TiN is an important material in the field of tribological coatings. Work in recent years has shown that incorporation of Si into TiN results in unique materials with enhanced mechanical and thermal properties. The most commonly proposed morphology for this material consists of nanocrystalline TiN grains surrounded by a Si_3N_4 matrix. [13, 20, 22, 47, 58-60, 63, 76-79] In addition, other researchers have reported the presence of other nanocrystalline titanium silicide phases of varying stoichiometry, [12, 80-82], and others have reported the presence of (TiSi)N crystalline phases in which Si atoms occupy Ti positions within the FCC lattice. [83-85]

It has been proposed that only TiSiN coatings deposited at temperatures at or above 550˚C could achieve high hardness due to nanocomposite morphology, since samples deposited at these elevated temperatures are thought to undergo spinodal decomposition to yield the two distinct nc-TiN and a-Si_3N_4 phases. [3, 6, 56] However, studies by our collaborators report coatings with high reported hardness of 50 GPa deposited via the previously discussed LAFAD Arc technique at a temperature of only 350˚C.

4.2 Hardness of Arc TiSiN Coatings

In a collaborative effort with Cheng et al, TiSiN films were studied in order to gain an understanding between the high previously reported hardness of 50 GPa and the nanoscale crystalline morphology of the coatings. Nanoindentation was performed to confirm the previously reported hardness of 50 GPa for the high Si and 37 GPa for the

low Si coatings, and surface optical profilometry was used to gain an understanding of the surface roughness of the as deposited TiSiN films.

4.2.1 Optical Surface Profilometry of Arc TiSiN films

Both the low Si and the high Si coatings were examined using optical profilometry in order to obtain the surface roughness for each coating. Overall, it was found that the surface roughness was high, with values of R_a = 25.2 nm and R_a = 26.5 nm for the low and high Si films, respectively.

A surface profile of the low and high Si samples displaying the surface roughness can be seen in Figure 4-1 on page 38. The relatively large “hill” type features present on the surface of both the low Si and the high Si films are likely a direct effect of the Arc sputtering method, which has the tendency to sputter nanoscale portions of the target material, as opposed to a more refined atom-by-atom deposition. These hills, which varied from about 0.1 µm to 1 µm in height, had to be carefully avoided when the hardness was measured via nanoindentation. Since the thickness of the coatings was about 2 µm, nanoindentation could be carried out to a maximum depth of 200 nm, which was on the order of the hills present on the sample surface. Indention locations carefully selected on the flat areas of the film were found to give highly repeatable hardness measurements, but indentation locations selected randomly without thought to the surface topography yielded highly irregular hardness results.

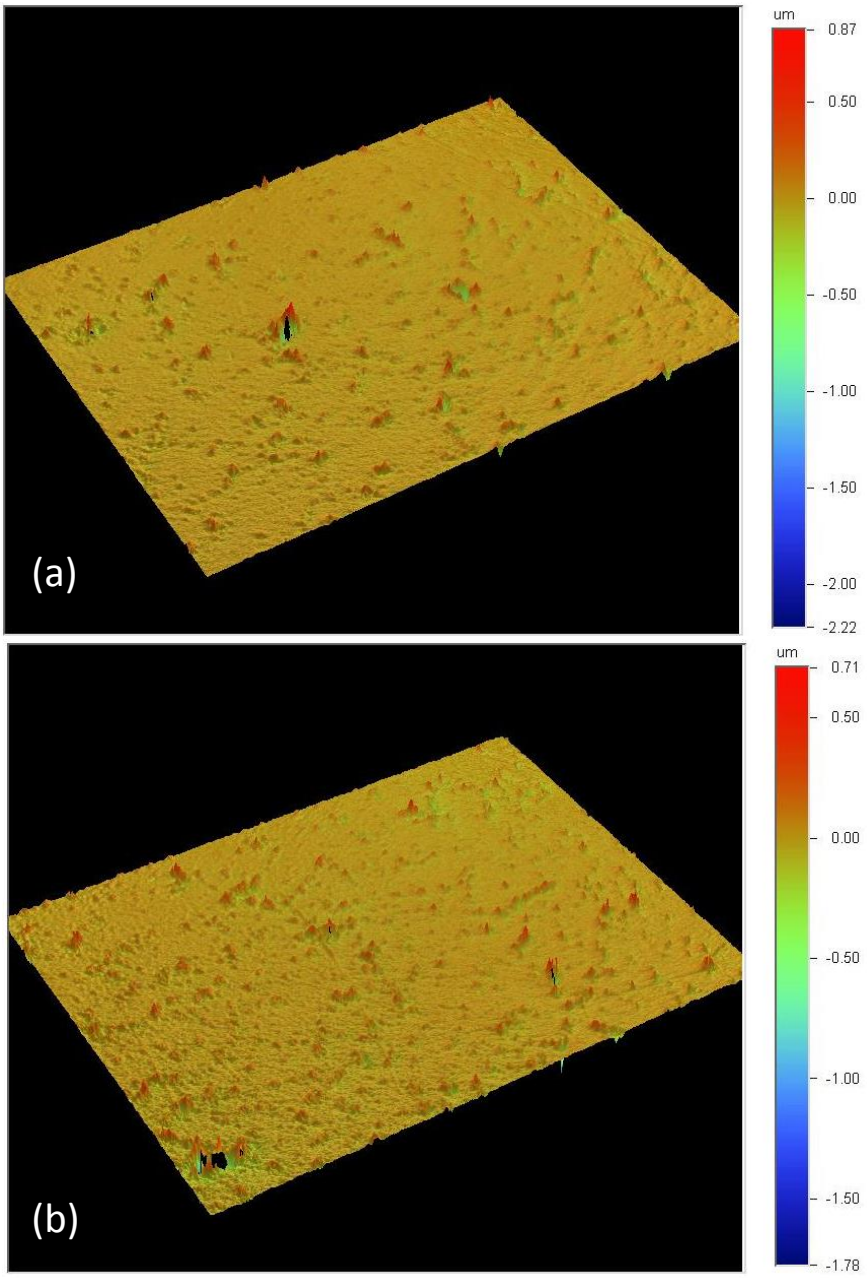

Figure 4-1 Optical profilometer profiles illustrating rough features present on the surface of the Arc TiSiN (a) Low Si and (b) High Si films

4.2.2 Nanoindentation of Arc TiSiN Films

Nanoindentation was used to test the hardness of the TiSiN coatings. While the previously reported hardness for the low and high Si were 36 and 51 GPa, respectively, the more recently obtained values using the Nanoindenter were more modest at 29.8 and 33.4 GPa. The large difference in the two data sets could potentially be explained by the high surface roughness of the sample. The flattest areas of the sample had to be carefully selected for nanoindentation, since indenting on a peak or valley was found to drastically alter the results, yielding both high and low outliers and unreliable data points for hardness measurements. A comparison of the previously published hardness results to the more recently obtained results using the CCMB UBI-1 Nanoindenter can be seen in Figure 4-2.

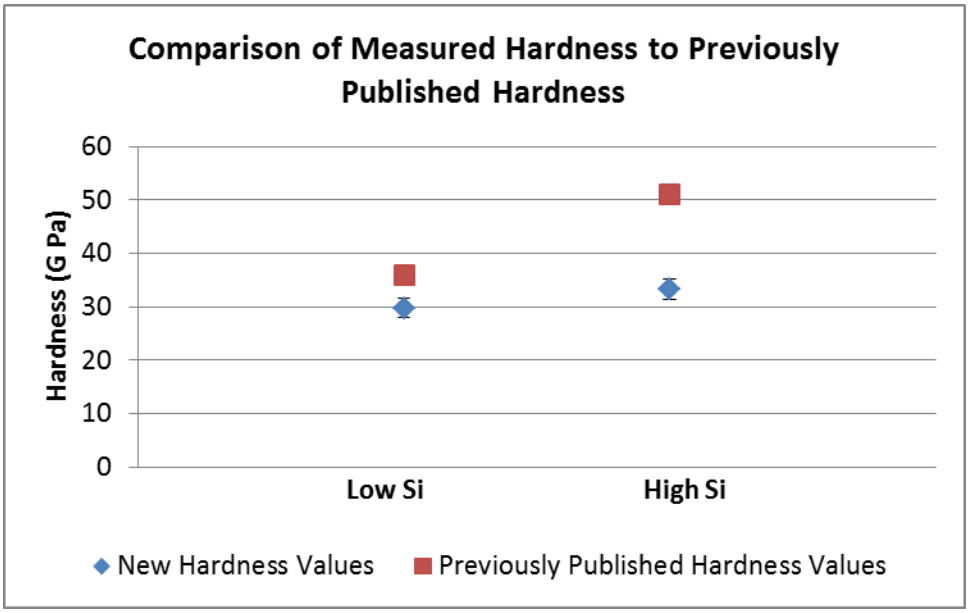

Figure 4-2 Comparison of previously reported hardness results (red) and hardness data obtained on the CCMB's Hysitron UBI-1 Nano-Indenter (blue) for both low and high Si films

4.2 Microstructural Study of Arc TiSiN Coatings

A detailed study of the microstructure of the Arc TiSiN coatings was completed to gain an understanding of the relationships between deposition conditions, coating morphology at the nanoscale, and coating properties. The films were deposited to a thickness of 2 µm onto stainless steel substrates. Si content was varied by changing the Si content present within the sputtering targets at values ranging from 0% to 20%. XRD, electron diffraction, and nanobeam diffraction were used to identify the presence of crystalline TiN and TiSiN phases. HRTEM was used to study the morphology of these identified phases, and EDS was used as a complimentary tool to understand the chemical content of the films at various locations.

4.2.1 X-Ray Diffraction of Arc TiSiN Coatings

XRD patterns can be seen in Figure 4-3 on page 41, and they are in agreement with previously published results. [60] The low angle scans displayed used an incidence angle of 5˚, because this angle of incidence allowed for penetration of the X-rays throughout the film, with only very limited penetration into the substrate, see Table 4-1 on page 40.

Table 4-1 Estimated depth of X-Ray penetration into TiSiN coatings and substrate at varying angles of incidence

Incidence Angle (degrees)	D_p (µm)
3	1.5
5	2.5
8	3.99
10	4.98
15	7.42

The low Si film appears to have a preferred orientation of TiN (111), as evidenced by the dominant peak located at 2θ = 36.5˚. A TiN (220) peak is also visible at 61.5˚. A Ti (100) shoulder can be seen at 35.4˚. The small peak visible at 39.8˚ originates from the Al sample holder used in the XRD setup. In the high Si film however, TiN (111) is no longer the dominant peak. Instead, the highest intensity TiN peak is TiN (220). This data supports the previously published observation that increasing Si content leads to a change in the preferred orientation of TiN grains within the coatings. [46, 60, 63, 64]

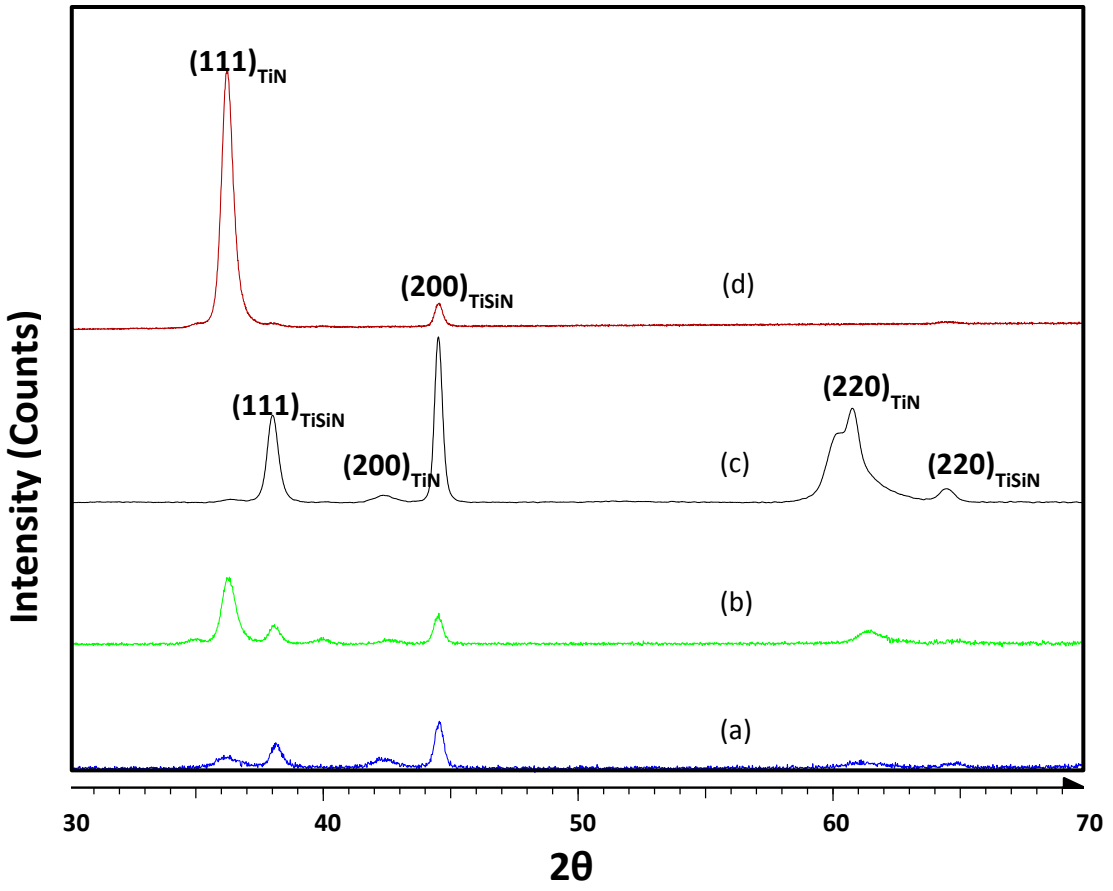

Figure 4-3 XRD scans including a) High Si with low angle scan, b) Low Si with low angle scan, c) High Si with theta-2theta scan, d) Low Si with theta-2theta scan

While it was previously reported that the peak at 38.0˚ corresponded to TiSi (102), and the peaks at 44.8˚ and 64.9˚ corresponded to the BCC stainless steel 17-4 substrate, the present work instead identifies these peaks as a separate TiSiN phase in which the Si atoms replace selected Ti atoms within the TiN FCC lattice. This Si incorporation causes a decrease in the lattice constant from 0.426 nm to 0.410 nm, which can be observed in the shift in the diffraction peaks of the XRD data. The presence of this additional phase was not immediately obvious. These peaks were unfortunately previously recorded as substrate peaks, since their location is nearly identical to the stainless steel 17-4 XRD peaks. [46, 60] Upon close inspection of the low angle XRD spectra, it was hypothesized that there may be an additional phase present at these locations, besides just the substrate. Figure 4-4 shows a zoomed in view of the peak previously reported as an Fe (110) substrate peak at 44.4˚ for the high Si film at varying angles of incidence.

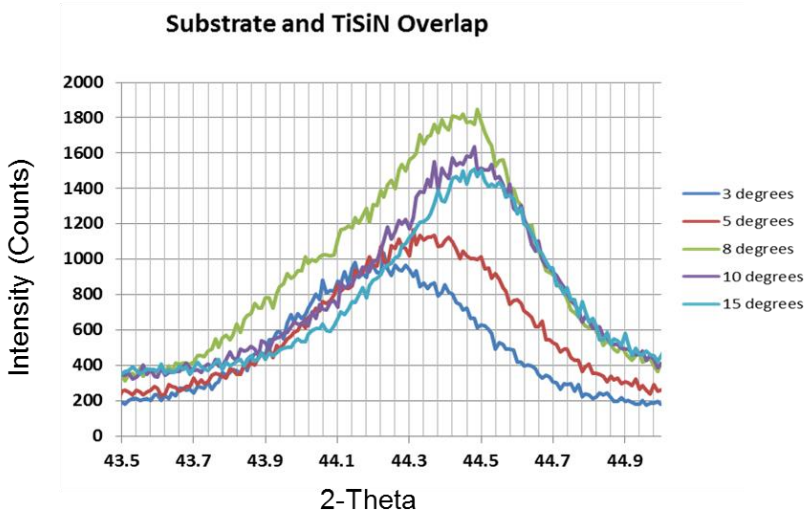

Figure 4-4 Low Angle XRD of High Si substrate and TiSiN (200) peak

Close inspection of this peak shows that the peaks in the 3˚ and 5˚ scans are centered around 44.3˚, while the peaks for the 8˚, 10˚, and 15˚ scans are shifted slightly to the right, with their centers at approximately 44.5˚. According to the estimates in Table 4-1 on page 40, the two lowest angle scans should penetrate only very little into the substrate, so the analysis should show mostly data from the coating itself, and little to no substrate peak should be visible. The presence of X-Ray diffraction signal at these low incident angles served as an early indicator that an additional phase besides the stainless steel 17-4 substrate may be present. This work identifies the presence of an additional phase, previously unreported due to overlap with the substrate peak. Further analysis via HRTEM, electron beam diffraction, and EDS to be discussed later confirms the identity of this phase as FCC TiSiN.

In addition, the Scherer formula was used to estimate grain size for the TiN and the TiSiN phases in the low and the high Si films. Using the 3˚ and 5˚ incident angle scans, the grain size for all phases was estimated at 12.5-15.5 nm and 7-11.5 nm for the low and high Si films, respectively. This was done using the Full Width at Half-Max (FWHM) feature on the EVA software and the Scherer formula. It should be noted that an additional phase is present that was not identified by XRD. EDS, HRTEM analysis, and electron nanobeam diffraction identified a very small number of crystalline TiSi grains, but the quantity of these grains are likely too low to be detected by XRD.

4.2.2 TEM Analysis of Arc TiSiN Coatings

TEM was used to examine the morphology in great detail, and electron beam diffraction helped to confirm the presence of the TiSiN crystalline phase first identified via XRD. Cross sectional and plan-view samples were prepared and examined, and additional FIB cross section samples were studied for both high and low Si contents. The attached EDS was used to gain an understanding of chemical content both at the micro

scale through the thickness of the coating and at the nano scale with the examination of individual grains.

4.2.2.1 Columnar Morphology of TiSiN Coatings as identified by TEM

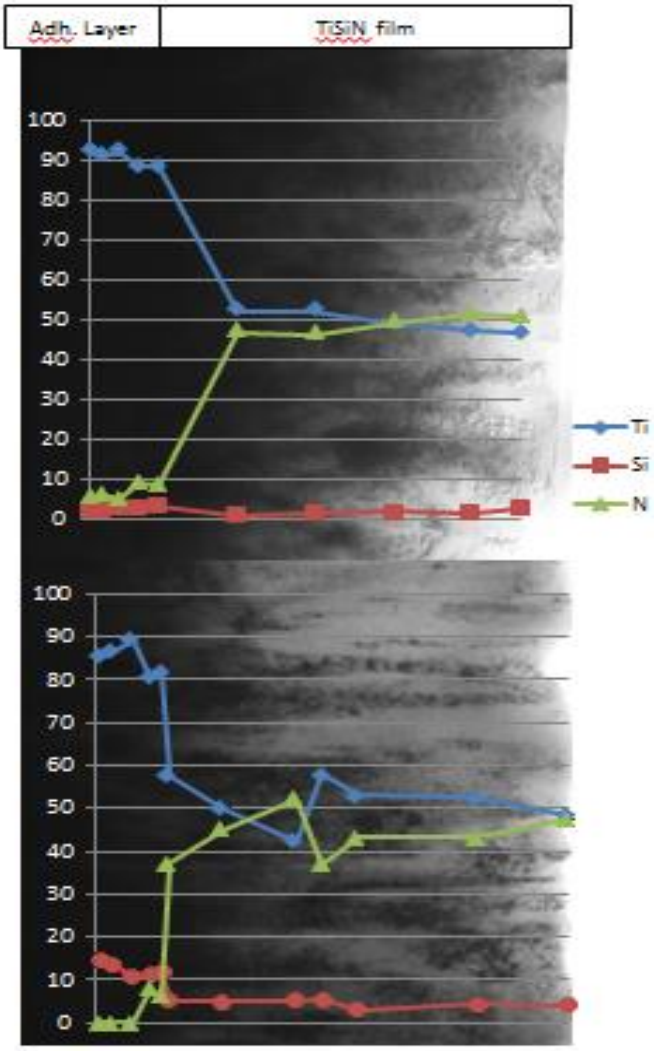

Figure 4-5 Cross Section TEM images of (top) Low Si film and (bottom) High Si film showing stainless steel substrate, TiSi adhesion layer, and TiSiN film and EDS analysis through the thickness of the film

HRTEM was used to analyze the films at the nanoscale and gain further understanding of the nanocrystalline morphology and structure of both the low and the high Si coatings. Low magnification cross-sectional images show that films of both Si content appear to be columnar in structure, as seen in Figure 4-5 on page 44. Figure 4-5(a) shows the columns in the low Si film, and Figure 4-5(b) shows the columnar structure of the high Si film. In both films, the columns span the entire thickness of the film, beginning at or within the adhesion layer, and continuing up to the film surface. The columns in the low Si film vary between 100-200 nm in width, while the columns within the high Si sample are thinner, ranging from 40-100 nm in diameter, suggesting that the increased presence of Si within the coatings serves to refine and reduce column thickness within the films.

Plan-view HRTEM analysis confirmed the size of the columns in both the high Si and the low Si cases. Figure 4-6 on page 46 shows the plan-view TEM view of the columns, as seen from the surface of the coating. It can clearly be seen that the columns are of larger diameter in the low Si film, Figure 4-6(a). In the high Si film, Figure 4-6(b), the Si content serves to reduce and refine the columnar diameter.

EDS analysis through the thickness of the films can be seen overlaid onto the TEM images in Figure 4-5(a) and 4-5(b) for the low and high Si films, respectively. This data was obtained by from the cross sectional TEM samples by performing EDS at various points throughout the TiSi adhesion layer and the film. The adhesion layer was deposited using a TiSi target with 5% Si for the low Si film and TiSi target with 20% Si for the high Si film. The adhesion layer for the low Si film contains >90 at% Ti and about 5 at% Si, and the adhesion layer for the high Si film contains about 85-90 at% Ti, with the remaining 10-15 at% comprised of Si. After deposition of the adhesion layer, N_2 gas was introduced into the sputtering chamber, and Si content drops to less than 2 at % in the

low Si sample and to 4-6 at % in the high Si sample. Both data sets show that the Ti:N ratio is slightly off from stoichiometric 1:1. The EDS results agree in general with the previously published XPS results by Cheng et al, presented in Figure 3-2 on page 23. [60]

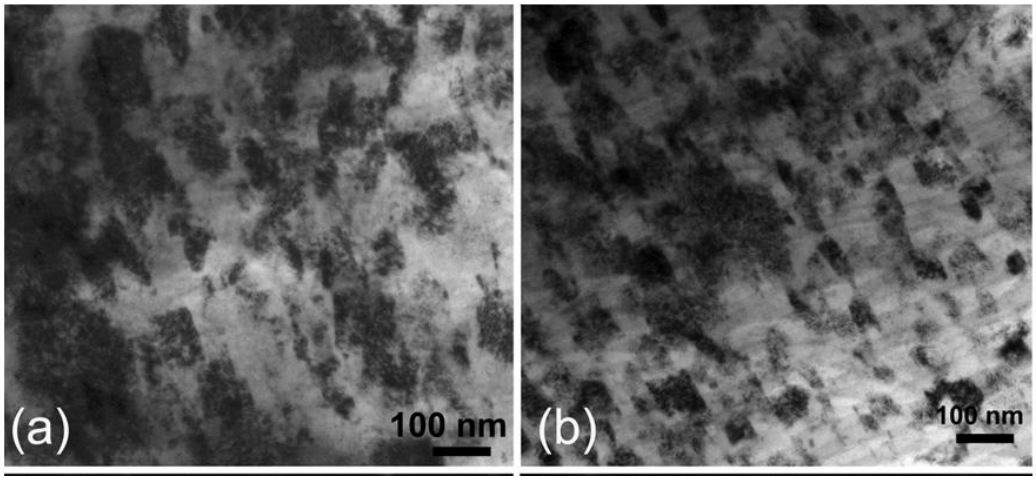

Figure 4-6 Plan-View TEM showing the diameter of the columns in (a) Low Si TiSiN and (b) High Si TiSiN

TEM electron beam diffraction was performed on the cross section TEM foil on areas shown on the left hand side of figures 4-7(b) and 4-7(d) below which included neither the stainless steel substrate nor the adhesion layer. The TEM ring diffraction patterns present in Figure 2-2 on page 48 indicate the presence of TiN and TiSiN in both samples. The ring patterns exhibit typical characteristics of an FCC structure, but two closely spaced rings are present within each bundle. In each bundle, two rings exist. The inner ring of each bundle has a lattice parameter of a = 4.26 Å, and the outer ring has a lattice parameter of a = 4.07 Å. The inner ring consists of FCC TiN, and possibly a small amount of $Ti(N_{(x)}, Si_{(1-x)})$, where Si takes the place of N within the crystal lattice. The outer ring represents FCC $(Ti_x, Si_{(1-x)})N$, where Si takes the place of some Ti atoms

within the crystalline lattice, reducing the lattice parameter by approximately 3%. The first three of these bundles can be easily indexed as (111), (200), and (220). Table 4-2 on page 47 lists the phase and the measured d spacing corresponding to each labeled ring.

Table 4-2 Phases identified by electron beam diffraction in high and low Si films

Ring	d measured	Phase
Low Si FIB Sample Ring Diffraction		
1	2.46	TiN (111)
2	2.37	TiSiN (111)
3	2.19	TiN (200)
4	2.04	TiSiN (200)
5	1.68	TiSi (021)
6	1.44	TiN (220)
7	1.23	TiN (222)
High Si FIB Sample Ring Diffraction		
1	2.33	TiSiN (111)
2	2.08	TiN (200)
3	1.43	TiN (220)
4	1.23	TiN (222)
5	1.17	TiSiN (222)
6	1.03	TiN (400)

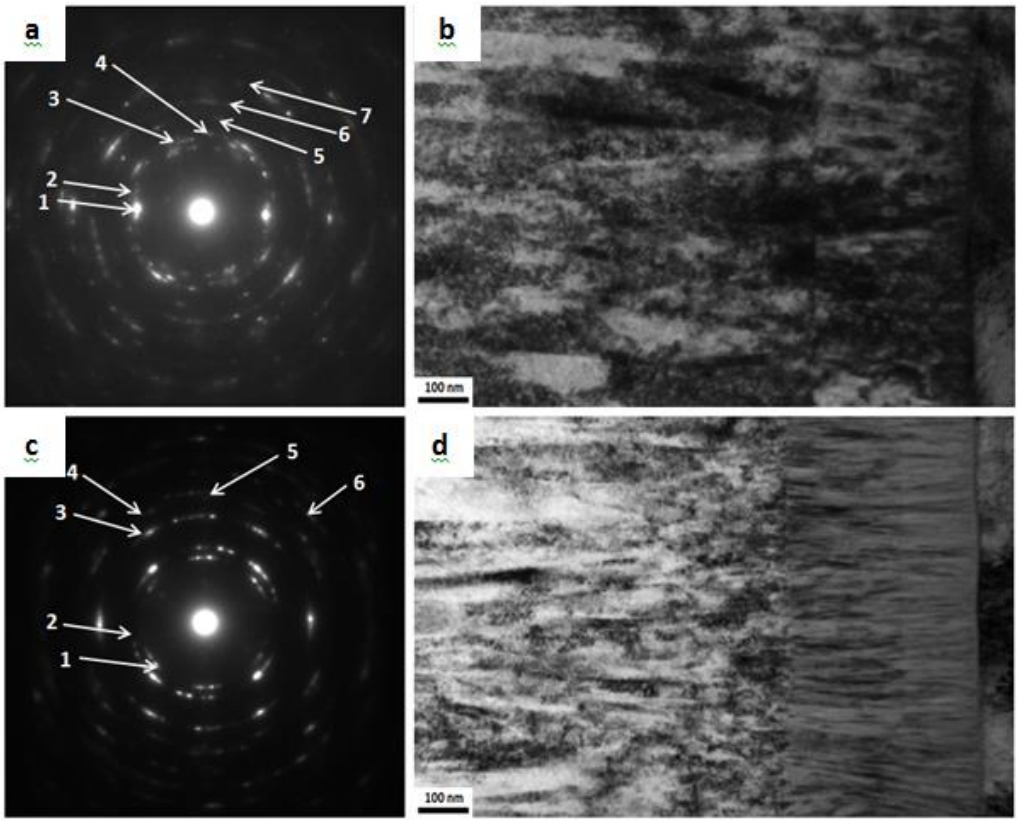

Figure 4-7 Low magnification TEM Images of the TiSiN film (left), the TiSi adhesion layer (middle) and the SS substrate (right) of (b) Low Si and (d) High Si and electron beam diffraction of (a) Low Si and (c) High Si TiSiN Arc coatings

4.2.2.2 Characterization of Nano-Scale Subgrain Morphology via HRTEM

While analysis of the TiSiN films at low magnification reveals a clear columnar structure, high resolution images indicate the presence of subgrains within each column. As observed by HRTEM, the size of these subgrains is about 7-10 nm in the low Si film and about 5 nm in the high Si film. This again indicates the tendency of increased Si content within the coatings to reduce and refine the microstructure, decreasing the size of the subgrains. This finding generally agrees with the previously discussed estimations of grain size based on analysis of the low angle X-Ray diffraction peaks via the Scherer

formula. In addition, the presence of additional Si serves to morphologically define the individual subgrains within columns; the subgrain boundaries within the high Si sample are clearly visible in Figure 4-8(b), while the subgrains in Figure 4-8(a) are still apparent, but are less clearly defined.

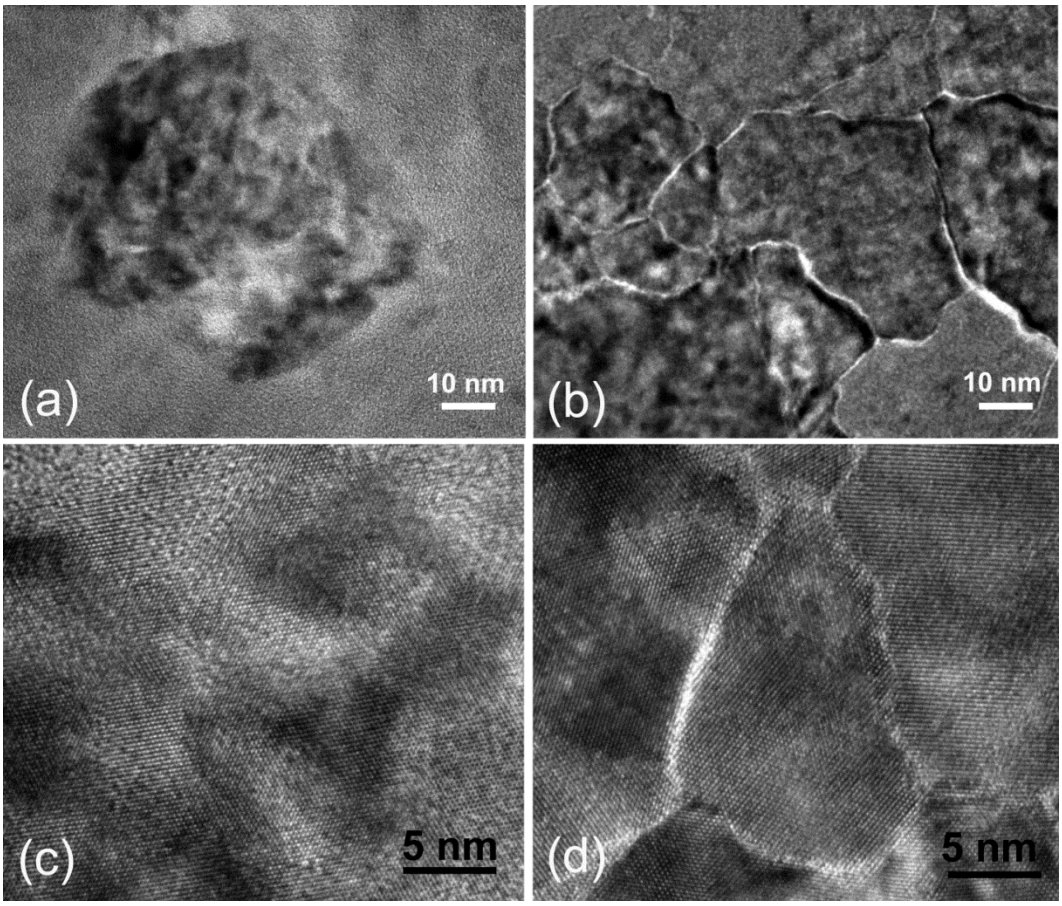

Figure 4-8 Plan-View HRTEM showing the grain boundaries of (a) low Si, (b) high Si and atomic structure and lattice fringing of (c) low Si and (d) high Si

HRTEM images showing the atomic structure of the subgrains in the low Si and the high Si films can be seen in Figure 4-8 (c) and 4-8 (d). From these images, it is apparent that while Si content has only a marginal effect on the size of the subgrains within the columns, it plays a clear role in the definition of the subgrains and their grain

boundaries in addition to its previously discussed role in the reduction and the refinement of the columnar diameter and structure. In Figure 4-8 (d), it is easily seen that the lattice fringes throughout the image possess different orientation. In addition, they have different lattice spacing, with grains being present in different orientations. In the low Si sample in Figure 4-8 (c), however, no obvious boundaries can be detected within the subgrains. The lattice fringes and orientation throughout the subgrains present in the image are very similar. Subgrains are distinguished by only slight differences in the lattice fringing, as well as compositional contrast between the lighter and darker grains in the micrograph.

4.2.2.3 EDS Analysis of TiSiN films

Numerous EDS spectra were obtained in the plan view and in the cross sectional TEM samples for both the low and the high Si films. In general, the EDS spectra collected from the low Si film can be generally categorized into three types, seen in Figure 4-9 (a) on page 51. By selecting individual subgrains within columns, the three basic compositions identified were TiN, $Ti_{50}(N_{(50-x)}Si_x)$, and $(Ti_{(50-x)}Si_x)N_{50}$, where x typically varied between 2-4 at%. The compositions present within the High Si sample were generally TiSi, $Ti_{50}(N_{(50-x)}Si_x)$, and $(Ti_{(50-x)}Si_x)N_{50}$, but x increases to values between 6-10 at %, Figure 4-9 (b).

In addition, EDS was used to systematically study the difference in composition between the light grains and the dark grains in the high and the low Si films. While the bright grains and the dark grains have very similar Ti content, it was found that overall, the dark grains tended to have higher Si content and lower N_2 content, Figure 4-9 (c).

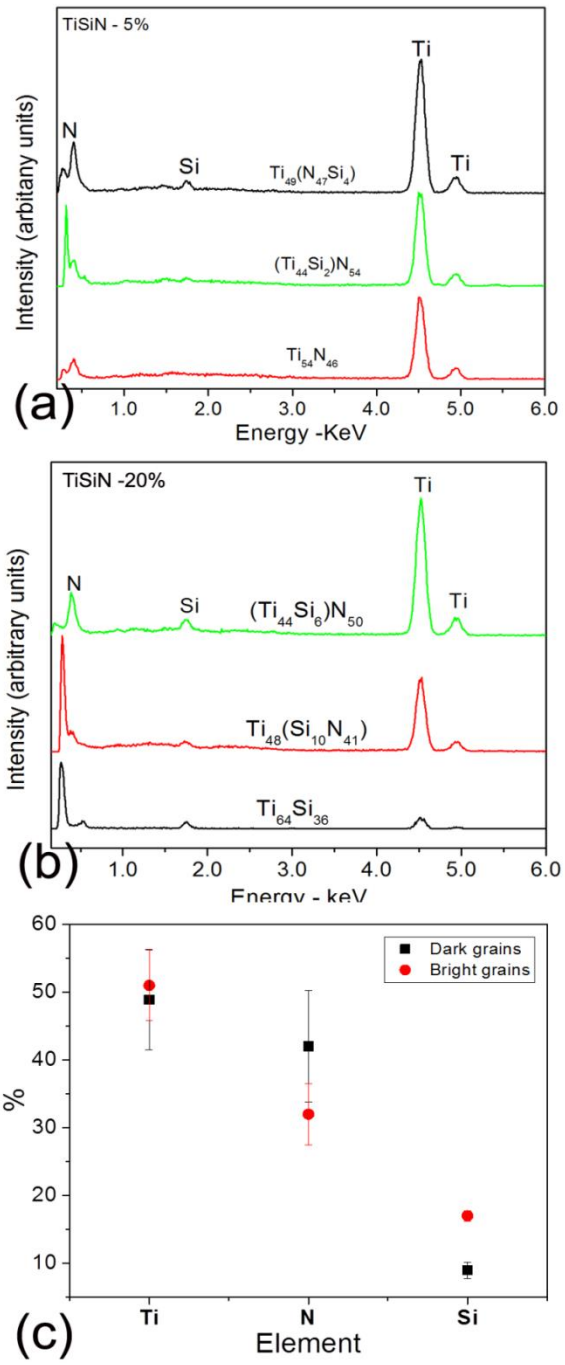

Figure 4-9 EDS spectra of chemical composition of grains in (a) Low Si and (b) High Si films, and (c) average chemical compositions of light and dark grains in High Si film

4.3 Discussion & Conclusions

The Arc deposited TiSiN samples were chosen for a detailed analysis due to their excellent mechanical properties, with reported hardness above 50 GPa. While in-house nanoindentation showed hardness under 35 GPa, far under the previously reported values, these properties are still quite remarkable, especially considering the processing conditions employed for the coating depositions. While it is commonly suggested in the literature that the nc-TiN/a-Si_3N_4 structure proposed by Veprek is only possible due to spinodal decomposition, these coatings show signs of this morphology, even though the substrate was heated to only 350˚C during the coating depositions. This is 200˚C below the reported minimum temperature for the chemical spinodal to occur, which has been theoretically calculated at 550˚C. [1, 3, 4, 6, 23, 56, 79] Although the Arc deposited TiSiN coatings appeared to be columnar upon early low magnification TEM investigation, careful analysis showed the presence of nano-scale crystalline subgrains, surrounded by brighter grain boundaries which likely contain amorphous Silicon phases. This result is somewhat surprising, since other reports of TiSiN deposited via PVD methods in the literature typically report hardness in the range of only 20-30 GPa when temperatures under 500˚ are employed. [3, 13, 25, 46, 48, 60, 63, 77, 78, 86]

One possible explanation for the excellent mechanical properties in spite of the low substrate temperature during deposition could be due to the high energy process by which the coatings were deposited. Arc is widely known as a high energy form of PVD, and it has been shown that it has high rates of energetic ion bombardment at the substrate. [46, 60, 63] This is supported by the high surface roughness in the range of 20-30 nm found on these coatings. Other methods of PVD, such as reactive magnetron sputtering which will be discussed shortly, tend to have lower rates of ion bombardment. This lower rate of ion bombardment in less energetic methods of PVD is supported by

both the lower deposition rate of the films and the much smoother surface of the coatings, with R_a values typically near 10 nm. Thus, it is possible that the high rate of sputtering and ion bombardment causes sufficient energy transfer from the kinetic energetic ions to the surface of the coating as to allow for significant local heating. Increased localized temperature due to such a mechanism could cause sufficient energy for the chemical spinodal to occur consistently at the surface throughout the deposition process. Such a mechanism potentially explains the resulting clearly defined nanoscale subgrains within the overall columnar structure and high film hardness, in spite of substrate heating quite far below the reported requirements for spinodal decomposition to occur.

Detailed analysis of the Arc deposited TiSiN films yielded an enhanced understanding of the relationship between the nanoscale morphology and the desirable mechanical properties. While the composites were previously believed to consist of nanocrystalline TiN and amorphous Si_3N_4, examination via TEM yielded information and understanding on a level which was not possible with previous methods of study such as the previously reported XRD and XPS. In fact, while many current academic publications on MeSiN systems claim to have achieved Veprek's proposed nc-MeN/a-Si_3N_4 nanocomposite morphology, they typically report data including XRD, XPS, and SEM analysis. [44, 46, 50, 59, 60, 63, 87] While these analysis allow for an understanding between processing positions, crystal structure, and chemical content, they lack the depth and detail necessary for better understanding of the effects of the nanoscale morphology of the coatings on the mechanical properties. A detailed understanding of this relationship emerges, however, by employing TEM and HRTEM analysis, as well as low angle XRD. In fact, it is found in this study that the development of the fine microstructure proposed by Veprek consisting of ~10 nm TiN grains embedded in a thin

monolayer Si_3N_4 matrix is apparently quite a challenging task. This structure likely requires ideal processing conditions to allow for the required uniformity at the atomic level. Thus, deposition methods employing highly energetic processes with very high deposition rates such as Arc PVD may not be capable of forming the fine microstructure with Si content localized only within a monolayer boundary. In addition, this challenge could change the overall content of Si required in the coatings from the typically predicted values of 8-12%, since a portion of the Si is shown to reside within the TiN FCC structure, instead of within the amorphous grain boundaries, as previously expected.

Increasing Si presence in the TiSiN films serves to increase the reported hardness of the coatings. The increased Si content has a clear effect on the morphology of the films, impacting both the diameter of the columns which span the thickness of the films and the size and grain boundary definition of the nano-scale subgrains within the films. While the columns in the low Si film were 100-200 nm in diameter, as observed in both cross-section and plan-view TEM samples, the column diameter decreased to 40-100 nm for the high Si sample. The columns are believed to form due to the low deposition temperature of 350˚ C. Within the columns, subgrains ranging in size from 7-10 nm for the low Si film and about 5 nm for the high Si film, were discovered. While the decrease in the size of the subgrains with increasing Si content was not apparent but not extreme, there was a significant difference in the appearance and the structure of the subgrain boundaries, as identified by HRTEM. Thus, a significant advancement of the understanding between morphology and mechanical properties is gained, showing that the presence of Si served to reduce and refine the structure both a the columnar, micro-scale level, and equally importantly, at the nanocrystalline level. The reduction in the width of the columns creates significantly more column boundaries within the coatings, increasing the overall contribution of the grain boundaries within the system to act as

sinks for dislocation and enhance the hardness. In addition, the clear definition of grain boundaries with increased Si could serve a quite similar purpose, further contributing to the impressive mechanical properties of these films.

Theta-2Theta and Low Angle XRD scans confirmed the previously reported shift in preferred orientation from the (111) to the (200) orientation with increasing Si content in the coatings. Using a combination of Low Angle XRD and EBD, the existence of an additional FCC crystalline phase was positively confirmed. This phase was previously identified as the BCC SS 17-4 substrate, but low angle XRD proved that this could not be the case, since diffraction response was measured when the incidence angle of the X-Ray was such that only the film was being probed, and no signal could possibly be coming from depths corresponding to the underlying substrate.

After extensive analysis, as well as complimentary data from EDS, this phase was confirmed to be a TiSiN phase, with Si substituting for select Ti atoms within the TiN FCC crystal lattice, resulting in an approximate 3% decrease in the experimentally observed lattice parameter as compared to FCC TiN. In addition, EDS indicates the presence of a (TiSi)N phase, with Si substituting for Ti within the FCC TiN lattice. The presence of these phases is likely made possible by the high presence of energy at the sight of the substrate, due to the energetic nature of Arc PVD sputtering. In addition to the previously discussed possible rise in thermal energy contributing to spinodal decomposition, this excess energy presence likely allows for the insertion of Si and N atoms into the FCC lattice. These atoms can be forced into the positions typically occupied by Ti atoms. Although no accurate method of residual stress estimation could be employed for these highly textured TiSiN coatings, it seemed that their residual stress was quite high, since the films curved significantly during TEM sample preparation. The presence of residual stress could be due in part to the substitution of Si atoms into the

FCC lattice and the presence of the (TiSi)N phase. This assumption gains validity by the fact that significantly more curvature occurred in the high Si film during TEM foil preparation, as compared to the low Si sample, indicating that additional Si, and thus additional substitution of Si into the crystal structure, could increase the presence of coating residual stresses. The relationship between residual stresses, morphology, and mechanical properties was a common thread throughout the investigation in this body of work on MeSiN coatings, and it will be discussed in more detail in regards to TiSiN and TaSiN coatings deposited using Reactive PVD Magnetron Sputtering shortly.

Chapter 5

Relationship of Microstructure and Mechanical Properties in PVD Magnetron Sputtered Titanium Silicon Nitride Thin Films

5.1 Introduction

TiSiN was studied as a model system in order to gain a fundamental understanding of the relationship between mechanical properties and morphology of MeSiN coatings as deposited using PVD Magnetron sputtering. Since much work currently exists for the TiSiN system, an extensive literature review was performed in order to select initial conditions for experiments to take place at SaNEL. Based on this literature review, preliminary experimental conditions were selected. From these preliminary conditions, parameters were adjusted as needed based on experimental results in order to further increase the hardness of the coatings, with an end result of an as-deposited TiSiN coating with a hardness of 38.9 GPa. This hardness is comparable to the 35-40 GPa values of hardness obtained in the literature for other researchers using PVD magnetron sputtering systems with similar vacuum pressure capabilities.

Based on an extensive literature review, it was clear that oxygen impurities have detrimental effects of the mechanical properties of TiSiN systems. Therefore, a negative bias was always applied at the substrate to repeal O^{2-} ions, and the working pressure was kept very low at 5 mTorr to discourage the presence of impurities within the sputtering chamber. [48, 88-91] In most cases, the ratio of Ar:N_2 gas was kept at 4:1, with the flow of Ar being 20 sccm, and the flow of N_2 being 5 sccm. In several of the later experiments, the Nitrogen flow was increased to 25% of the total gas flow. The substrate was held at a temperature of 550˚C, which has been shown to be required to achieve the proposed spinodal decomposition which is necessary for the formation of the nc-TiN/a-Si_3N_4 nanocomposite structure. The magnetron guns holding the Ti and Si targets were

positioned such that the target and substrate were approximately 10.5 cm apart. Although several several target to substrate distances were explored, only coatings deposited at the 10.5 cm distance will be discussed in this document, since this intermediate distance allowed for both sufficiently high deposition rate and acceptable coating uniformity. In this study, the bias at the substrate was varied in order to determine the effect of increased energy presence at the substrate during film deposition, since it has been previously shown that substrate bias can have the effect of fine nanostructure refinement through the continued re-sputtering of the coating surface. This relationship had not been previously explored in detail for the TiSiN system for magnetron sputtered samples deposited at low working pressure. Once the effect of bias on mechanical properties of the coatings was established, the coatings were fine-tuned by adjusting additional deposition parameters such as Si content, Ar/N_2 flow ratio, and substrate rotation to obtain high hardness TiSiN films. Table 5-1 on page 59 shows the coatings and processing conditions which will be discussed in detail through the remainder of this chapter. Conditions not listed in the table include working pressure, substrate temperature, and distance between the target and substrate which were held constant at 5 mTorr, 550˚C, and 10.5 cm, respectively, for all depositions to be discussed in this document.

Table 5-1 Record of TiSiN deposition conditions and basic results

	Substrate			Ti Target			Si Target			Volumetric Flow		Deposition Rate (nm/h)	Hardness (GPa)	E (GPa)
Coating Name	Power (W)	Voltage (V)	Current (mA)	Power (W)	Voltage (V)	Current (mA)	Power (W)	Voltage (V)	Current (mA)	Ar (sccm)	N_2 (sccm)			
B100 Si60	3.8	100	38	150	307	537	60	263	228	20	5	390	37.1	281.2
B200 Si65	8	200	40	150	328	501	65	266 V	244	20	5	380	32.2	263.7
B300 Si65	12.6	300	42	150	327	503	65	267 V	243	20	5	335	31.5	262.8
B400 Si65	16.8	400	42	150	324	508	65	266 V	244	20	5	300	22.4	189.8
B500 Si65	19.5	500	39	150	333	492	65	264 V	246	20	5	230	18.5	191.4
B100 Si50	3.9	100	39	150	318	519	50	255 V	196	20	5	390	34.5	279.8
B100 Si55	3.7	100	37	150	321	510	55	248 V	222	20	5	380	35.8	282.9
B100 Si60	3.8	100	38	150	307	537	60	263 V	228	20	5	390	37.1	281.2
B100 Si60 N25	3.7	100	37	150	315	522	60	265 V	226	18.75	6.25	390	37.9	251.7
B100 Si60 N25 1RPM	3.9	100	39	150	322	510	60	263	228	18.75	6.25	390	35.1	235.8
B100 Si60 N25 3RPM	3.7	100	37	150	315	522	60	265 V	226	18.75	6.25	390	37.9	251.7
B100 Si60 N25 6RPM	3.7	100	37	150	323	509	60	253	237	18.75	6.25	385	38.9	277.6

5.2 Effect of Bias Voltage Applied at the Substrate on Coating Properties

By varying the bias voltage applied to the substrate during the deposition of TiSiN films, the relationship between bias voltage applied at the substrate and coating properties were explored. Coating properties investigated included deposition rate, surface roughness, hardness (nanoindentation), wear resistance (tribology), chemical composition (XPS), investigation of crystal structure (XRD), and residual stress analysis.

5.2.1 Effect of Bias Voltage on Deposition Rate and Surface Roughness

With increasing bias, the surface of the coatings are bombarded increasingly with ions during their deposition. As a result, re-sputtering of the film surface continually occurs throughout the deposition process of the film. [92] While this is known to refine the microstructure and break up the columnar structure commonly found in samples deposited via PVD, it can also drastically decrease the sputtering rate, thus reducing the thickness of the as-deposited films. It has also been shown that a bias applied at the substrate can decrease the surface roughness of coatings deposited using PVD. [87, 93] Although the relationship between bias voltage and deposition rate was not of key importance in this work, and the interest instead resided in the relationship between processing conditions, mechanical properties, and coating microstructure, the relationship between bias, deposition rate, and surface roughness was explored to gain a clearer understanding of the coating deposition process.

In the current work, increasing substrate bias was found to decrease the deposition rate, but have no effect on the surface roughness of the TiSiN coatings. This relationship can be seen in Figure 5-1 on page 61. *It should be mentioned that the data points for bias voltage from 200 V through 500 V were taken from films deposited with a power of 65 W applied to the Si magnetron, but the data point at 100 V bias voltage was taken from B100 Si60, where only 60 W of power was applied to the Si magnetron. The

Si power was adjusted when it became clear that a well-established relationship between bias voltage applied at the substrate and Si content existed, with decreasing bias voltage leading to an increase in Si content.

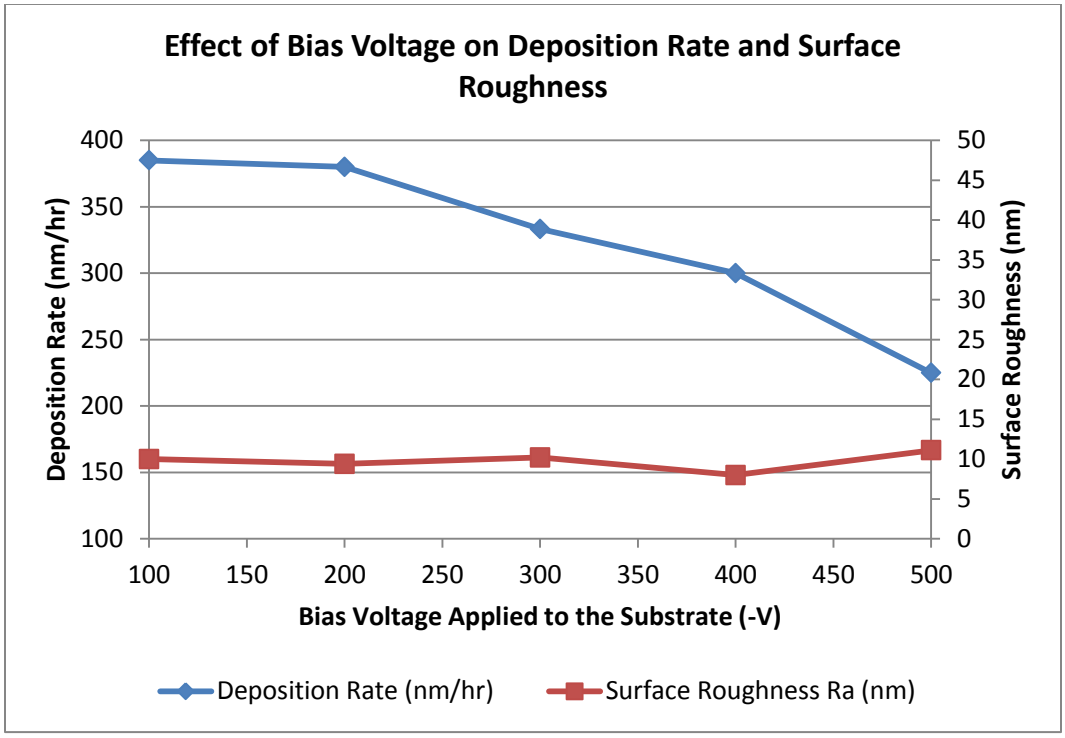

Figure 5-1 Deposition rate and surface roughness as a function of bias voltage applied at the substrate

As previously mentioned, the surface roughness varied minimally as substrate bias was varied for the TiSiN coatings. The value for R_a was calculated using the optical profilometer and Veeco software as previously described in Chapter 4, and the values were consistently near 10 nm, as can be seen in Figure 5-1. The low surface roughness as compared to the previously discussed Arc TiSiN samples is likely a result of lower deposition rate, yielding a smoother coating. In addition, the high energy processes employed in Arc Sputtering encourage the ejection of larger groups of atoms from the target material as compared to methods such as reactive PVD magnetron sputtering.

This could easily contribute to the increased surface roughness observed in the Arc TiSiN coatings. An example of a surface profile displaying the surface roughness of the coating deposited with 300 V bias on the substrate (coating 300B 65Si), obtained from the optical profilometer can be seen in Figure 5-2 on page 62. In this image, an area of approximately 1.2 x 0.9 mm is displayed. The roughness displayed in this image is representative of the roughness of each of the coatings produced.

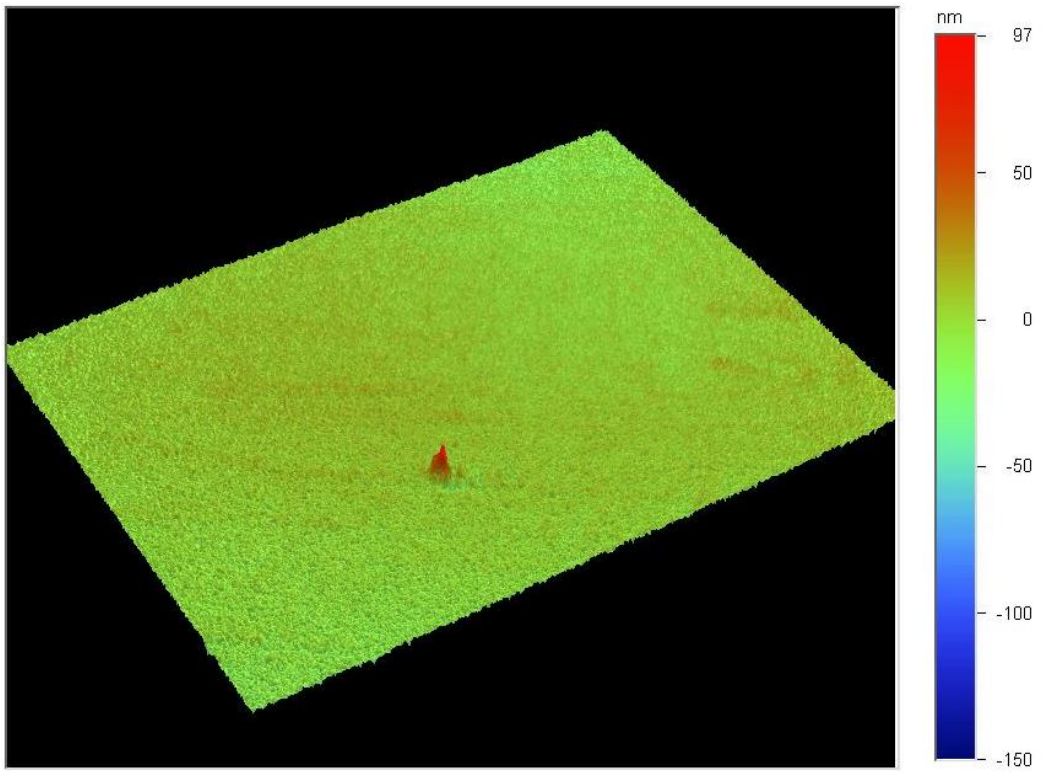

Figure 5-2 Surface roughness of TiSiN coating produced using 300 V bias applied to the substrate. This example is representative of the surface roughness of all coatings produced in this series.

5.2.2 Crystal Structure and Grain Size

XRD was used to determine the crystalline phases present in the as deposited TiSiN films. Figure 5-4 on page 65 shows the low angle scans taken at an incidence

angle of 5 degrees. It is apparent that increasing bias voltage results in a shift of the preferred orientation of the TiN within the films. While coatings B100 Si60 and B200 Si65 both display a preferred orientation of (200), the preferred orientation in the higher bias films shifts instead to (111). FCC TiN was identified in every film, regardless of bias voltage applied. However, with bias voltage of 300-500 V, the presence of a (TiSi)N FCC phase emerged. The FCC (TiSi)N phase is present with increasing prominence as the bias is increased in the series, suggesting that increasing bias or energy applied to the substrate results in the formation of increasing amounts of Si being incorporated into the FCC lattice. The lattice constant of the FCC TiN was calculated to be 4.23 Å, and the lattice parameter of the FCC (TiSi)N phase was calculated to be 4.08 Å, about 3% less than the TiN crystalline phase. This change in lattice parameter is nearly identical to that reported in Chapter 4, indicating a possible similar mechanism for the formation of this phase.

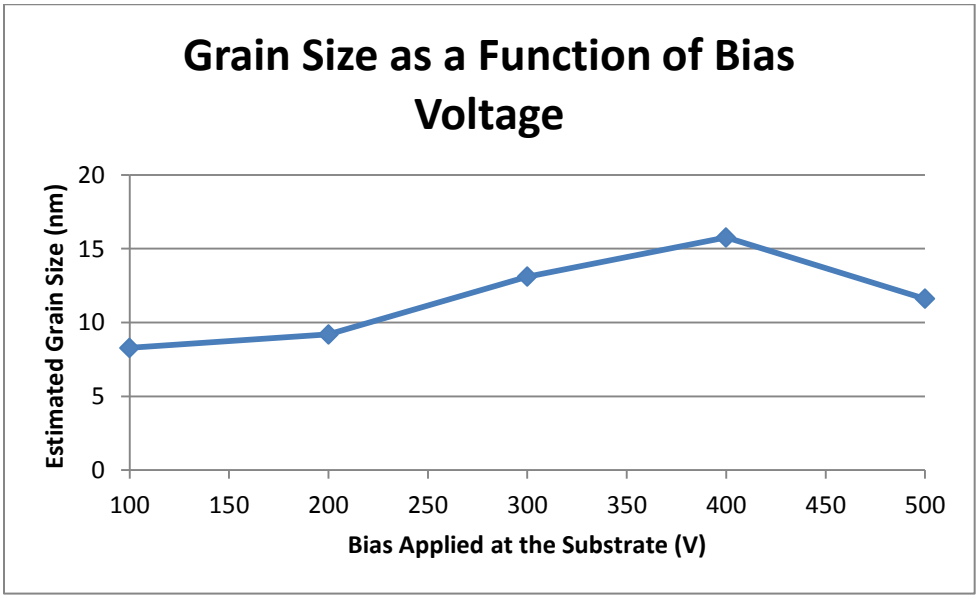

Figure 5-3 Grain size as a function of bias voltage applied to the substrate during coating deposition, estimated using the Scherrer formula

In the PVD Magnetron system, this (TiSi)N phase increases in prominence as bias voltage and the presence of energy and ion bombardment of the substrate, increases. In the Arc system, similar high levels of energy are present at the substrate due to the nature of the coating deposition process. Thus, it is logical that the incorporation of Si into the FCC TiN crystal lattice may occur as a result of the high energy processes employed in coating deposition, encouraging the energetic incorporation of Si into the TiN structure.

The Scherrer formula was used to estimate the grain size of the TiN crystalline phase in each of the films, as described in Chapter 3. According to this estimation, there was little variation in the grain size as a function of bias voltage. Figure 5-3 on page 63 shows that all coatings have an estimated grain size between 8 and 14 nm, regardless of the bias voltage applied at the substrate. There does appear to be a small increase in grain size as bias voltage is increased from 100 V to 400 V, and then the grain size decreases slightly when bias is increased to 500 V. While at first glance, this suggests that the highest bias condition may begin to refine the microstructure of the coatings, it should be noted that other sources of peak broadening, such as the presence of residual stress, may be coming into play in this estimate. This will be discussed in more detail shortly. Based on the estimation shown in Chapter 2 which correlates grain size and Si content (at%) necessary to achieve one amorphous monolayer of amorphous Si_3N_4, approximately 6-14 at% of Si would be necessary for the formation of the proposed microstructure.

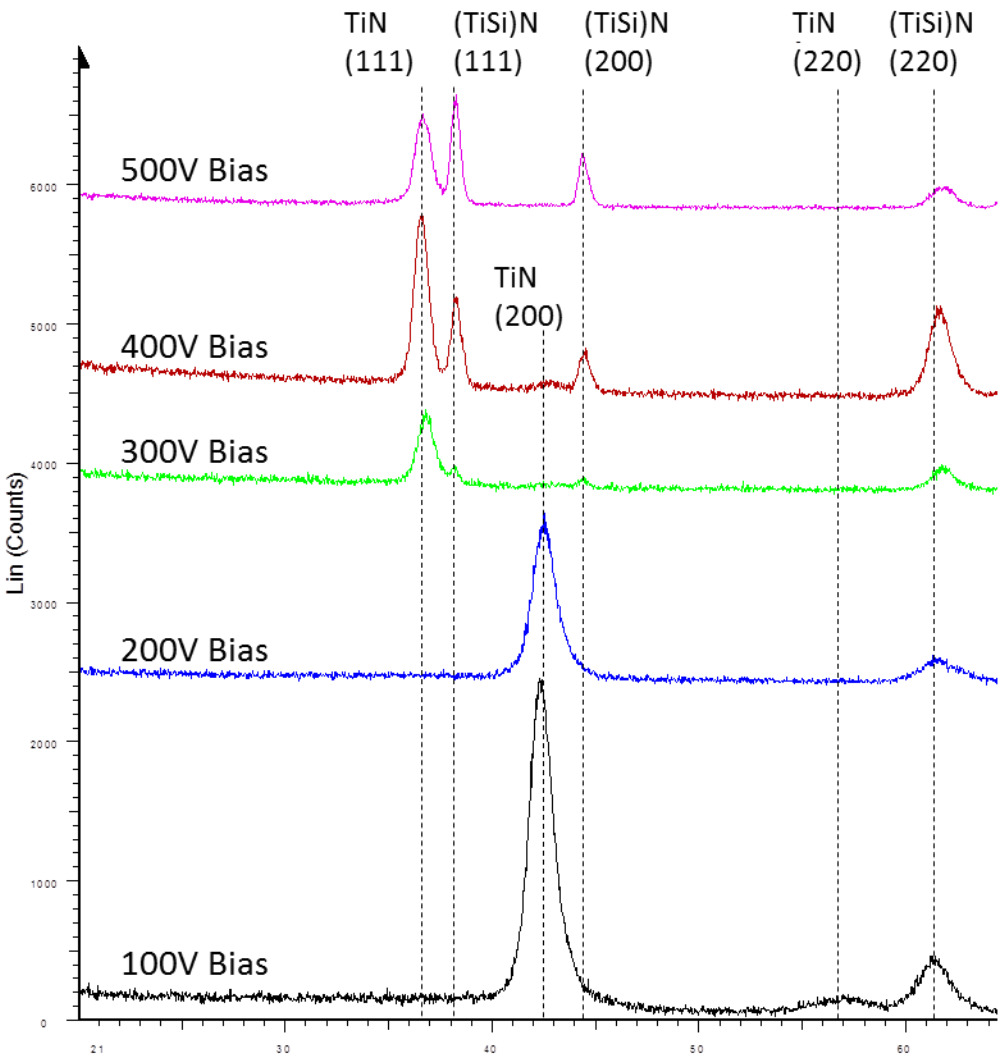

Figure 5-4 Low Angle XRD Patterns for TiSiN samples with substrate bias voltage varying between 100 V and 500 V

From XPS data from other TiSiN coatings not discussed in this document, it is known that increased bias applied at the substrate results in decreasing Si content within the TiSiN films. From these studies, it appears that while the initial 6-8 at% of Si serves to form the amorphous monolayer between TiN grains, additional Si content may become incorporated into the TiN FCC crystal lattice, but only when bias voltage is sufficiently

high. As previously mentioned, it is likely that the incorporation of this (TiSi)N phase into the microstructure is made possible at high energy conditions, and for that reason, it becomes more predominant as bias voltage is increased. In fact, in other preliminary experiments using 72 W of power to the Si target not reported here, TiSiN crystalline phases were seen in all bias voltages above 500 V, further supporting the combined role of increased bias voltage and Si content in excess of the required 6-8 at% in the formation of the nanocrystalline FCC TiSiN phase.

5.2.3 Effect of Bias Voltage on Coating Mechanical Properties

Bias voltage was varied in order to assess the effect of the additional energy applied to the substrate on the mechanical properties of the coatings. The original hypothesis for this work stated that increasing bias may result in increased hardness due to increased re-sputtering effects and refinement of the microstructure at the surface of the coating during deposition. It was hypothesized that this energetic bombardment would reduce the columnar effect commonly seen in PVD methods and more closely resemble Veprek's nc-TiN/a-Si_3N_4 proposed model. In fact, however, it was found that decreased substrate bias resulted in samples with greater hardness. These findings will be discussed in detail in the following text.

5.2.3.1 Hardness as a function of Bias Voltage

Nanoindentation was performed on the coatings of varying substrate bias. The average hardness was obtained from an average of nine indentation points. This was done at several locations for each sample, to ensure uniformity. The standard deviation of each data set was also found and calculated for each bias voltage. It was found that increasing the bias to the substrate reduced the hardness of the coatings from over 37 GPa in the case of coating 100B 60Si to under 20 GPa for coating 500B 65Si, as can be

seen in Figure 5-5 on page 67. In addition, the experimentally measured modulus decreased in value as the bias voltage applied to the substrate was increased.

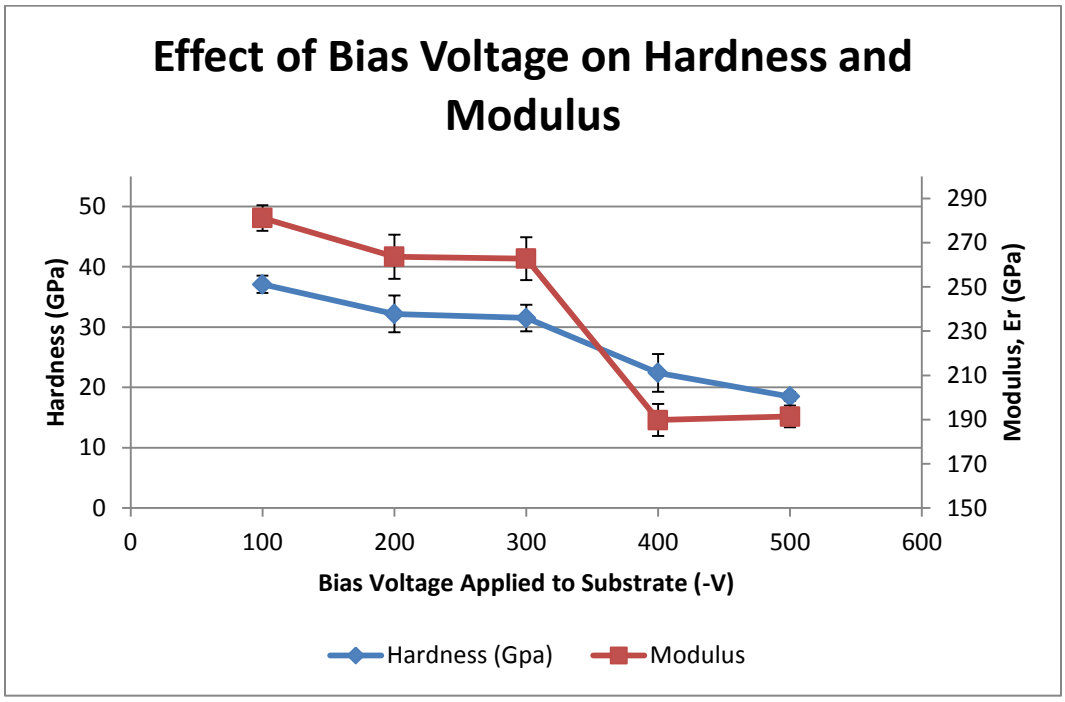

Figure 5-5 Effect of bias voltage on TiSiN coating hardness, as measured by nanoindentation

While it was originally suspected that an increase in the bias voltage would have a positive impact on mechanical properties of the TiSiN films, including hardness, the opposite was found to be true in this case. It seems that although increasing the bias voltage encourages the coatings to become less textured, switching from a primarily (200) orientation to contain FCC orientations including additional orientations of (111) and (220), some negative effects occur simultaneously. These negative effects could include excessive ion bombardement, resulting in changes to the microstructure yielding less overall mechanical strength.

Figure 5-6 on page 68 shows a typical example of a nano-indentation loading and unloading curve for a depth-controlled indentation test. With increasing bias voltage and decreasing hardness, the overall loading (in uN) decreases, as expected. However, other changes to the loading and unloading process take place as well. The shapes of the curves are significantly different for the 100 V bias and the 400 V bias TiSiN samples with identical indentation depths. The elastic portion makes up a higher percentage of the total unloading curve in the lower bias, higher hardness samples, as compared to the higher bias, lower hardness samples, indicating the increased presence of elastic recovery mechanism in the high hardness samples.

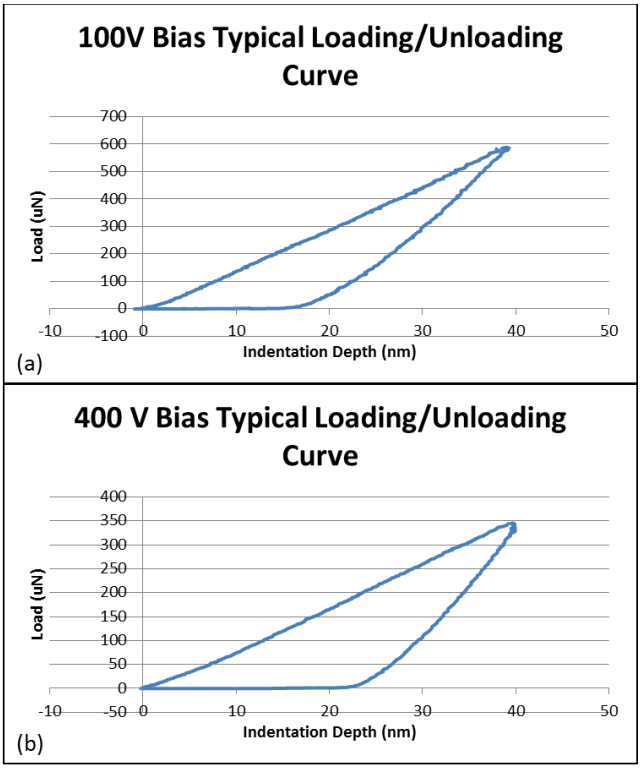

Figure 5-6 Examples of typical loading/unloading curves for varying bias TiSiN coatings, displaying the difference in the unloading mechanisms with increased bias voltage (a) 100 V bias curve, (b) 400 V bias curve

This trend continues for the remainder of the varying bias series. Figure 5-7 on page 69 displays the average percent elastic unloading for the 100 V through 500 V bias films showing the overall trend of decreasing elastic deformation mechanism with increasing bias and decreasing hardness. The percent elastic deformation was calculated as the portion of elastic deformation over the total deformation. The elastic portion of the unloading curve was defined between the points of the beginning of the unload and the point at which the unloading curve returns to zero load.

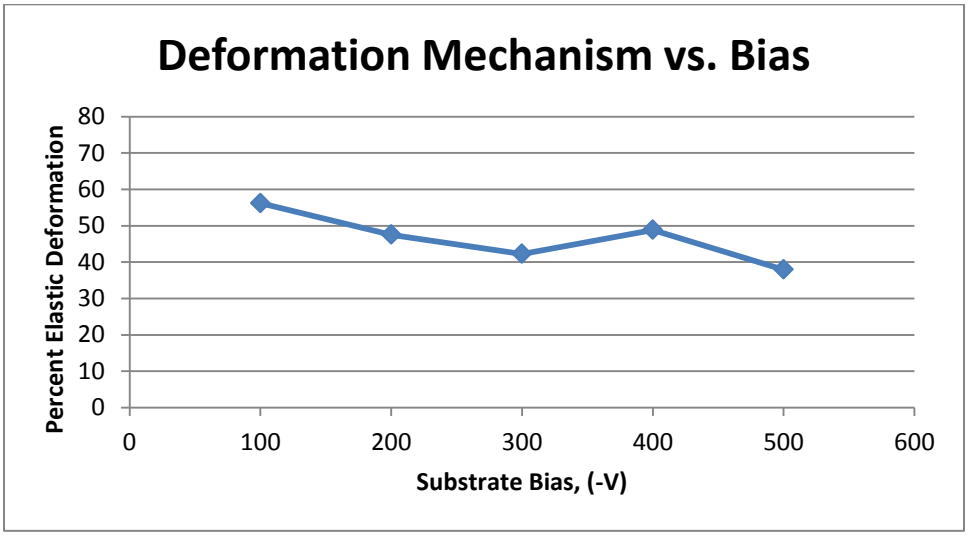

Figure 5-7 Percent of deformation during nanoindentation associated with elastic deformation as a function of bias voltage applied during coating processing

5.2.3.2 Residual Stress as a function of Bias Voltage

Using the optical profilometer, the radius of curvature was calculated on uncoated Si wafers before film deposition and on the coatings after deposition. With the presence of residual stress within the TiSiN films, some curvature will be induced onto the Si wafer. The difference in the curvature of the wafer before and after TiSiN coating deposition was used in order to calculate the stresses present within each film using Stoney's Equation, previously described in Chapter 3.

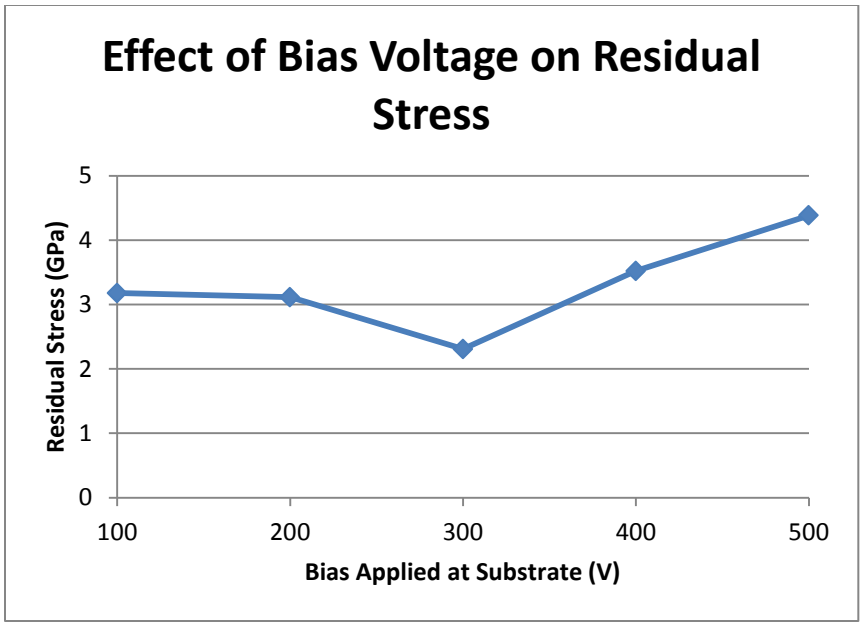

Figure 5-8 Estimate of residual stress within varying bias TiSiN coatings, as estimated using Stoney's equation

Figure 5-8 on page 70 shows the residual stresses calculated using this method, for varying bias voltage. It appears that there is an initial decrease in the values of experimentally measured residual stress starting at -300 V bias, and then the residual stress steadily increases as bias voltage is increased to -500 V. This could be explained by both the shift in preferred orientation from (200) to (111) that occurs at -300 V bias as well as the appearance of the (TiSi)N phase in the (111) and the (200) orientation. The increase in prominence of the (TiSi)N phase as bias is further increased, however seems to increase the stresses within the crystal structure. This additional energy allows atoms to deposit in orientations and fashions that would not normally be energetically favorable or possible. After deposition, this translates into greater presence of residual stress within the coatings and easily measurable curvature induced onto the Si wafer substrate. This result is consistent with that found in the Arc coatings, which displayed properties

indicating higher residual stresses as the (TiSi)N FCC phase increased in prominence. In addition, the overall relationship of decreasing residual stress with decreasing bias voltage and increasing hardness indicates that the high hardness present in the lower bias coatings is not in fact due to residual stress accumulated in the films as a result of the deposition process.

5.2.3.3 Tribological Properties as a function of Bias Voltage

Additionally, the wear rate on the TiSiN films after tribological testing was assessed using the optical profilometer. Wear tracks were imaged in 2 and 3 dimensions. The 2-dimensional wear tracks were used to calculate the wear rate of each TiSiN coating. Examples of these 2-D wear tracks for two low bias (100 V and 200 V) and a high bias (500 V) coating can be seen in Figure 5-9 on page 73.

Table 5-2 Experimentally measured tribological properties as a function of applied bias voltage to the substrate during film deposition

Bias (-V)	Wear Track radius (mm)	Wear track depth (nm)	Wear Track width (um)	Wear Rate (mm^3/Nm)	Coefficient of friction, μ
100	16	104	156	7.4E-06	0.82
200	16	90	97	2.7E-06	0.24
300	27	60	80	2.3E-06	0.19
400	27	210	85	4.5E-06	0.21
500	31	190	80	4.8E-06	0.18

From these examples, the difference in wear mechanism is immediately apparent. In the highest bias film the 2-D wear track shows a steep, deep wear track. The wear track for the -200 V and -300 V bias, on the other hand, is shallow and uniform in depth. This is indicative of a good tribological coating. In the case of the 100 V bias

coating, the wear track was deeper, as well as wider, with irregular wear along the bottom of the track. In fact, in Figure 5-9 (a), a large peak can be seen in the center of the 2-D representation of the wear track. This peak is actually a piece of debris, presumably from the Al_2O_3 ball, present in the track immediately after the wear test was completed. The hardness of alumina is approximately 20.5 GPa. These differences in wear mechanism, along with the fact that this was ceramic on ceramic wear testing, indicate the possibility of an introduction of 3-body wear as the hardness of the TiSiN coatings reaches values in excess of 35 GPa. This type of relationship was in fact found in all samples with hardness above 35 GPa, and it will be discussed in more detail later in this chapter. The three-dimensional wear tracks for bias voltages 200, 300, 400, and 500 V can be seen in Figure 5-11 on page 75 and the wear rate, coefficient of friction, and wear track dimensions as a function of bias voltage for the 100 through 500 V bias are listed in Table 5-2 on page 71.

Three-dimensional wear tracks obtained using the optical profilometer show a portion of the wear tracks for the 200 V – 500 V substrate bias coatings. A larger view of the 100 V bias wear track to accentuate the presence and visibility of debris can be seen in Figure 5-10 on page 74. The three-dimensional view displays a larger area, and a larger portion of the wear tracks can be seen than in the two-dimensional view. This view again shows the difference in wear mechanism with increasing bias and decreasing hardness.

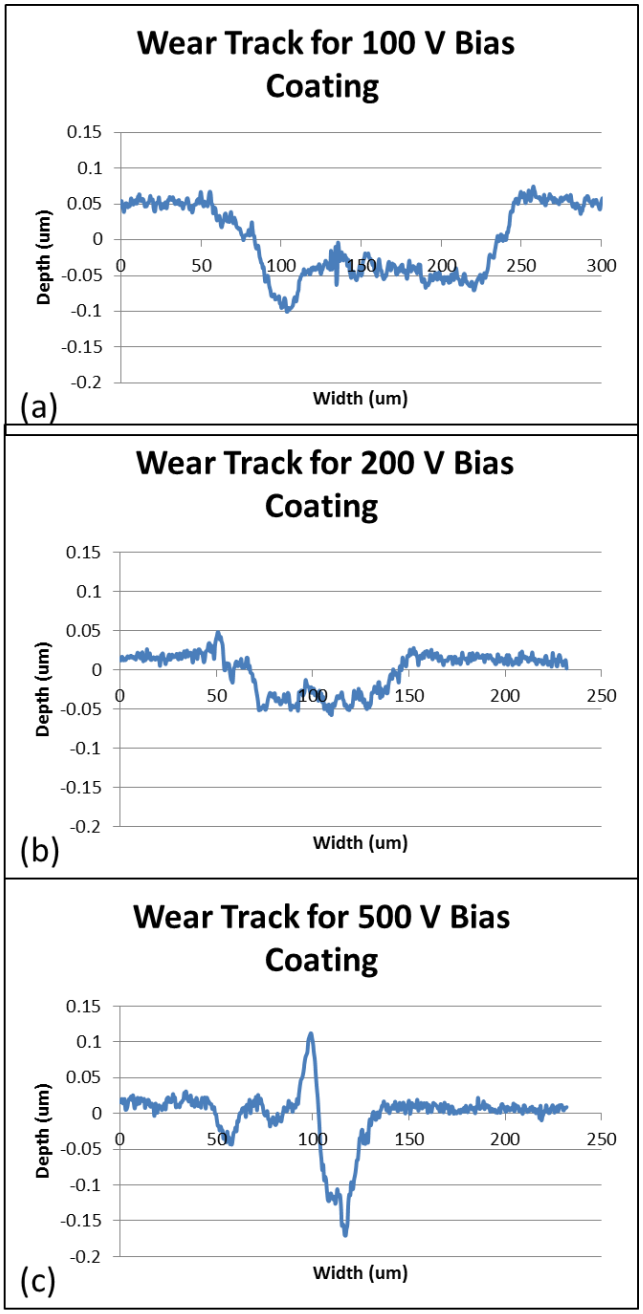

Figure 5-9 2-D representations of wear tracks from a typical (a) 100 V bias and (b) 200 V bias and (c) 500 V bias voltage TiSiN coating tribological experiment

The general trend observed consisted of lower wear rates for increasingly hard coatings. However, this did not hold true for the hardest film. In the case of the -100 V bias TiSiN coating with a hardness of over 36 GPa, the wear rate of the film was actually the greatest. On all films with hardness over 35 GPa, white debris was apparent within the wear tracks upon completion of the tribological testing, and the observed coefficient of friction was very high, at values > 0.7. It is likely that the high hardness of the films contributed to excessive wear on the alumina ball, resulting in the white debris seen on the wear tracks as well as the higher coefficient of friction due to a three body wear system involving powder-like debris from the alumina ball. This powder-like debris present within the wear tracks could have led to greater wear of the film during tribological testing. A three dimensional view of the wear track from the 100V bias TiSiN coating can be seen in Figure 5-10 on page 74. From this figure, some wear debris is clearly evident near the center of the track.

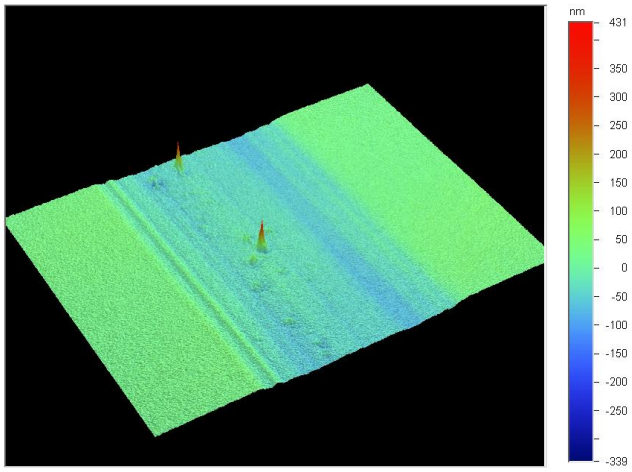

Figure 5-10 Wear track for 100 V Bias TiSiN coating, with wear debris within the track

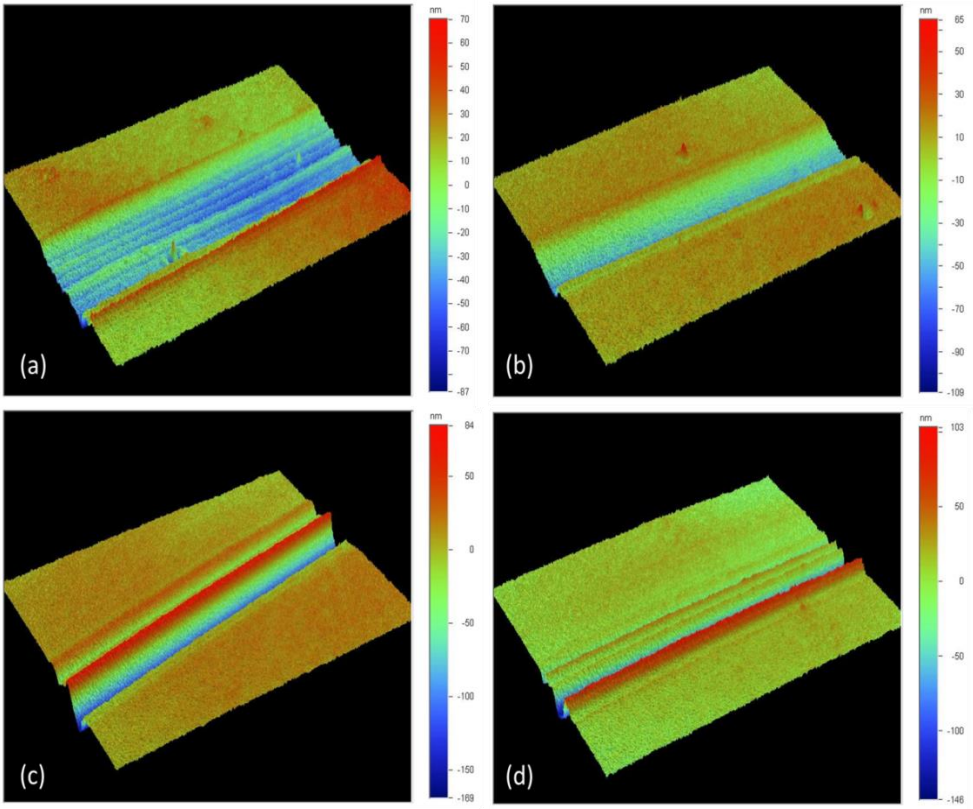

Figure 5-11 Wear tracks for (a) 200 V (b) 300 V (c) 400 V and (d) 500 V bias applied to the substrate TiSiN coatings

5.2.3.4 Summary of Effect of Bias Voltage on Mechanical Properties in Magnetron Sputtered TiSiN Films

The effect of increased bias voltage on PVD Magnetron sputtered TiSiN films was explored in terms of hardness measurements, estimation of elastic and plastic deformation, estimation of residual stresses present in the films, and tribological wear testing. In general, it was consistently found across these various methods that lower presence of bias voltage during coating deposition yielded coatings with properties making them more desirable for use as tribological coatings. Contrary to this trend were the high wear rates and coefficient of friction found in the coating processed using 100 V

of bias. It is possible due to the high hardness of this coating of above 35 GPa that the ceramic-on-ceramic pin-on-disk tribological test caused excessive wear on the alumina ball, resulting in powder-like alumina debris within the wear track. The presence of this debris likely caused a 3-body wear system scenario to occur, thus raising the experimentally measured wear rate and coefficient of friction, particularly in cases such that the hardness of the coatings far exceeded the hardness of the alumina ball used for the wear testing.

While XRD showed a decrease in texturing for the higher bias coatings, these coatings displayed greatly reduced hardness as compared to the coatings deposited at lower bias voltage, which exhibited a predominantly (200) textured structure. This indicates that randomly oriented crystalline TiN with nanoscale dimensions are not necessarily required in order to achieve high hardness coatings, but instead, desirable mechanical properties can be achieved with a textured coating with primarily (200) orientation. Critical analysis of the Low Angle XRD, nano-indentation, and residual stress data suggest that the shift in preferred orientation from the less dense (200) FCC orientation to the more dense (111) orientation may initially occur between 200 and 300 V bias in order to relax the crystal structure, due to the emergence of an increasingly predominant (TiSi)N FCC crystal phase as bias voltage is increased. As the predominance of this phase continues to rise with bias voltages of 400 V and 500 V however, the (TiSi)N phase's increasing presence increases the residual stresses present within the coatings, as well as decreasing the overall hardness and modulus of the films. This result is further supported by the presence of a (TiSi)N phase within the Arc-deposited coatings with nearly identical lattice parameter as seen in the PVD Magnetron sputtered films, as well as high presence of residual stresses. This suggests that increased presence of Si incorporation into the TiN FCC lattice becomes possible as

the energy present at the substrate during the deposition process is increased, since the Arc-deposition process is quite high in energy. In addition, an overall trend of increased elastic deformation was found as bias voltage was reduced and hardness was increased in the coatings. The mechanism of hardness enhancement in the PVD Magnetron Sputtered TiSiN films will be discussed in more detail and supported with TEM and HRTEM micrographs later in this chapter.

Residual stress was estimated for the coatings deposited at bias voltages between 100 V and 500 V, and it was found that residual stress present within the coatings increased with increasing bias voltage, although there was a drop in estimated residual stress values for the 300 V bias coating. This drop likely occurred due to the shift in preferred orientation of the crystal structure from (200) in the lower bias coatings to (111) in the higher bias coatings. The overall trend signifies that hardness enhancement is due primarily to the microstructure of the coatings, and not increased residual stresses. Residual stress is likely more prominent in the higher bias coatings due to the high amount of energy present at the substrate encouraging atomic interactions and the formation of the FCC (TiSi)N phase which would not normally be favorable at conditions closer to equilibrium. After the deposition is completed and the bias is no longer present, the atomic structures which were made possible by the excess energy presence at the substrate cause the presence of increased residual stress. This stress is easily estimated by measuring the radius of curvature of the Si substrate after the deposition process is completed.

The increased prominence of elastic deformation in the higher hardness coatings suggests that dislocations which occur during loading and are later reversed play a major role in the hardness enhancement of these coatings. In addition, the higher presence of plastic deformation mechanisms in the higher bias coatings could likely be due to the

presence of increased residual stresses within the coating material. As these coatings are indented, some of the residual stresses imposed by the high bias deposition conditions could be relieved. This would contribute a higher percentage of permanent, plastic deformation and less overall elastic recovery during the unloading of these coatings.

Overall, there seems to be a high degree of inter-relation between various properties as the bias voltage of the coatings is increased from 100 V to 500 V. Perhaps most importantly, the hardness and modulus both show significant decrease with increasing bias voltage, with the coatings processed using the lowest bias possessing the highest hardness of 37.1 GPa and the highest modulus of 281.2 GPa. This hardness can not, however be attributed to the bias voltage processing condition alone. Instead, it is intimately related to other by-products of the bias voltage applied such as the varying degree of presence of FCC TiN and (TiSi)N phases, a change in the preferred orientation of the crystal structure, a variance in the residual stresses present within the coatings, and a change in the percentage of the elastic deformation percentage. These relationships and parameters will be continually discussed throughout the remainder of this document.

5.3 Varying Si power and N_2 ratio for TiSiN coatings deposited with 100V Substrate Bias

After determining the effect of bias voltage on coating hardness, the conditions yielding the coatings with the highest hardness were fine-tuned in order to further enhance the hardness of the as deposited material. In particular, the power to the magnetron gun containing the Si target and the N_2/Ar flow ratio were adjusted in an attempt to increase the hardness of the coatings as much as possible. Coatings were deposited at 50 W, 55 W, and 60 W to the magnetron gun containing the Si target. After determining that the highest power Si coating had the highest hardness, the N_2/Ar ratio

was adjusted from 20% to 25% N_2. This was found to further increase the hardness of the TiSiN coating.

5.3.1 Effect of Si power on Deposition Rate and Surface Roughness

In the case of adjusting the parameters including power to the Si magnetron and Nitrogen gas flow ratio, no significant changes to the deposition rate or to the surface roughness occurred. Deposition rates for all films in this series were very close to 400 nm/h, and surface roughness was always very close to R_a = 10 nm. Since the Si content in the coatings is relatively low as compared to the Ti content, it makes sense that adjusting the power to the Si magnetron would have little impact on the overall thickness of the coating. Surface topography and roughness were consistent with coatings processed in the previously discussed series of coatings in which the bias voltage was varied, and all coatings appeared similar in surface roughness as shown in Figure 5-2 on 62.

5.3.2 X-Ray Diffraction and Grain Size for varying Si and N_2

Figure 5-12 on page 80 shows low angle X-Ray diffraction at a 5˚ incident angle coatings B100 Si50, B100 Si55, B100 Si60, and B100 Si60 25N2. In the case of all coatings, FCC TiN is present with a lattice parameter of a = 4.23 Å. Also present was a (TiSi)N FCC phase with Si substituting for Ti within the crystal lattice. In the case of the B100 Si50 coating, the presence of this (TiSi)N phase is more prominent as compared to the other coatings, and the intensity of the peaks representing the FCC TiN phase are greatly decreased. While it initially seems counter-intuitive that decreasing the power to the Si magnetron would result in increased presence of Si within the FCC TiN lattice, it is likely that a relationship exists between the residual stresses, the texturing, the presence of the (TiSi)N phase, and the mechanical properties in which there is a great deal of inter-relation. This will be discussed in more detail shortly. For all coatings in which the FCC

(TiSi)N phase was present, the lattice parameter for this phase was calculated from the XRD peaks to be between a = 4.06-4.08 Å, a change of approximately 3-3.5% from the FCC TiN phase. When considering the three coatings where power to the Si target was varied, it can be seen that higher power to the Si target resulted in more textured samples, with the (200) orientation being prominent.

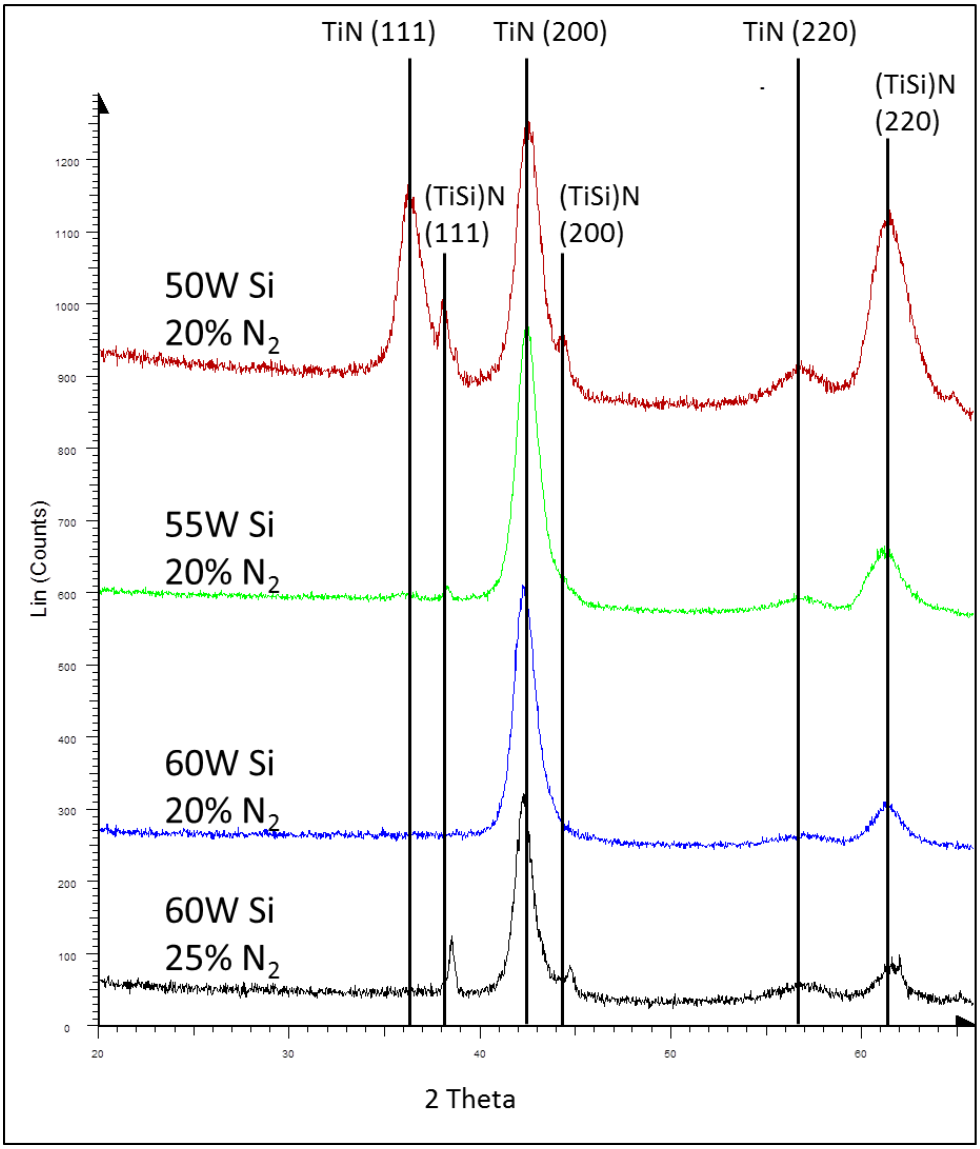

Figure 5-12 Low Angle XRD of varying Si TiSiN series

The Scherrer formula was used to estimate the grain size in the as-deposited TiSiN coatings. The results can be seen in Figure 5-13 on page 81. Similarly to the result presented in the previous section on the varying bias films, power to the Si gun and N_2 flow ratio had minimal effects on the estimated grain size within the films. While it appears that the increased N_2 flow may have had a slight effect on grain size, increasing the estimated grain size somewhat as compared to the film with identical conditions and a lower Nitrogen flow, all films had an estimated grain size between 8 and 11 nm.

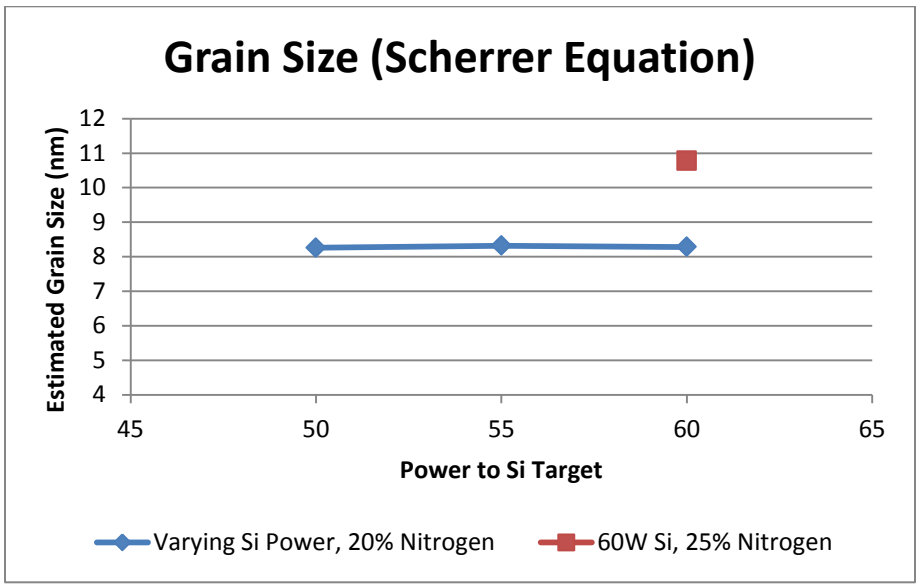

Figure 5-13 Grain size, as estimated using the Scherrer Equation in the varying Si TiSiN series

5.3.3 Effect of varying Si and N_2 on mechanical properties

Using nanoindentation, residual stress estimation methods, and tribological testing, the effects of varying Si and N_2 were determined for this series of TiSiN coatings. Since there was little variation in the deposition parameters, the changes to the mechanical properties of the coatings were much more modest than the effects presented in the previous section, but the effects were still apparent.

5.3.3.1 Effect of Varying Si and N_2 on hardness

Decreased power to the magnetron gun containing the Si target had a small, but clear effect on the hardness of the TiSiN coatings. With increased Si power, an increase in hardness was observed, Figure 5-14 on page 83. Once the relationship of power to the Si target and coating hardness was understood, the conditions yielding the hardest sample (B100 Si60) were slightly modified with higher N_2 flow rate in order to assess the effects of increased Nitrogen content in the gas mixture on coating mechanical properties. This was performed because it was believed based on XPS results not discussed here that preferential sputtering of N_2 away from the coatings were occurring during deposition. Therefore, the percentage of N_2 gas in the mixture was adjusted in an attempt to compensate for this effect. Little effect was seen on the measured molulus of the coatings as power to the Si target was varied, Figure 5-15 on page 83. When the Nitrogen ratio was increased from 20 to 25% however, the modulus was measurably reduced by a value of statistical significance. In order to develop ideal tribological coatings, both the hardness and the modulus should be considered. While a high hardness certainly contributes to excellent wear resistance, it has also been suggested that a reduction in the modulus can lead to more desirable tribological performance due to reduced elasticity in the coating. For these reasons, conditions including 60 W of RF power to the Si target with 25% N_2 in the gas mixture were used in the final series of TiSiN films with varying substrate rotation. This final series of TiSiN coatings will be discussed in detail shortly.

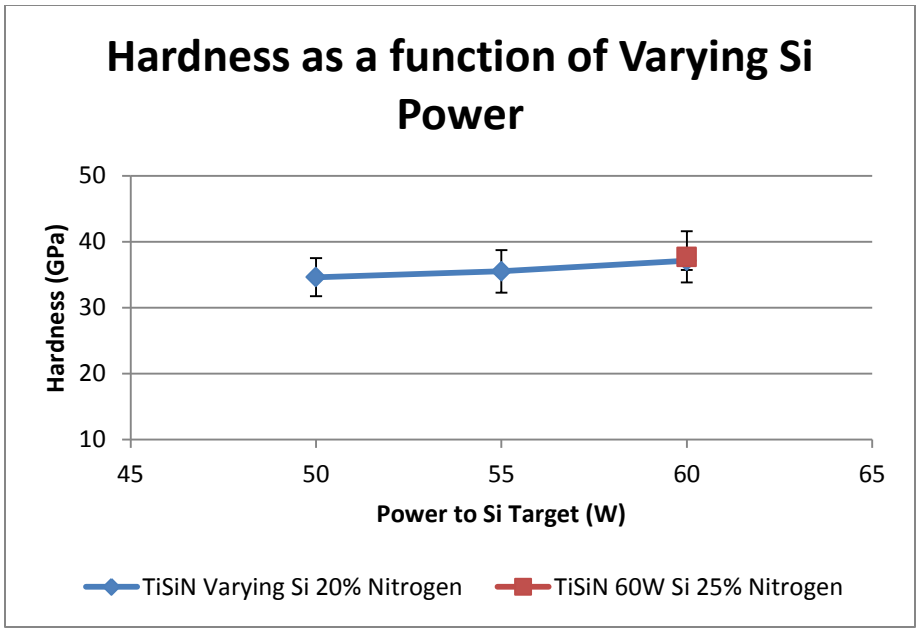

Figure 5-14 Hardness, as measured by nanoindentation, with varying power to the Si target and varying Nitrogen content

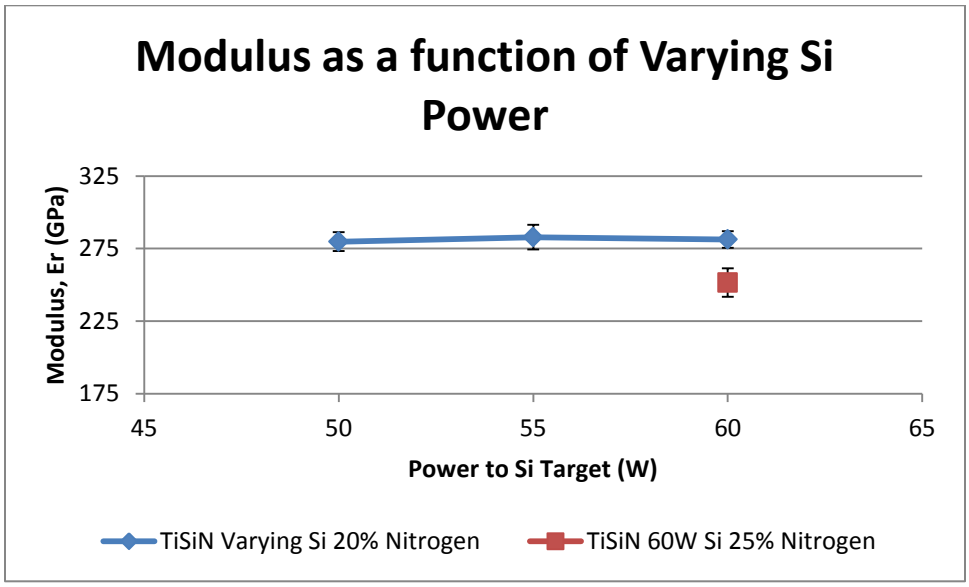

Figure 5-15 Modulus as a function of varying power to Si target and varied N_2 content in the gas mixture

The presence of elastic and plastic deformation was again investigated for this series of coatings. No major effects were seen on the percentage of the unloading curve associated with the elastic deformation or the general characteristics of the loading and unloading curves, regardless of power to the Si magnetron gun or N_2 flow ratio during the deposition of the coatings. For every film produced in this series, the average percentage of elastic deformation was between 58 and 62%.

5.3.3.2 Effect of Si and N_2 on residual stress

The residual stress was estimated from the radius of curvature of the substrate before and after coating deposition for the TiSiN coatings. Compared to the previously discussed TiSiN coating series with varying substrate bias, the effects of Si and N_2 variation on residual stress were very minimal. This reinforces the conclusion drawn from the series of magnetron sputtered coatings with varying bias and the Arc coatings that increased energetic presence encourages unusual atomic arrangements due to deposition conditions far from equilibrium, thus greatly impacting the residual stress within the films. It is clear from the varying Si and N_2 series that slight variations to the amounts of silicon and nitrogen ions present in the plasma has only a small effect on the residual stresses, as compared to the effects induced by varying bias voltage. There is a noticeable change, however, in the prominence of texturing and of the (TiSi)N phase within the coatings as Si content is varied. The increased presence of the (TiSi)N phase at conditions of lower power to the Si target seems initially counter intuitive, but upon closer inspection of the data, levels of texturing seem to be inversely related to both residual stress and the prominence of (TiSi)N within the coatings. A decreasing degree of texturing with decreasing Si content has been consistently reported amongst TiSiN academic publications. [46, 60, 63] Therefore, it could be possible that decreased levels of texturing, an increase in the amount of high angle grain boundaries, and an overall

increase in the residual stress of the coatings create conditions unfavorable at the locations of the TiN grain boundaries for the formation of amorphous Si phases, thus encouraging the Si to become incorporated into the FCC TiN lattice. This again supports the previously stated hypothesis that the relationship between the formation of the nc-TiN/a-Si_3N_4 may be quite a bit more complicated than simply achieving the required temperature for the chemical spiondal to exist. Instead, complex energetic interactions and residual stress conditions occurring both within the TiN grains as well as at the grain boundaries impact the location and the structure of the Si within the crystalline and amorphous components of the coating material. The overall relationship between residual stress and power to the Si magnetron can be seen in Figure 5-16 on page 85.

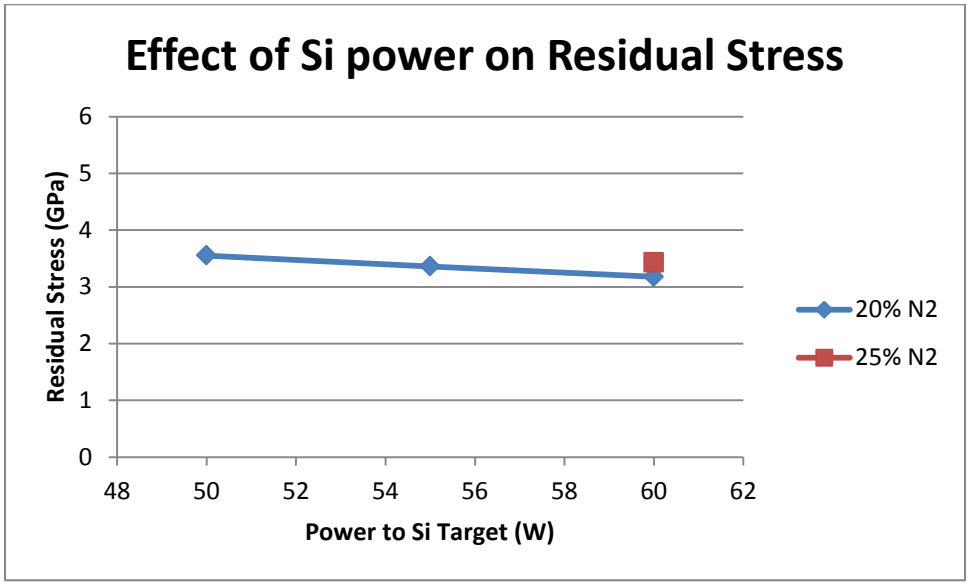

Figure 5-16 Residual stress, estimated using Stoney's Equation in the varying Si TiSiN series

5.3.3.3 Tribological Properties as a function of varying Si power and N_2 content

Tribological wear testing on the TiSiN series with varying power to the Si target showed high coefficient of friction, and a general trend of increasing wear rate with

increasing hardness. These results, along with the dimensions of the resulting wear tracks, are presented in Table 5-3 on page 86. As the softest film, B100 Si50, presented in this series still had very high hardness of nearly 35 GPa, it is probable that the comparably high wear rates and friction coefficients are due in part to debris from the alumina balls used in the tests, as hypothesized in the previous section.

Table 5-3 Tribological properties of TiSiN coatings with varying Si and N_2

Coating	Wear Track radius (mm)	Wear Track depth (nm)	Wear Track Width (um)	Wear Rate (mm^3/Nm)	Coefficient of friction, μ
B100 Si50	21	87	216	4.9E-06	0.47
B100 Si55	21	92	150	6.2E-06	0.74
B100 Si60	24	167	157	7.4E-06	0.82
B100 Si60 N25	21	140	174	7.3E-06	1.03

In the case of each film tested in this series, white debris was visible within the wear tracks of the TiSiN coatings. In fact, images obtained from the optical profilometer of the wear tracks from coatings B100Si50 and B100 Si60 N25, Figure 5-17 on page 87, clearly show the presence of a greater amount of debris within the wear track of the highest hardness coating produced with 60 W DC Power to the Si target as opposed to the comparatively softer coating produced with 50 W DC power to the Si target. This again supports the occurrence of a three-body wear system as hardness is increased in the TiSiN ceramic coatings, especially since the experimentally measured wear rate and the coefficient of friction both tend to increase with increasing coating hardness.

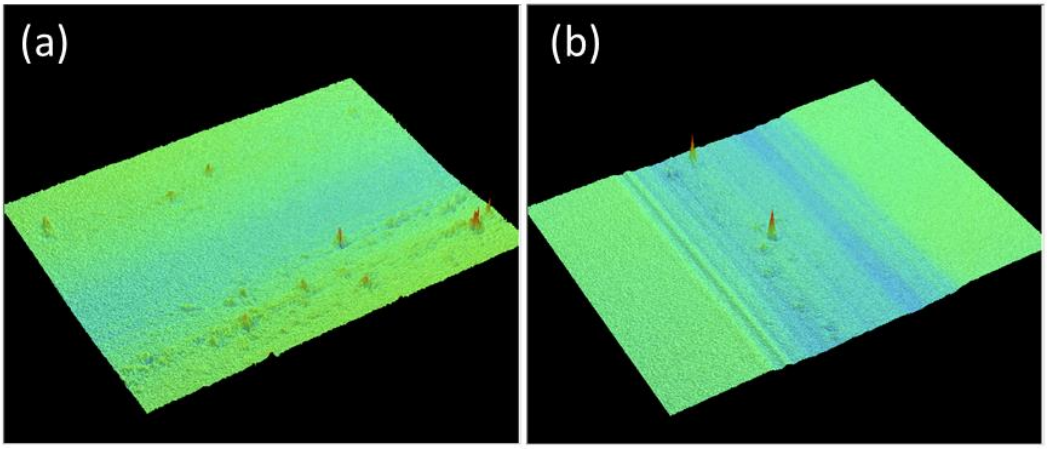

Figure 5-17 Wear tracks from coatings (a) B100 Si50 and (b) B100 Si60 N25

5.3.4 XPS

High resolution XPS was performed on the Nitrogen 1S peak of the B100 Si60 N25 TiSiN coating in an attempt to further support the presence of amorphous Si_3N_4 content. In fact, based on the deconvoluted peak shown in Figure 5-18 on page 88, TiN and Si_3N_4 peaks are clearly distinguished at binding energies of 396.5 and 398.3, respectively. This result, along with the presence of nano-crystalline morphology displaying compositional contrast within TEM micrographs, to be discussed shortly, combined provide quite convincing evidence of the existence of the presence of amorphous Si phases within the coatings. Due to repeated issues with breakdown of the XPS instrumentation experienced over the course of the last several months, only a limited amount of time was possible on this equipment. However, more XPS analysis will soon be under way involving a collaborator with these coatings.

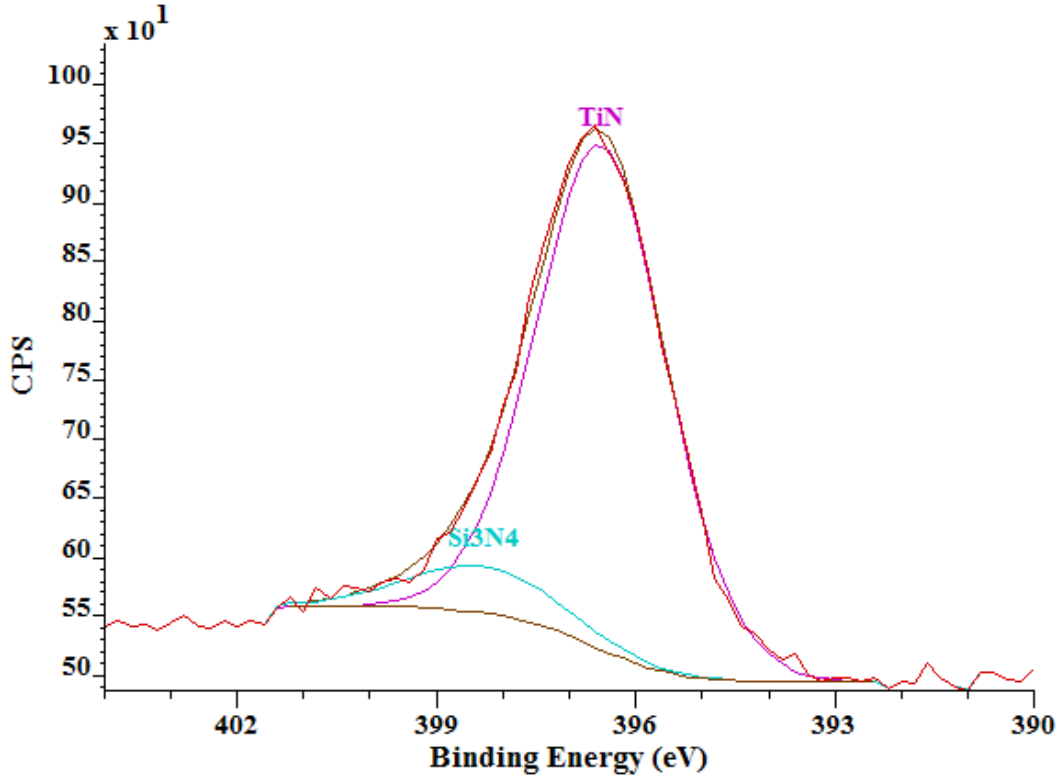

Figure 5-18 High Resolution XPS of the N1S peak, showing the presence of TiN and $S_{i3}N_4$ bonding

5.3.5 Summary of Effects of Varying Power to Si target and N_2 ratio

Overall, the effects of slight variations to the power applied to the Si target and to the N_2/Ar ratio were less pronounced, as compared to the obvious effects of bias voltage on the mechanical properties of the TiSiN coatings. This exercise, however, still provided some improvement in terms of coating hardness, as well as a more enhanced understanding of the quite involved relationships between coating texturing, residual stress, hardness, and the prominence of the (TiSi)N phase. With slight adjustment of the conditions identified during the study of the varying bias voltage series, the mechanical

properties of the TiSiN coatings were refined further, with a result of almost an additional GPa of hardness.

XRD showed no significant changes in grain size of the coatings with respect to Si target power or N_2 content. It did, however, show an increase in the (200) texturing with increasing Si power and increasing hardness. The relationship between increasing Si content within TiSiN coatings and the gradual increase in texturing and resulting shift in preferred orientation to TiN (200) has been previously established in the literature, so this relationship was not surprising. [46, 60, 63] However, FCC TiN and (TiSi)N with Si atoms substituting for some Ti atoms within the crystal lattice were identified using low angle X-Ray Diffraction at an incidence angle of 5°. The prominence of this (TiSi)N phase increased as the power to the Si target was decreased. While this result seems strange, since one might initially suspect that less Si present within the plasma cone would result in less prominence in the (TiSi)N crystal structure, it is clear that other factors play an important role in this relationship.

In particular, the residual stresses present seem to be highly related to the occurrence and prominence of the (TiSi)N FCC crystalline phase. This suggests the possibility that decreased texturing and more random orientation occur in tandem with increased residual stress and increased presence of crystalline (TiSi)N. This could be possible due to the presence of higher angle grain boundaries, which may lead to more residual stresses present in the coatings. Since the incorporation mechanism of Si into the coatings is obviously more complex than a simple temperature relationship due to a chemical spinodal, as previously proposed, it seems that the energetic interactions play a key role in the manner of Si location and structure within the nanocomposite TiSiN coating structure.

Hardness was slightly impacted as a function of RF power applied to the magnetron gun containing the Si target, with increasing Si content resulting in higher hardness. In addition, increased N_2 flow using identical conditions as the 100B 60Si film resulted in a slight improvement of the hardness, yielding a film with a hardness of 37.9 GPa. There was no clear effect on the average percentage of elastic deformation with variation in power to the Si target or N_2 ratio.

Tribological testing showed high coefficient of friction and high wear rates, competitively with the varying bias TiSiN series discussed earlier in this chapter. In every instance, the measured coefficient of friction was above 0.47, and the coating with highest measured hardness exhibited friction coefficient of over 1.0. After each tribological wear test, white residue/debris, presumably from the alumina ball used in the wear test, was found inside the wear track. Since the coating hardness is so high, the film could be causing significant wear to the alumina ball, resulting in alumina debris formation within the wear track and higher measured wear rates and friction coefficients.

Overall, although the effects of Si power applied to the target were less radical than the effect of bias applied at the substrate, some important discoveries were made, and the hardness of the coatings was increased by nearly an additional GPa. With increased power to the Si target, a decrease in residual stress and an increase in texturing were noticed. It is possible that this decrease in stress, along with increased texturing could signify the presence of low angle grain boundaries. It is likely that low angle grain boundaries would result in considerably less residual stress than high angle grain boundaries, and this could also contribute to the high levels of (200) texturing seen in the samples as power to the Si target is increased. In fact, HRTEM micrographs to be presented shortly in the final section of this chapter do in fact confirm the presence of low angle grain boundaries with possible amorphous content located between nanoscale

sub-domains within an overall columnar film structure. Thus, when the microstructure is adjusted such that subgrains of TiN and (TiSi)N present within the columnar structure of the film have both low angle grain boundaries and a thin amorphous layer surrounding these domains, hardness is enhanced.

5.4 Effect of Substrate Rotation

In the final phase of the TiSiN study, the effects of varying substrate rotation were explored. The 3" Si wafers were affixed to a 4" substrate holder with rotation capability. During TiSiN coating depositions discussed thus far in this chapter, the substrate was rotated at a rate of approximately 3 RPM. Rotation was performed to ensure uniformity of the coatings. Since both a DC plasma from a Ti target and an RF plasma from a Si target were used to deposit the TiSiN films, the portion of the plasma on the left hand side of the deposition chamber containing the Si target would tend to be rich in silicon ions, while the plasma towards the front of the chamber in the region containing the Ti target would tend to be rich in Ti ions. Therefore, a lack of rotation would result in a sample with a graded composition, with one side of the coating being more Ti rich, and the other having higher Si content. Therefore, the substrate was rotated to avoid this effect and to encourage the formation of a uniform coating. In the final series of TiSiN coatings to be presented in this chapter, the speed of the rotation of the substrate was adjusted in order to assess the impact of this variable on coating properties. TiSiN films were processed at conditions of 60 W power to the Si target, 100 V bias to the substrate, and 25% N_2 in the gas mixture. The rotation speeds used were 1 RPM, 3 RPM, and 6 RPM.

5.4.1 X-Ray Diffraction of TiSiN Substrate Rotation Series

Low angle X-Ray diffraction at 5° incidence angle was performed for the TiSiN coatings processed at substrate rotation speeds of 1 RPM, 3 RPM, and 6 RPM. As can

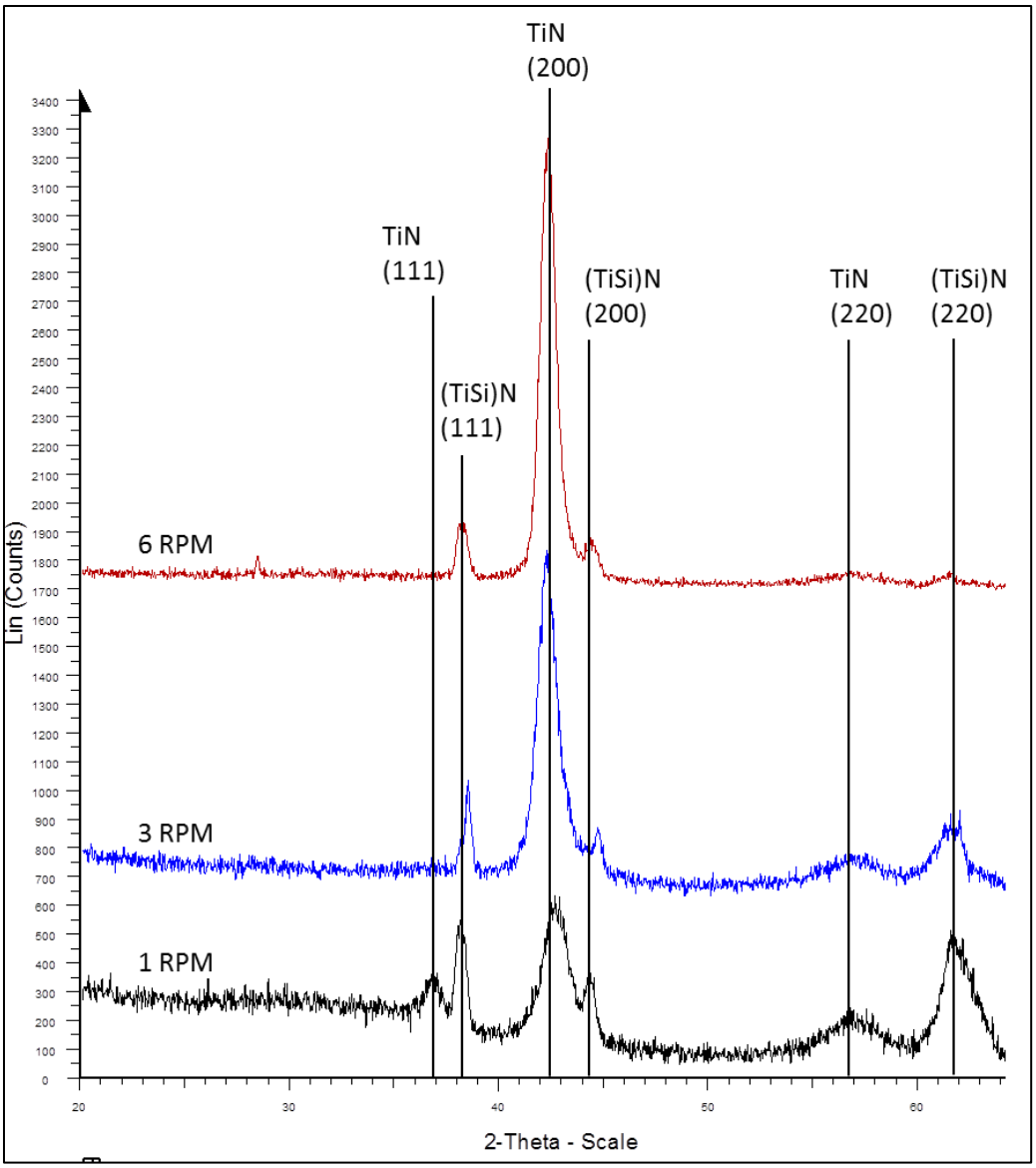

Figure 5-19 Low Angle XRD for TiSiN coatings produced at identical deposition conditions, with only substrate rotation varied

be seen in Figure 5-19 on page 92, the characteristics of each XRD scan are quite different, even though all deposition conditions besides the speed of substrate rotation were identical. With increasing substrate rotation, the coatings clearly shift from a more randomly oriented FCC TiN and FCC (TiSi)N structure to a more textured coating, with a

preferred (200) orientation in the coating deposited at 6 RPM. This indicates that a faster rotation speed results in a sample with a more textured crystal structure, while rotating the substrate more slowly allows for more randomly oriented, nanoscale crystalline regions to develop. Estimations on the grain size of the crystalline phases within the film showed virtually no change from film to film, with the prominent XRD peak for each film yielding a grain size estimate between 9 -11nm.

5.4.2 Effect of Substrate Rotation on the Mechanical Properties of TiSiN Coatings

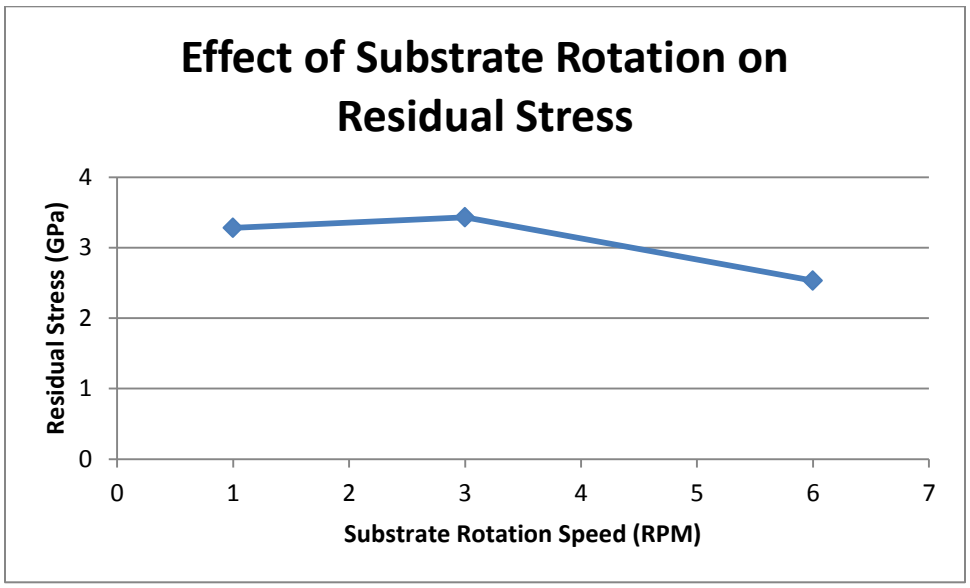

Figure 5-20 Residual stresses present within TiSiN coatings processed using different substrate rotation speeds, as estimated by Stoney's Equation

Similarly to the previous sections of this chapter, the residual stresses present in the as-deposited films were estimated, and the hardness and tribological properties were measured. The residual stress estimates show that the levels of stress within the 1 and 3 RPM samples are nearly identical, and the residual stresses are reduced in the sample which was deposited using the highest rotation speed, also displaying the most texturing and the highest hardness. Thus, a relationship between increasing (200) texturing,

increasing hardness, reduced prominence of the (TiSi)N FCC crystal structure, and reduced residual stress is established in each series of TiSiN coatings presented in this chapter, regardless of the specific experimental parameter (bias, power to Si target, or substrate rotation) varied. The estimated residual stress values can be seen in Figure 5-20 on page 93.

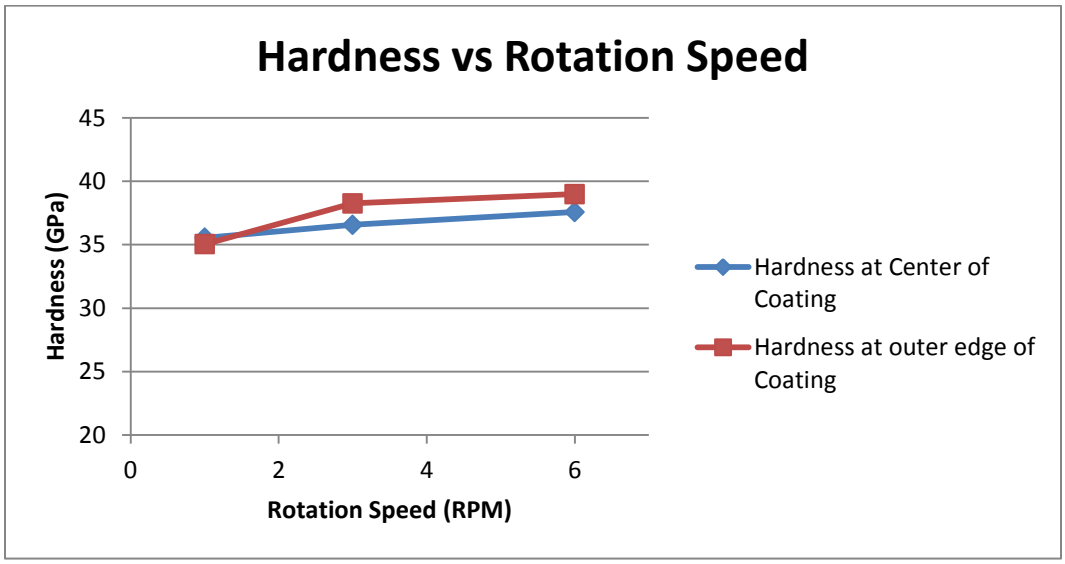

Figure 5-21 Effect of substrate rotation speed on coating hardness at both the center and the outer edge of each TiSiN coating

Hardness was measured using nano-indentation, Figure 5-21 on page 94. It was found that the TiSiN film with the highest rotation possessed the highest hardness of the three explored films. In fact, the TiSiN coating processed using the fastest rotation speed had the highest hardness of any of the TiSiN films produced in this study, with a hardness of 38.9 GPa. Additionally, the hardness was measured at both the center and the outer edge of each sample processed, since one would expect the hardness enhancement effects resulting from substrate rotation to vary radially from the center axis of rotation to the outer edge of the produced coating, farthest from the axis. It was found

that although there was some variation in the hardness, for the most part, the hardness of the coatings remained uniform between the center and edges of the coatings. As with the TiSiN coatings disussed in the previous sections of this chapter, the mechanism of deformation was assessed using the loading and unloading curves. In the case of varying substrate rotation speed between 1 RPM and 6 RPM, no significant change in the percentage of the unloading curve associated with elastic recovery was noted. All rotation values had an elastic recovery percentage between 59 and 62%, with no apparent trends in the data.

5.4.3 Tribological Testing of Varying Substrate Rotation TiSiN

Table 5-4 Trobilogical properties measured experimentally for varying rotation TiSiN series

Coating	Wear Track Radius (mm)	Wear Track depth (nm)	Wear Track width (um)	Wear Rate (mm^3/Nm)	Coefficient of friction, μ
1 RPM	21	126	221	1.1E-05	1.22
3 RPM	21	140	174	7.3E-06	1.03
6 RPM	21	129	197	1.1E-05	1.13

Once again, with high coating hardness, the experimentally measured wear rate and coefficients of friction were high for the TiSiN series with varying rotation speeds. As seen in Table 2-1, the friction coefficient is above 1.0 for each sample examined in this series, and the wear rates are all quite high, compared to most of the softer samples in the varying bias TiSiN series discussed earlier in this chapter. Once again, the presence of white (presumably alumina) debris within the wear tracks to the naked eye immediately after completion of the tribological wear experiments. It is thought that the high values for

coefficient of friction as well as the comparatively high wear rates may be related to the presence of this debris.

5.4.4 TEM and detailed Microstructure Study of TiSiN Varying Rotation Coatings

Cross sectional samples were studied of the B100 Si60 N25 3RPM and the B100 Si60 N25 6RPM coatings in order to assess the crystal structure using electron beam diffraction and the morphology using HRTEM. The overall goal was to gain an understanding of the film characteristics at the nanoscale which contribute to the excellent mechanical properties of the coatings, which exhibited hardness of nearly 40 GPa.

5.4.4.1 Electron Diffraction of TiSiN coatings with varying substrate rotation speed

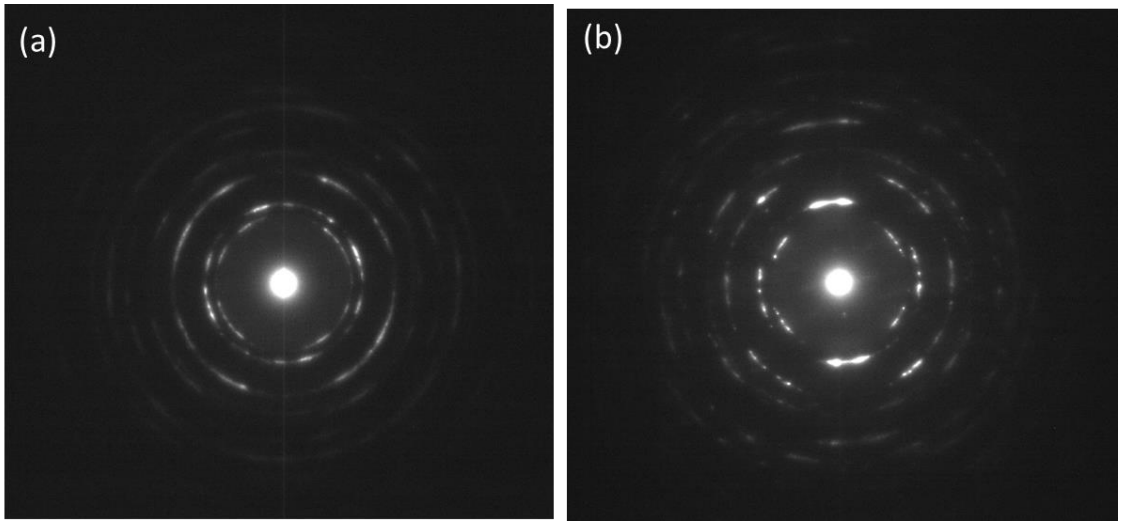

Figure 5-22 Electron Diffraction Patterns for TiSiN coatings processed with (1) 3 RPM and (b) 6 RPM rotation speed

Electron diffraction was performed for TEM samples created from the 3 RPM and the 6 RPM TiSiN films which exhibited hardness of 37.9 and 38.9 GPa, respectively. While XRD on these films showed the presence of TiN and (TiSi)N FCC crystalline

phases, electron diffraction was not able to distinguish the small variation between the two FCC phases, which varied in lattice parameter by only 3%. While no differences were found in the phases present between the two coatings of varying rotation speed, it is apparent by comparison of the two electron diffraction patterns in Figure 5-22 on page 96 that the coating processed using the higher rotation speed possesses a higher degree of texturing from the discontinuity of the diffraction rings. This result is in agreement with the previously discussed low angle XRD.

Table 5-5 Experimentally measured and indexed d-spacings from TEM electron diffraction patterns

	B100 Si60 N25 3RPM d spacing	B100 Si60 N25 6RPM d spacing
TiN (111)	2.44	2.42
TiN (200)	2.10	2.08
TiN (220)	1.49	1.47
TiN (222)	1.21	1.20
TiN (400)	1.06	1.04
TiN (420)	0.94	0.98

The lattice parameter of each film is a = 4.23 Å, and the experimentally measured d spacings from the diffraction rings are listed in Table 5-5 on page 97. While the difference is only very slight, the coating processed using the higher rotation speed possesses a slightly more compressed FCC crystal lattice. This could be inter-related to the decreased levels of residual stress present in the coatings with increasing rotation speed.

5.4.4.2 Columnar Morphology of TiSiN Coatings with varying substrate rotation speed

Figure 5-23 (a) on page 99 shows a bright field, low magnification image of a cross section of the thickness of the B100 Si60 N25 3RPM TiSiN film. Several distinct layers can be seen in this cross section. From the top, down, layers present include the Si substrate, SiO_2 layer, Ti adhesion layer (deposited for 4 minutes), TiSiN nucleation (interlayer), and the columnar TiSiN coating. Columnar structure is clearly present through the thickness of the coating, with some columns spanning the entire thickness of the coating, and others being as short as about 200 nm in height. While the columns are dense, crystalline, and encompass the entire coating, they also have a fine, feather-like structure. The width of the columns varies greatly, with some being as wide as about 60 nm, and others being only about 10 nm in width.

Figure 5-23 (b) on page 99 shows a similar view of the B100 Si60 N25 6RPM TiSiN coating. Again, a SiO_2 layer and Ti adhesion layer were identified using EDS, and a TiSiN nucleation/interlayer exists between the Ti adhesion layer and the TiSiN coating. While a columnar morphology is still clearly present in the coating with higher substrate rotation speed, the columns appear to be even finer in structure than those in the 3 RPM film. Once again, although the columnar structure spans the entire thickness of the film, many of the individual columns do not actually span the entire cross section of the film, with the majority being between 200-400 nm tall. Additionally, faster rotation appears to result in thinner, finer column structure. The majority of the columns within the film are between10-30 nm in width. It should be noted that as rotation speed increased, both residual stress and prominence of the crystalline (TiSi)N phase decreased, as seen from the low angle XRD. This not only reinforces the previously discussed relationship between residual stress and state of Si within the coatings, but the TEM micrographs also suggest the presence of a higher number of column boundaries within the coating with

increasing rotation speed, decreasing residual stress, and increasing hardness. This supports in general Veprek's suggestion of amorphous Si localized at crystalline boundaries, since the quantity and thus the overall volume percent of grain boundaries are increased in conjunction with a decrease in the presence of Si incorporation into the FCC TiN crystal structure.

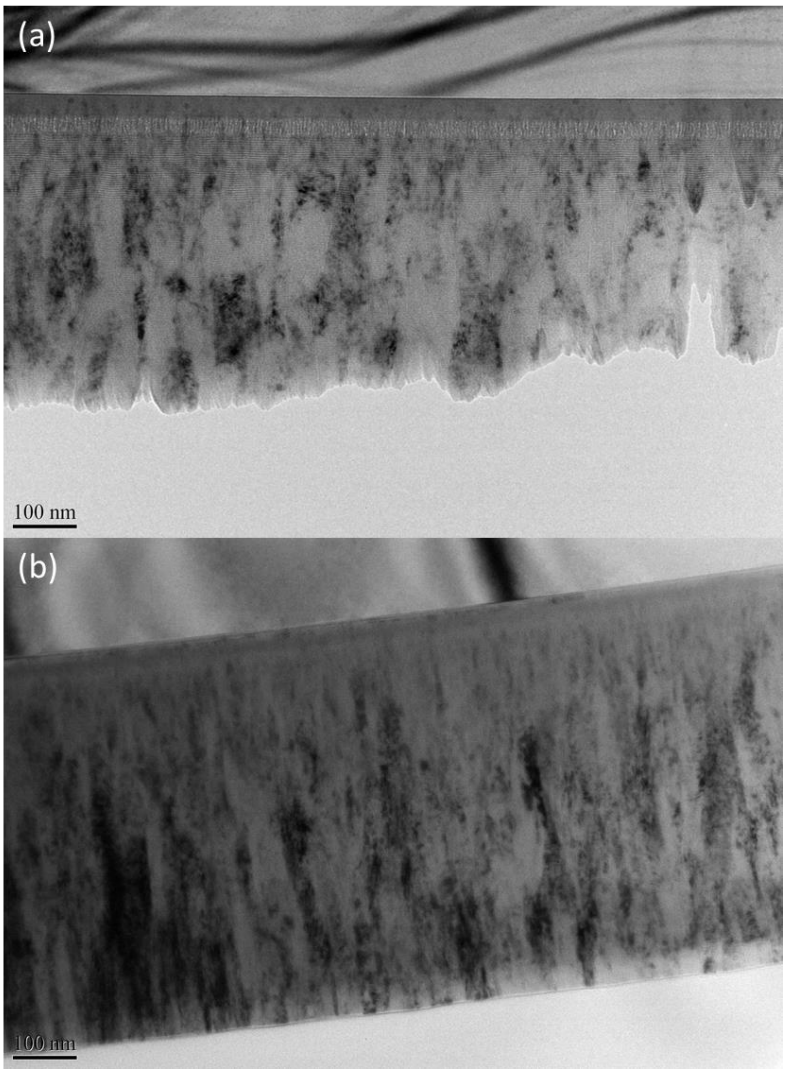

Figure 5-23 Low magnification, bright field images of (a) TiSiN 3 RPM and (b) TiSiN 6 RPM

Another clear difference in the morphology of the coatings produced at 3 RPM and 6 RPM rotation speeds is the occurrence of multilayers. In Figure 5-24 (a) on page 102 showing the 3 RPM coating, multilayers of about 2.5nm can be clearly seen. These multilayers span the entire thickness of the coating, and they are continuous even across column boundaries. With faster rotation speeds, however, these multilayers completely disappear. Figure 5-24 (b) on page 102, which was taken at the same magnification as Figure 5-24 (a), clearly shows no sign of the multilayer structure. These micrographs are representative of the overall microstructure in both cases.

From these micrographs, it is clear that rotation speed has a clear impact on the morphology of the deposited TiSiN coatings. As explained in detail in the experimental section of this report, two targets, Ti and Si, are used in the preparation of these coatings. The Ti target is placed in the front magnetron gun, and the Si target is placed in the left magnetron gun. While these magnetrons would both ideally be pointed exactly towards the center of the rotation substrate holder, experimental constraints result in the magnetrons each being pointed slightly outside of the axis of substrate rotation. This results in the plasma containing a Si rich region towards the left side of the chamber and a Ti rich region towards the front of the chamber. As the substrate rotates, it moves in and out of the Si and Ti rich regions. In the case of the lower rotation speed, this rotation through the Ti and Si rich plasma regions presumably causes the multilayer structure seen in Figure 5-24 (a) on page 102. In fact, when the deposition rate of approximately 400nm/hr and the rotation speed of 3 RPM are used to calculate the approximate amount of deposition per rotation of the substrate, the result is a thickness of 2.22 nm. This is in very close agreement with the thickness of the multilayers seen in Figure 5-24 (a). Thus,

a mutilayered structure is produced in the lower rotation speed coating as a result of increased time spent in the Ti rich and Si rich regions.

In the 6 RPM coating, although the substrate is rotated through the Si rich and the Ti rich regions in the same way, no multilayers are visible via TEM. With the faster rotation speed, the multilayers have less time to form, since any given area on the outer edge of the substrate spends only about ½ the amount of time in the Ti and Si rich regions of the plasma cone. Additionally, while the presence of the multilayers creates an obvious difference in the appearance of the nanoscale morphology, it does not appear to actually have significant effects on the hardness. The coating produced at 3 RPM had a hardness of 37.9 GPa, and the coating produced at 6 RPM had ha hardness of 38.9 GPa. While the higher rotation did increase the hardness of the film by 1 GPa, the film with the lower rotation speed still displays excellent hardness, and these two values of hardness are not statistically significant from one another. In addition, if the mechanical properties were significantly dependent on the rotation speed of the substrate, one would expect properties to vary radially from the center to the edge of the sample. From the data presented in Figure 5-21 on page 94, however, this is clearly not the case. Thus, it can be determined that the presence or absence of the multilayers does not significantly affect the mechanical properties of the coating materials, and excellent mechanical properties are possible with or without the presence of these layers.

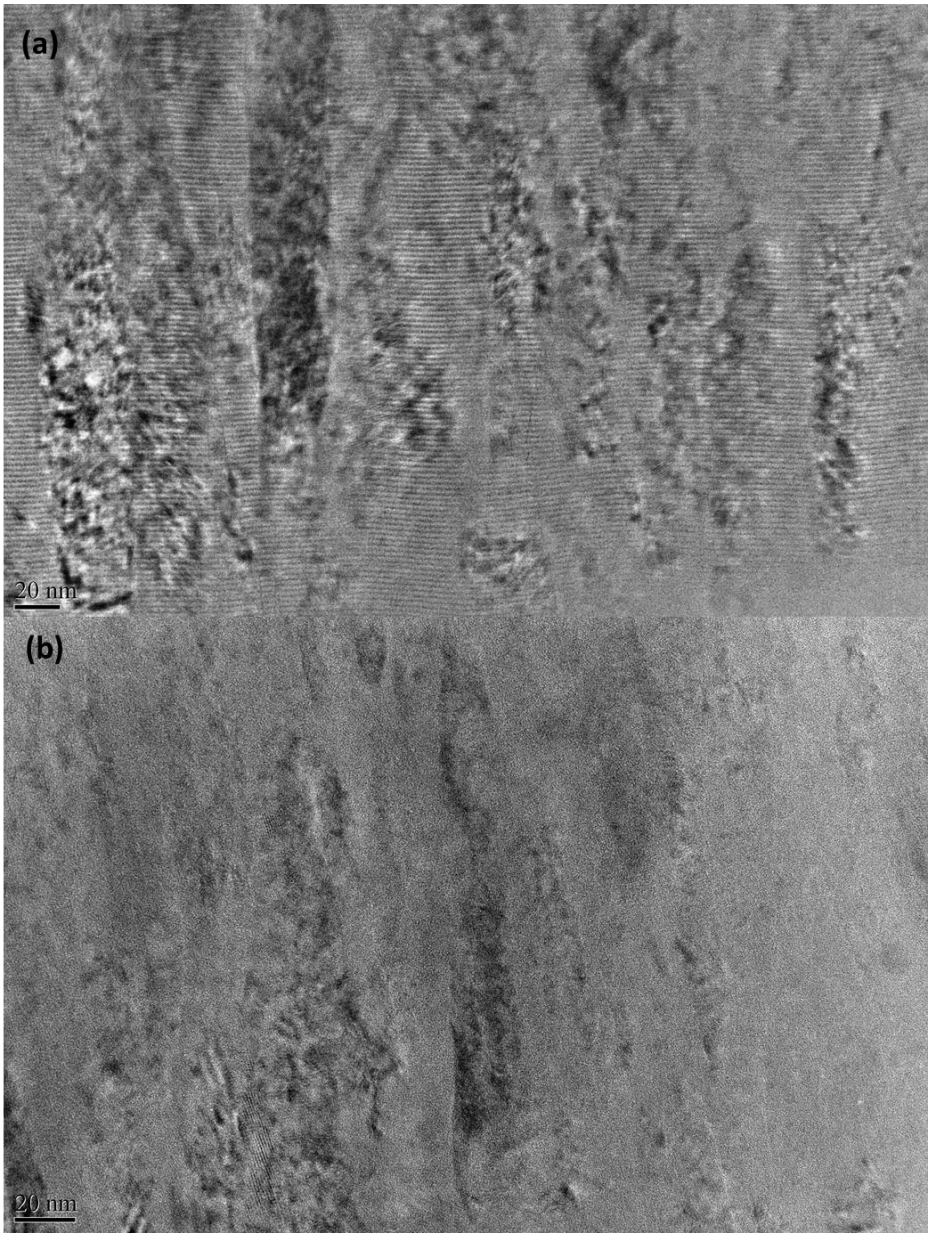

Figure 5-24 TEM micrographs of the columnar structure of (a) 3 RPM and (b) 6 RPM rotation speed TiSiN coatings

5.4.4.3 Sub-domain structure within TiSiN columns

Within the columns in both the 3 RPM and the 6 RPM TiSiN films, nanoscale subdomains or subgrains were present. Examples of these subgrains can be seen for the 3 RPM coating in Figure 5-25 (a) on page 104 and for the 6 RPM coating in Figure 5-25 (b). In the case of the low rotation coating, grain boundaries are not clearly defined, and individual subdomains can be identified by slight variations in the direction of lattice fringing. For the 6 RPM coating, however, bright grain boundaries surrounding two distinct nanoscale TiN grains of (200) orientation are visible. Both the 3 RPM and the 6 RPM sample show (200) orientation within the subgrains. No other orientations besides (200) were identified upon examination of the high resolution TEM micrographs.

When comparing the two high resolution micrographs presented in Figure 5-25, the most obvious difference is the presence of the multilayers in the 3 RPM coating, and their absence in the 6 RPM coating. Based on results from the previously studied Arc TiSiN samples, Figure 4-9 (c), this type of coating may have some compositional contrast, with Si rich material showing up as a brighter in comparison to Si-poor material. Since the smallest spot size for EDS measurements on the HRTEM is 10 nm, and since the difference in the distance in the lattice fringes is not measurable, there is unfortunately no clear way to confirm that the lighter regions contain more Si by atom % than the darker regions. However, based on the previously reported result, as well as critical reasoning based on the processing conditions used for film deposition, it is reasonable to hypothesize that the brighter regions within Figure 5-25 (a) and (b) contain higher amounts of Si than the darker regions. In the case of the lower rotation speed, when the substrate spends more time in the Ti and Si rich regions of the plasma, TiSiN layers with varying amounts of Ti or Si present within the FCC crystal lattice are allowed

sufficient time to form. Thus, the majority of the Si is likely located within the brighter portion of each multilayer.

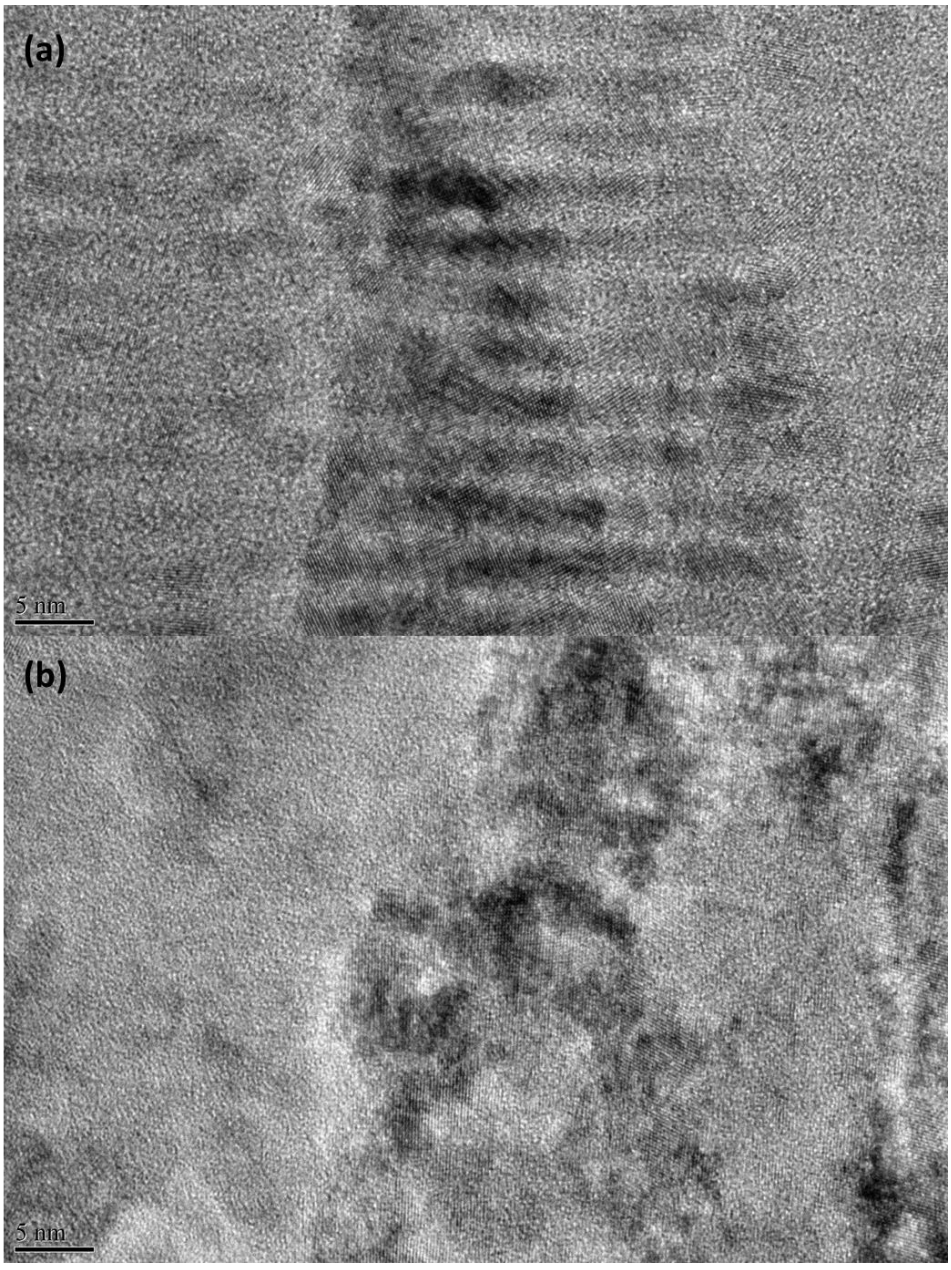

Figure 5-25 High resolution TEM micrographs of the microstructure of (a) 3 RPM and (b) 6 RPM TiSiN films

In the case of the higher rotation speed coating however, the time that the substrate spends in each region of the plasma is not sufficient for the formation of distinct layers of Ti-rich and Si-rich (TiSi)N material. Instead, a more uniform microstructure is formed, and more of the crystalline content in the coating is FCC TiN, as opposed to FCC TiSiN. This hypothesis is supported by the increase in intensity of the (200) TiN peak with increasing rotation speed, as measured by low angle XRD, Figure 5-19 on page 92. Several subgrains can be clearly distinguished in Figure 5-25 (b) on page 104. These subdomains, present throughout the film, are predominantly equi-axed, and they vary in size from approximately 10-30 nm in diameter. The distribution of the brighter regions in the higher rotation coating differs significantly from that of the lower rotation speed coating. In the case of the 6 RPM film, the bright regions appear to be localized around subgrains, rather than in layers, as seen in the 3 RPM sample. This is consistent with Veprek's prediction that the Silicon content may reside as amorphous content, localized at the grain boundaries of nano-scale TiN grains.

5.4.5 Summary of Effects of Varying Rotation Speed on TiSiN Coatings

Varying the rotation speed of the substrate during TiSiN deposition had small, but measurable effects on the properties of the as deposited coatings and had a great impact on the morphology of the coatings at the nano-scale. Increasing rotation speed had a clear effect on the low angle X-Ray diffraction results, with increasing rotation speed resulting in a more highly textured coating in the (200) direction. Additionally, the hardness of the coatings increased with increasing rotation speed, and the residual stress decreased. From these results, it seems probable that the multilayered structure which forms in the case of the lower rotation speed coatings contains layers rich in Ti which are likely consistent of predominantly TiN crystalline content and layers more rich in Si, where the crystalline (TiSi)N likely resides. This constant fluctuation could explain

the higher values for residual stress present in the coatings with lower rotation speeds, and is consistent with the tendency of the (TiSi)N phase to increase in prominence with decreasing substrate rotation speed.

Low magnification TEM showed the presence of columnar morphology in the coatings produced using the 3 RPM and the 6 RPM substrate rotation speeds. The columns were dense, and spanned the entire thickness of both films. Higher rotation, however, yielded a finer, more feather-like shape of the columns within the film. In the case of the TiSiN coating produced at 3 RPM, a clear multi-layer structure resulting from rotation through Ti and Si rich regions of the plasma within the deposition chamber was present. Each layer is approximately 2.5 nm in thickness and presumably consists of a Ti-rich and an Si-rich component. In the 6 RPM sample, however, these multiplayers are not present. This suggests that faster rotation through the Ti-rich and Si-rich portions of the plasma does not allow sufficient time for formation of clear layers, resulting in a coating with more uniform microstructure, and slightly improved mechanical properties.

High Resolution TEM showed signs of the nc-TiN a-Si_3N_4 microstructure, as proposed by Veprek. The presence of amorphous content at the grain boundaries was not innately clear, however, and most of the subgrains were only distinguishable by low angle grain boundaries, visible via slight changes in the angles of the lattice fringing. This was especially true for the coating processed using the lower substrate rotation speed. These subdomains could be seen in both the 3 RPM and the 6 RPM coatings, but they were much more easily distinguished via the appearance of grain boundaries in the coating processed using higher substrate rotation.

5.5 Discussion and Conclusions of PVD Magnetron Sputtered TiSiN Coatings

Three different series of TiSiN coating produced using the in-house SaNEL PVD Magnetron Sputtering system show the effect of various processing parameters on the

mechanical properties of the as-produced coatings. The coatings with the most desirable mechanical properties were then examined in great detail in order to determine the relationship between the microstructure and the observed mechanical properties of the coatings. Based on the analysis presented here, some interesting relationships between not only the processing conditions and the various mechanical properties, but also the interaction of the crystal structure, the hardness, and the residual stress emerged.

The effects of bias voltage on mechanical properties were assessed, and it was found that increasing bias led decreased hardness and increased presence of residual stress present within the coatings. In fact, the relationship between increased hardness, decreased residual stress, and decreased prominence of Si within the FCC crystal lattice was a recurring theme observed in all three series of TiSiN coatings explored in this chapter, regardless of the deposition parameter being investigated in each particular series. Increased bias voltage results in the presence of increased energy at the site of the substrate during coating deposition. This can in turn cause re-sputtering effects of atoms away from the coating after their initial deposition. Thus, coatings produced using high bias voltage may contain atomic arrangements which would not be energetically favorable under conditions with less bias applied. Much as the Arc deposited TiSiN coatings are suspected to contain Si content within the FCC TiN crystal lattice due to the high energy processing conditions, increased prominence of FCC (TiSi)N was observed as the energy was increased in the reactive PVD magnetron sputtering process.

Next, the power to the Si target was varied in order to determine the effects of varying Si on the properties of the coatings. It was found that decreasing the RF power applied to the Si target from 60 W to 50 W resulted in a slight decrease to the mechanical properties of the coatings, with decreased hardness and increased residual stress.

Additionally, increased Si content and increased hardness correlated with increased presence of texturing within the coatings, as observed with low angle XRD.

Variation in the rotation speed yielded an additional 1 GPa improvement in the hardness of the coatings, with the fastest rotation speed resulting in a coating with a hardness of 38.9 GPa. This coating showed high amounts of (200) texturing, relatively low residual stress within the film, and high amounts of elastic recovery present in the nanoindentation unloading curve. A detailed investigation of the morphology of the coating using HRTEM showed the presence of a highly refined nanoscale material. The film consisted of dense, but fine columns, only tens of nanometers in width. Within the columns, subdomains were clearly present. In some cases, bright grain boundaries were visible immediately adjacent to the (200) oriented TiN crystals. Previous results suggest a degree of compositional contrast, with brighter regions being richer in Si content than darker regions. This supports Veprek's proposed nanostructure of possible accumulation of amorphous silicon nitrides around the grain boundaries of the TiN nanoscale grains.

Veprek's proposed model of a nc-TiN/a-Si_3N_4 system achieved via spinodal decomposition was largely based on work with CVD systems, and little concrete proof of the formation of this microstructure according to this phenomenon exists in the literature, to date. [12, 13, 21-23, 27, 48, 52, 79, 89, 94] In the case of the less energetic coating processing involving the presence of chemical species for Si deposition such as CVD, crystalline MeN and amorphous silicon nitride are consistently reported. However, it seems clear based on upon a both critical review of the literature and on the results presented in this work, that a high energetic presence during coating deposition adds a degree of complexity. Although the resulting PVD TiSiN coatings still have extraordinary mechanical properties, their microstructure cannot be completely explained by Veprek's model.

MeSiN coatings processed using PVD often have additional phases present, in addition to nanocrystalline TiN and amorphous silicon nitride. In fact, the (TiSi)N phase reported in this work has also been previously identified in the literature in coatings processed via PVD methods. [59] In the Arc TiSiN coatings explored in this work, the presence of a prominent (TiSi)N FCC phase where Ti substitutes for Si within the crystal lattice was identified. In addition, it was shown in the magnetron sputtered TiSiN films that increasing the bias voltage at the substrate resulted in increasing incorporation of Si into the TiN crystal lattice, thus increasing the prominence of the FCC (TiSi)N phase as the energy presence at the substrate during deposition increased. In addition, this work also showed a consistent increase in the residual stress present in TiSiN coatings with the increase in prominence of the (TiSi)N crystal structure. This suggests that a more detailed, complicated relationship exists between the relationship between deposition conditions and morphology at the nano-scale in the case of high energy processes such as PVD.

From this study, it was noticed in the case of each series studied that more highly textured films had higher mechanical properties in terms of increased hardness and decreased residual stress. In addition, FCC TiN and FCC (TiSi)N were present in the coatings in varying degrees of prominence. Although the relationships between processing conditions and incorporation of Si into the TiN crystal lattice was not immediately clear, closer inspection resulted in an understanding that residual stress, hardness, film texturing, and the appearance and fluctuating amounts of crystalline (TiSi)N within the coating are all likely inter-related. While some possible evidence was seen to support the presence of spinodal decomposition of the nc-TiN and the a-Si_3N_4 phases, as proposed by Veprek, it appears that the incorporation of Si and it's role in the microstructure may involve a much more than just the thermal requirements of at least

550˚C of substrate heating to reach the chemical spinodal. Instead, parameters like energetic presence at the surface of the coating during deposition, as well as residual stresses and tendency of textured grain formation, all play a role in the tendency for Si to localize within the crystalline structure versus at the grain boundaries in PVD processes.

TEM showed the presence of fine, nanoscale columnar structure with equi-axed nanoscale subdomains present within the columns. Although the presence of Si_3N_4 at the grain boundaries could not be confirmed via TEM, the presence of bright areas surrounding many of the grains, along with high resolution XPS and earlier evidence of compositional contrast, could indicate the presence of amorphous silicon content immediately surrounding the TiN nanoscale domains, thus contributing to the impressive mechanical properties of these films.

Chapter 6

PVD Magnetron Sputtered Tantalum Silicon Nitride Coatings

6.1 Introduction

While the TiSiN system has been explored in some amount of detail by researchers for the past 10-15 years, other less understood coatings are of significant interest for their abilities to perform as high hardness, high temperature coatings. One such system involving another transition metal is the TaSiN system. While TiSiN is typically a coating composed of mostly nanocrystalline components with some amorphous content, TaSiN coatings reported thus far in the literature tend to be mostly amorphous, with some having a small amount of crystalline content. Several studies report mechanical properties of the TaN system with no Si presence within the coatings. Although some researchers report the theoretical hardness of various crystalline phases of TaN such as FCC, 1:1 stoichiometric hexagonal, and orthogonal at values between 40 and 50 GPa, the experimental hardness values reported in the literature for FCC TaN are typically between 20-25 GPa. This is comparable to the hardness typically achieved in TiN coatings. Researchers able to achieve the hexagonal and orthogonal phases report higher hardness, between 32-39 GPa. [70, 71, 95]

TiSiN coatings are explored mainly due to their high hardness and utility as tribological coatings. While TiSiN has higher resistance to oxidation than TiN, it does not show great promise as a high hardness material, with oxidation of the film typically occurring near 600-650˚C. Conversely, TaSiN coatings with high Si and primarily amorphous content have been reported to resist oxidation to temperatures of up to 1300˚C. These amorphous coatings have been explored mainly because of promising optical and electrical properties and for use as insulating layers. Leading researchers in the field, however, have identified the TaSiN system as a promising possibility for the

further advancement of the knowledge and application of high temperature, oxidation resistant MeSiN coatings.

By applying the relationships and trends established and studied with the PVD magnetron sputtered TiSiN samples at SaNEL, initial TaSiN films which could serve as effective high hardness, oxidative resistant coatings were developed using the same, home-built sputtering system. Conditions used to create TiSiN coatings with high hardness were used in the deposition of TaSiN films. Upon analysis of the coatings, deposition conditions were altered in order to adjust the chemical content of the coatings, as needed. Three films processed with varying DC power to the magnetron gun containing the Ta target will be discussed in detail in this chapter.

The as-deposited TaSiN films were studied in order to determine the crystalline phases present and the grain size using low angle X-Ray diffraction. Nanoindentation was used in order to assess the hardness of the coatings, and the optical profilometer was used in order to measure the curvature and estimate the residual stresses present in the coatings.

In order to test the high temperature properties of the TaSiN coatings, the TaSiN films on Si substrate were annealed in ambient air at 550˚C. While this treatment resulted in severe oxidation, hardness decrease, discoloration, and overall breakdown of the TiSiN coatings, the TaSiN coatings remained in-tact. In fact, the coatings produced using the lower DC power s (70 W and 100 W) to the magnetron gun containing the Ta target showed almost no decrease in mechanical properties after annealing. No changes to the crystalline phases present within the coatings were observed via XRD scans performed before and after the annealing.

TEM and HRTEM were performed on the TaSiN samples produced using the intermediate power to the Ta gun, since this condition resulted in coatings which had

reasonably high hardness, which was maintained after annealing in ambient air, signifying that this material displayed good resistance to oxidation.

In addition, further studies on the TaN and TaSiN system are ongoing in the Surface and Nano Engineering Laboratory. The goal of the continued research is the development of a more thorough understanding of the relationships between processing conditions, material morphology, and mechanical properties in this promising system, resulting in further refinement of the coatings. Table 6-1 on page 114 lists the deposition conditions used in the processing of the TaSiN coatings used in this portion of the study.

Table 6-1 Processing conditions and results for TaSiN coatings deposited using reactive magnetron sputtering PVD

	Substrate			Ta Target			Si Target			Volumetric Flow		Deposition Rate (nm/hr)	Hardness (GPa)	E (GPa)
Coating Name	Power (W)	Voltage (V)	Current (mA)	Power (W)	Voltage (V)	Current (mA)	Power (W)	Voltage (V)	Current (mA)	Ar (sccm)	N2 (sccm)			
70WTa	2	100	20	70	329	245	60	264	227	18.75	6.25	450	20.7	233.1
100WTa	3.1	100	31	100	343	328	60	267	229	18.75	6.25	850	24.6	258.9
150WTa	4	100	40	150	359	456	60	272	221	18.75	6.25	1000	26.1	259.4
50WTa 30WSi 5%N2	1.7	100	17	50	272	215	30	169	178	23.75	1.25		33.5	256.1

6.2 X-Ray Diffraction of TaSiN Coatings

Low angle XRD with an incidence angle of 5˚ was used in order to determine the crystal phases present in the TaSiN samples processed using varying power to the Magnetron gun containing the Ta target before and after annealing in ambient air at 550˚C for 30 minutes. In addition, the Scherrer formula was used to estimate the grain size of the crystalline phases present within the films. Low angle X-Ray diffraction patterns can be seen in Figure 6-1 on page 116 with FCC TaN and (TaSi)N identified. In the 70 W and 100 W Ta coatings, FCC TaN with a lattice parameter of 4.34 Å was identified.

In addition an FCC (TaSi)N phase in which Si replaces some of the Ta atoms within the FCC structure with a lattice constant of 4.06 Å was found in the coatings produced using the 70 W and 100 W to the Ta target. The lattice parameter of the FCC (TaSi)N phase is 6.5% smaller than the lattice parameter of the FCC TaN phase. This result is not dissimilar to that found in the TiSiN system. When comparing the coatings processed using 70 W and 100 W of DC power to the Ta target, with Si power held constant, one might expect that the condition with increased presence of Si within the plasma would result in the increased presence of Si within the crystal lattice. However, the opposite is in fact true, and this result can be connected back to the TiSiN results presented in the two previous chapters, since an overall increase in the energy of the deposition process (increasing Ta power from 70 W to 100 W) resulted in increased prominence of Si within the crystalline portion of the microstructure, as identified by Low Angle XRD. This trend did not continue to the coating processed with 150 W DC power to the Ta target, likely because the deposition rate of Ta was sufficiently high as to overwhelm the Si content in the structure. The breadth of the peaks and the slight left shift in the TaN (111) peak for the TaSiN sample deposited using the highest power to

the Ta target likely contain grains with stoichiometry varying slightly from the usual (111). This phenomena has been previously reported in the literature in cases where the composition varies from 1:1 stoichiometric TaN. [95]

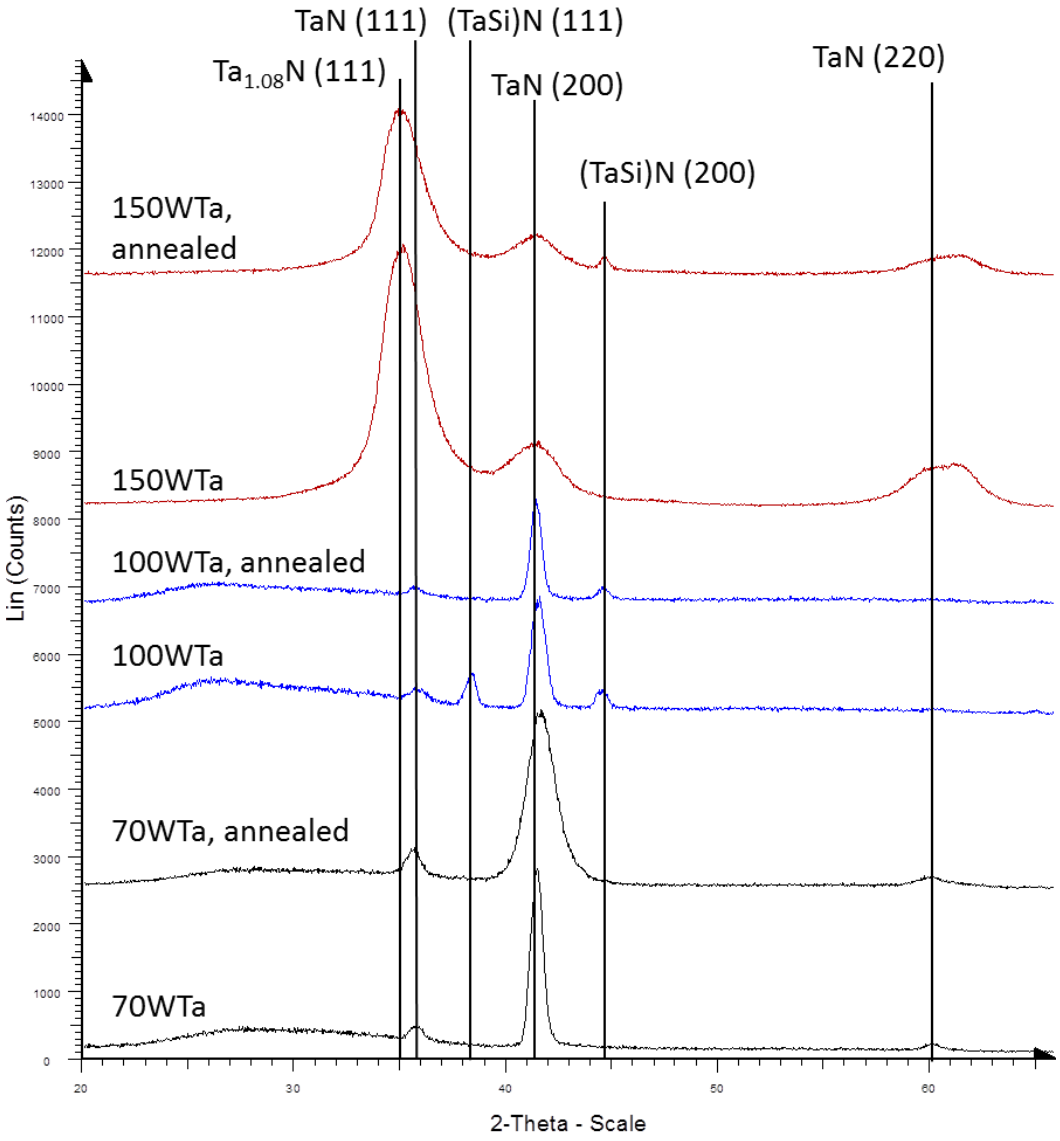

Figure 6-1 Low Angle XRD of TaSiN coatings processed with varying power to the Ta target, before and after annealing in ambient air at 550˚C for 30 minutes

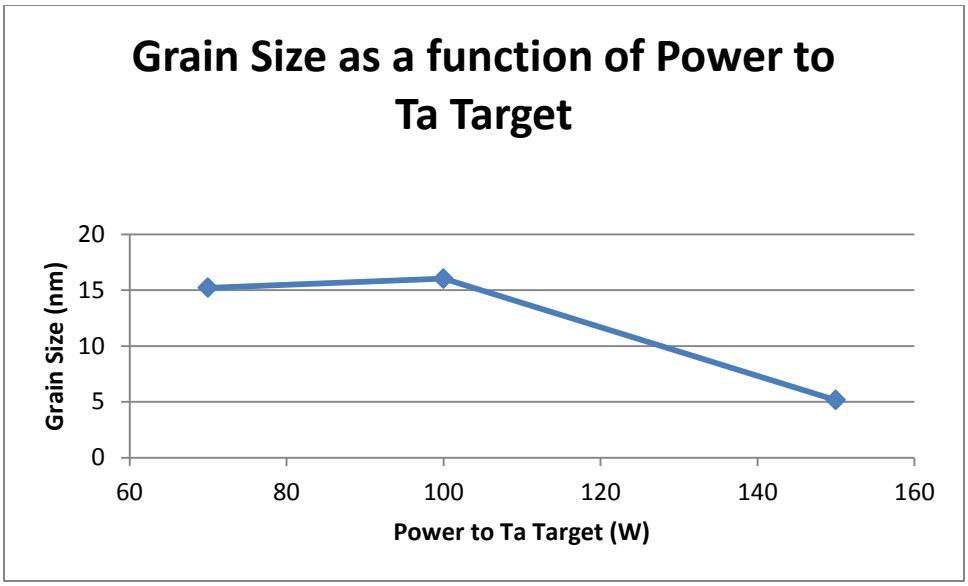

Figure 6-2 Grain size as a function of DC power to the Ta target, estimated using the Scherrer Equation

Additionally, amorphous content is identified in the regions between 22-34˚ on the XRD scans, but only in the 70 W Ta and 100 W Ta coatings. This feature is present both before and after annealing. Overall, the XRD scans before and after annealing show very little difference. The film processed using 70 W of DC power to the Ta target experienced some broadening of the TaN (200) peak after annealing. In the case of the film created with 100 W of power to the Ta target, the coating gained more (200) texturing after annealing. After annealing, the TaN (111) peak reduced in prominence, and the (TaSi)N peak went away entirely. The coating processed using 150 W to the Ta target measured nearly identically before and after annealing with low angle XRD. However, an overall intensity decrease of the FCC TaN peaks was observed, even though the scans were performed under identical conditions. This suggests the possibly formation of a thick, X-Ray amorphous oxide layer at the surface of the coating.

These XRD scans were also used, along with the Scherrer Equation, to estimate grain size. The estimated grain size as a function of power to the Ta target is presented in Figure 6-2, page 117. It is seen that while the films produced with 70 W and 100 W of power to the Ta target have very similar grain size, the film with the highest power to the Ta target had an estimated grain size of only 5 nm, only about 1/3 of the estimated grain size of the other two films. This nanoscale grain size is closely aligned with the grain sizes reported in both the Arc and the magnetron sputtered coatings discussed in Chapters 4 and 5, previously.

6.3 Chemical Composition of TaSiN Coatings

XPS was used to analyze the chemical content and bonds present within the as-deposited TaSiN films. Survey scans of the coatings processed using 70 W, 100 W, and 150 W DC power to the Ta target were performed in order to assess the atomic percent of Ta, Si, and N present near the surface of the coatings. The results of these scans can be seen in Figure 6-3 on page 119. As expected, an increase in Tantalum atom percent occurs as power to the Ta target is increased. In addition, Si and N content are reduced as with increasing power to the Ta target. It can be seen that the coating with the highest hardness had Si content very near to the amount which is proposed as necessary for the formation of the nc-MeN/a-Si_3N_4 microstructure, as proposed by Veprek. The Nitrogen content in this film, however, is too low to allow for the formation of both TaN and Si_3N_4 phases, reinforcing the notion of the presence of a sub-stoichiometric TaN phase consisting of excess Ta within the FCC crystal lattice.

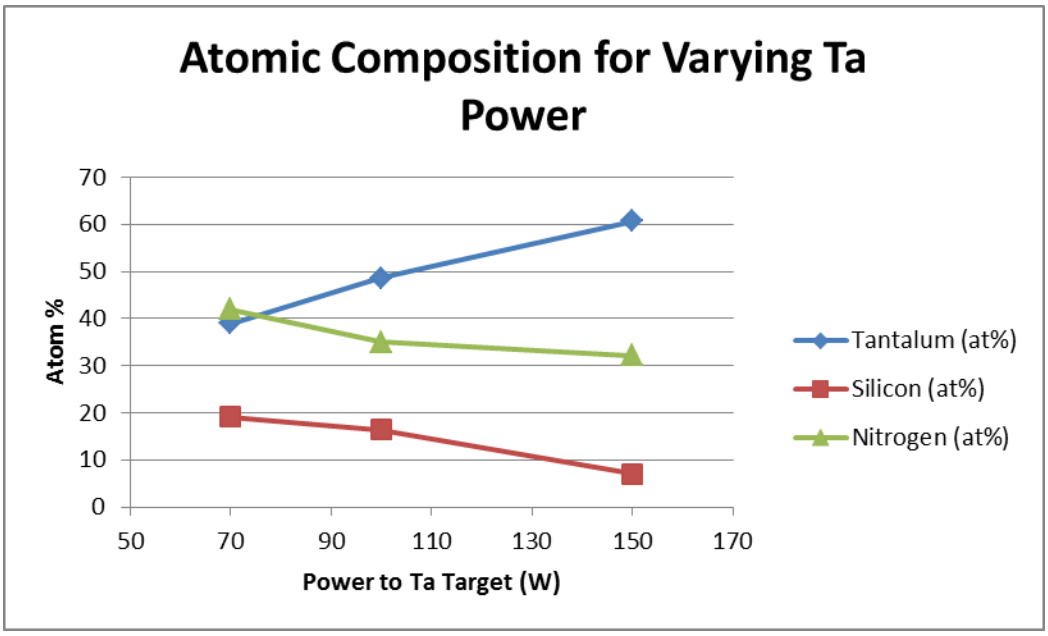

Figure 6-3 Atomic composition in terms of Ta, N, and Si (atom%) as measured by XPS survey scans

High resolution XPS scans of the Ta4s peak showed the presence of both Ta-N and Ta-Si doublets present. The peaks of the TaN doublet were found at binding energies of 27.8 and 25.7 eV, and the peaks for the TaSi doublet were found at 26.2 and 23.8 eV, respectively. No sign of Ta-O bonding was observable, indicating very low levels of oxygen impurities within the coating materials, Figure 6-4 on page 120.

6.4 Mechanical Properties of TaSiN Coatings

After processing the TaSiN coatings, the mechanical properties including the hardness and the residual stress were estimated. Because the TaSiN system is of great interest as a high temperature coating, the mechanical properties were assessed before and after ambient air annealing at a temperature of 550˚C.

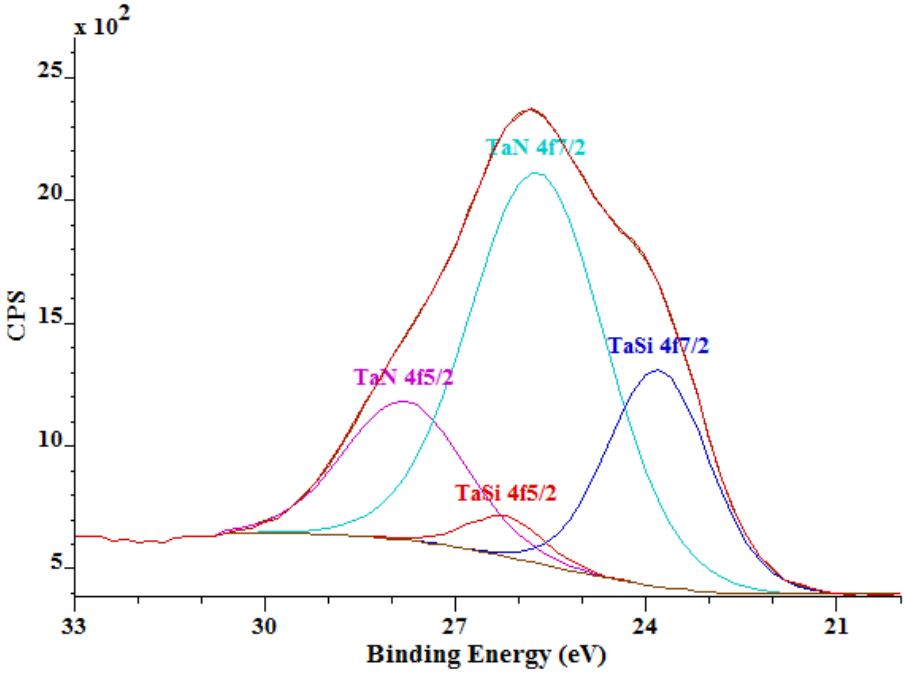

Figure 6-4 High resolution XPS of Ta4s peak from 100 W Ta coating, showing the presence of TaN and TaSi bonding

6.4.1 Hardness of TaSiN Coatings

From the blue data series in Figure 6-5 on page 121, the hardness of the as-deposited TaSiN samples can be seen. With increasing power to the Ta target, hardness of the resulting coatings increased, with all other deposition conditions being held constant. These deposition conditions were selected based on the large amount of knowledge from experimental data gained regarding the relationship between processing parameters and mechanical properties on the TiSiN system. The red data series in Figure 6-5 on page 121 shows the hardness after annealing for 30 min at 550˚C in ambient air. While the TaSiN coating processed using 150 W of DC power to the Ta target had the highest hardness, according to nano-indentation, it fared the worst in terms

of hardness after annealing in air. This is likely due to excessive oxidation. XRD of the films before and after oxidation showed no significant differences, except for a reduced intensity of all peaks, with little change in the ratios of the intensities of the peaks. This suggests the formation of an amorphous oxide layer at the surface of the TaSiN coatings. This oxide layer must be quite thin in the case of the 70 W Ta and 100 W Ta films, since the impact on the hardness of the films as compared to the hardness of the as deposited films is quite low.

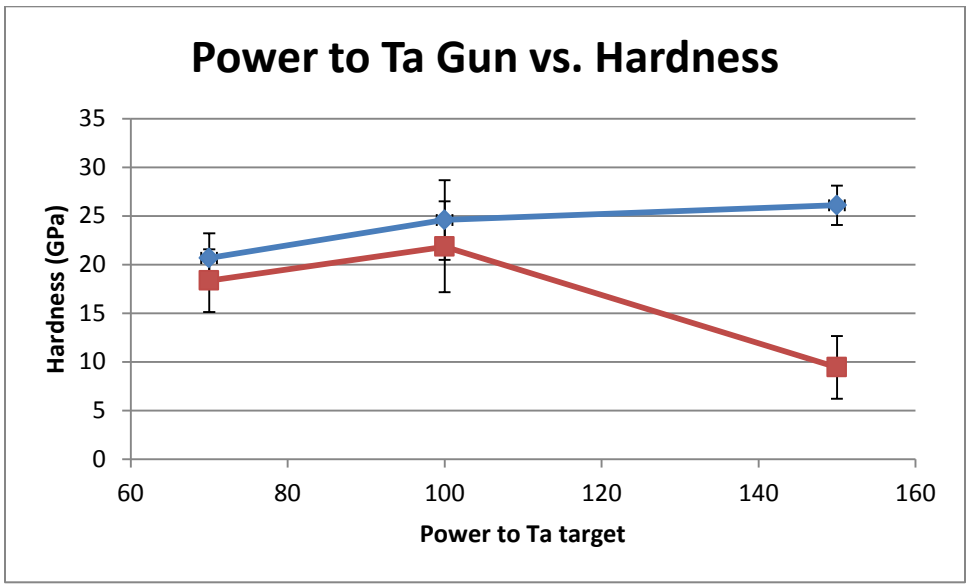

Figure 6-5 Hardness as a function of power applied to the Ta target during coatings deposition, before (blue) and after (red) annealing at 550˚C

In fact, TEM micrographs to be presented shortly confirm that the thickness of the oxide layer on the film produced using 100 W DC power on the Ta target was only about 20 nm. It should also be noted that similar experments were performed to deposit TaN coatings with no Si content. A TaN coating produced as identical conditions as the 100 W TaSiN coating, but with no power applied to the Si target, showed a hardness of

21.5 GPa. So, the addition of Si provides approximately 3.5 GPa of hardness enhancement over TaN under these specific deposition conditions.

The mechanisms of deformation were explored via examination of the TaSiN loading and unloading curves from nanoindentation. As compared to the TiSiN coatings, the TaSiN coatings were much less elastic. In fact, the coating produced with 70 W to the Ta target showed the greatest amount of elastic deformation, but this value was only 37%. Elastic deformation for the 100 W and 150 W coatings was approximately 33% in both cases. Compared to the values of above 50% elastic deformation obtained from nanoindentation of the TiSiN coatings, the values for elastic deformation of TaSiN are quite low. This indicates that a much higher percentage of deformation in the TaSiN coatings is due to irreversible, plastic mechanisms as compared to the TiSiN coatings.

The low difference in hardness values between the as-deposited and annealed 70 W and 100 W TaSiN films suggests the presence of a thin, soft oxide layer in both cases. Hardness indentations were taken at depths ranging from 50-70 nm, depending on the total film thickness. From the hardness data presented above, it is logical to assume that the cube corner tip must penetrate through the oxide layer and reach the largely unaffected TaSiN coating relatively quickly. Thus, the oxide layer must be no more than a few tens of nanometers in thickness. X-Ray diffraction scans previously presented also support this hypothesis, since there is very little difference in intensity of the FCC TaN peaks before and after annealing in the case of the 70 W and the 100 W films. TEM micrographs further supporting the presence of a thin, possibly amorphous oxide layer will be discussed shortly.

6.4.2 Residual Stress of TaSiN Films

Residual stresses were calculated before and after annealing in air at 550˚C. It can be seen that with increasing power to the Ta target, residual stress present in the

films was increased, reaching very high levels of nearly 5 GPa. In certain cases, the substrates even fractured during deposition, presumably due the high amounts of residual stresses present in these coatings, as well as their high thickness. As the power to the Ta target was decreased, however, the residual stresses decreased dramatically. This could be due to the incorporation of a significant amorphous content and increased (200) texturing with decreasing power to the Ta target, as seen in the XRD scans shown in Figure 6-1 on page 116. Residual stresses remained present after annealing, but the heat treatment in air appeared to result in significant relaxation of the stresses present within the coatings, Figure 6-6 on page 123.

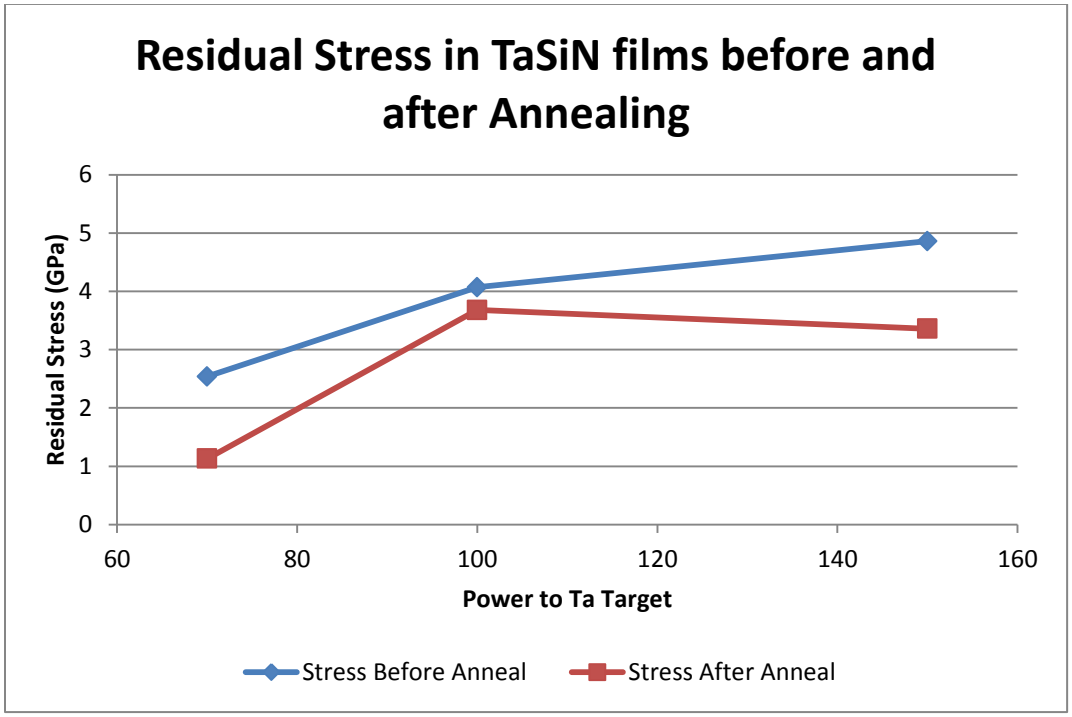

Figure 6-6 Residual stresses in TaSiN coatings before and after annealing

6.5 Microstructure of TaSiN Coatings, as explored by HRTEM

High resolution TEM was performed on the TaSiN coating processed using 100 W of DC power to the Ta target. Two TEM samples were examined, one each from before and after oxidation at 550˚C in ambient air for 30 minutes, in order to assess the effects of oxidation on the microstructure of the coating material. The sample processed using 100 W power to the Ta target was selected because it provided an intermediate hardness, near to the maximum hardness obtained, but it still displayed resistance to oxidation at 550˚C in ambient air, as previously shown in the XRD and nanoindentation data. Electron diffraction provided information regarding the crystal phases present in this coating before and after annealing, and TEM micrographs provided information regarding the film morphology and oxidation mechanism of the TaSiN material.

6.5.1 Electron Diffraction of TaSiN coatings

Electron diffraction of TaSiN coatings before and after annealing showed FCC TaN crystal structure. Little, if any, amorphous content was observed in these diffraction patterns, although some amorphous content appeared to be present based on the XRD scans discussed previously. Figure 6-0-7 on page 125 shows the electron diffraction for TaSiN before and after annealing at 550˚C in ambient air for 30 minutes. Both of these coatings have diffraction patterns with discontinuous rings. By comparison, the TiSiN coatings had diffraction rings, for the most part. Since these diffraction patterns were taken using the same size aperture as was used for the TiSiN coatings, this suggests the presence of larger crystalline domains within the TaSiN sample than were present in TiSiN. Additionally, there appears to be some (200) texturing in both the annealed and the unannealed TaSiN coating.

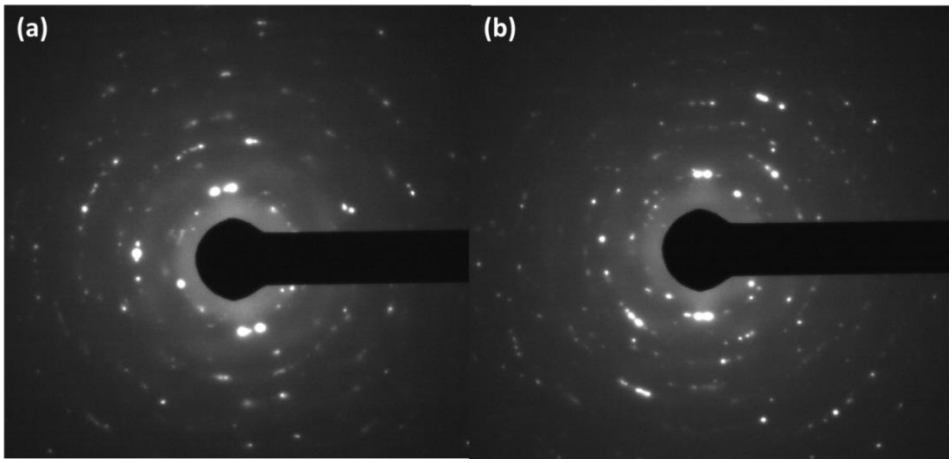

Figure 6-0-7 Electron diffraction patterns of (a) unannealed and (b) annealed TaSiN coatings processed with 100W DC power on Ta target

Table 6-2 lists the FCC crystal orientations present in the TaSiN coatings. No differences were noticed between the orientations present before and after annealing. No other phases other than FCC TaN were identified. Lattice parameters calculated from the measured diffraction rings were 4.33 Å and 4.36 Å for the as deposited and the annealed TaSiN samples, respectively.

Table 6-2 TaN crystalline phases present in as deposited and annealed TaSiN samples processed using 100 W power to Ta target before and after annealing

FCC Orientation	TaSiN as deposited	TaSiN, Annealed
TaN (111)	2.50	2.51
TaN (200)	2.16	2.18
TaN (220)	1.53	1.53
TaN (311)	1.31	1.30
TaN (420)	0.98	1.02
TaN (422)	0.87	0.88

6.5.2 Columnar morphology of TaSiN Coatings

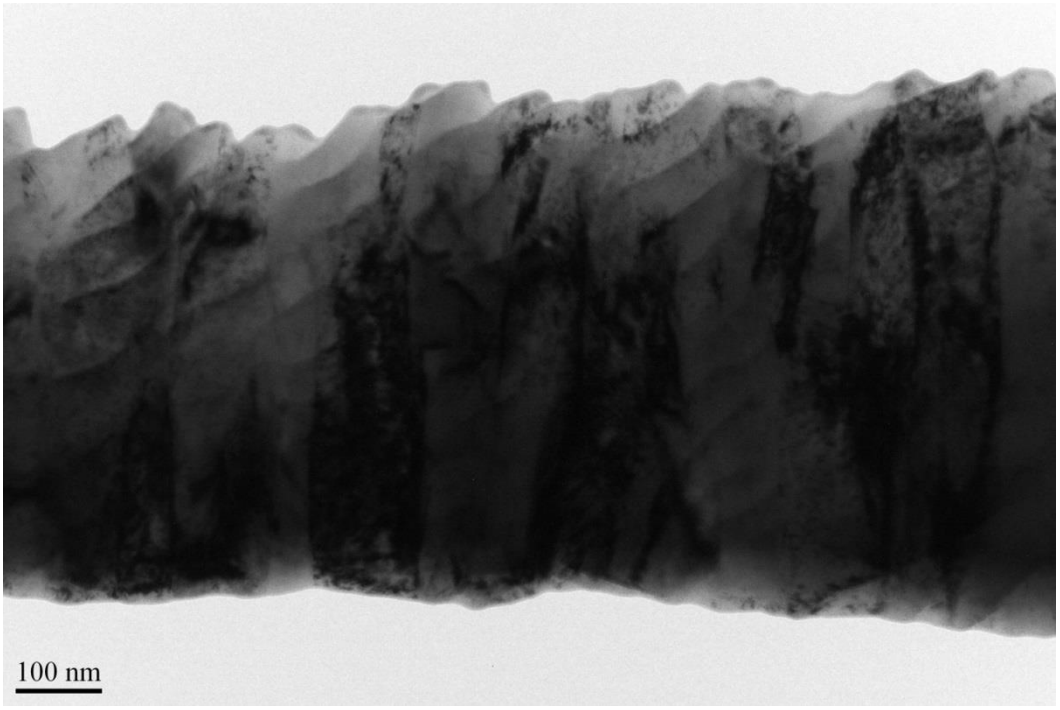

Figure 6-8 Low magnification TEM micrograph showing columnar morphology present in Ta 100 W coating

Low magnification TEM images showed a columnar morphology present in the TaSiN film before annealing, seen in Figure 6-8 on page 126. The columns were very dense, and were much thicker and more uniform in shape than the columns seen in the TiSiN coatings. Based on careful examination of the TEM foil, the columns appeared to be composed of entirely crystalline content. In the case of this TEM sample, the ion milling process preferentially removed the substrate, leaving a “flap” of TaSiN film material thin enough to be penetrated by the electron beam. The ridge like features, slightly slanted from the horizontal in this micrograph, are not thought to be features associated with the microstructure of the film itself. Rather, it seems likely that these features resulted from the bending of the TEM foil due to the previously discussed high

levels of residual stress present in the coating material. There was no change in the appearance or size of the columns in the TEM samples created from the unannealed and the annealed TaSiN films.

The columnar microstructure is highly common in PVD sputtering methods, and is often preferentially formed. When comparing the TaSiN to the TiSiN microstructure, a difference in both the width and the structure of the crystalline columns are obvious. In fact, it seems likely that a portion of the hardness enhancement and excellent mechanical properties displayed by the previously discussed magnetron sputtered TiSiN coatings could be due to the highly refined, feather-like, dense crystalline columnar structure. However, the morphology at the nanoscale also plays a key role in enhancement of mechanical properties of the coatings.

6.5.2.1 Oxidation Resistance of TaSiN Coatings

A clear oxidation layer was present at the surface of the TaSiN coating which was annealed in ambient air for 30 minutes at 550˚C. However, it was very difficult to obtain clear TEM micrographs of this layer. The layer was very thin in comparison to the thickness of the coating. While the coating was over 1 µm thick, the thickness of the oxide layer was only about 20 nm. This made thinning of the oxide layer via ion milling nearly impossible. Ion milling removed the majority of the oxide layer, instead of thinning it and making it thin enough for the electron beam to penetrate. However, some low magnification TEM micrographs were obtained demonstrating the thickness and the basic morphology of the layer, Figure 6-9 on page 128. EDS was not possible within the oxide layer, because the thickness was too high, so the composition cannot be determined with certainty. However, no additional crystalline peaks were visible using low angle XRD, signifying that the layer is likely amorphous, rather than crystalline.

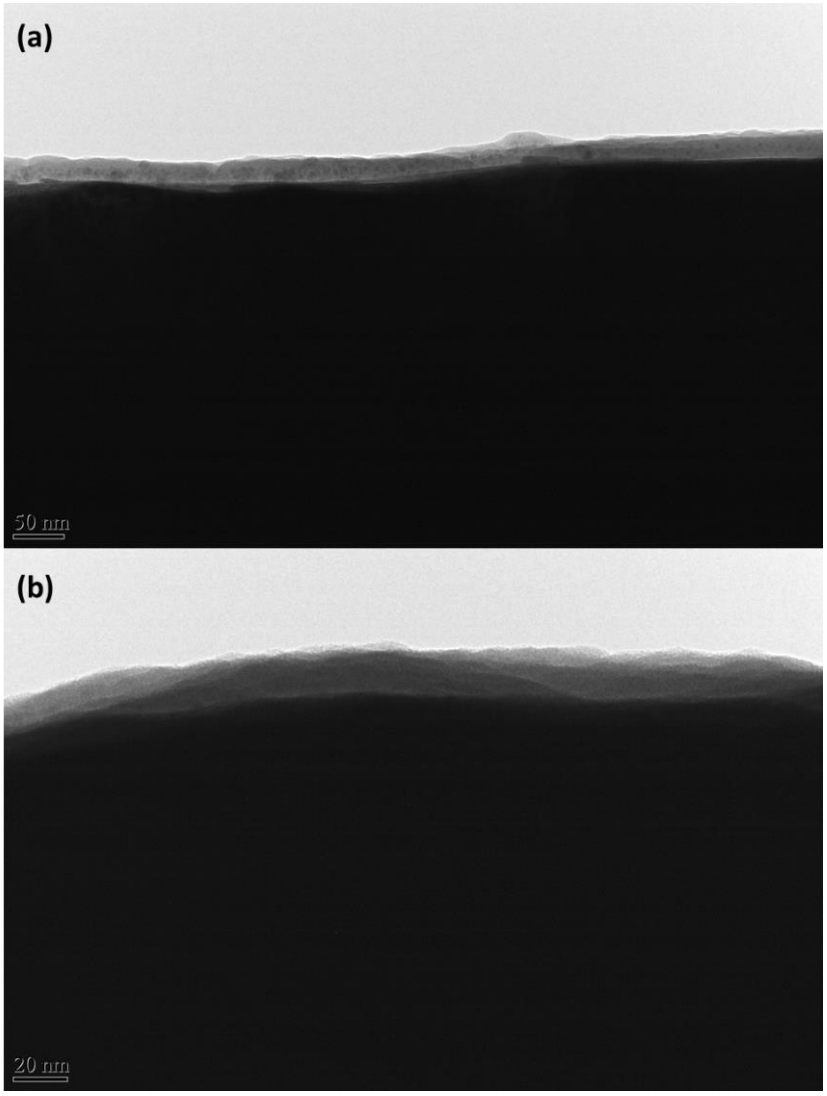

Figure 6-9 Oxide layer present at the surface of annealed 100W TaSiN coating

6.5.3 Nanoscale Morphology of TaSiN Coatings

In contrast to the TiSiN coatings discussed in the previous chapter, where individual columns consisted of many nano-scale subdomains, most columns in the TaSiN film consisted of a single FCC TaN grain. Near the left-hand side of the micrograph shown in Figure 6-10 on page 129, a column boundary is visible. To the right of this boundary, continuous lattice fringing, suggesting the presence of a single grain is

visible . There is some contrast within each individual column, possibly due to composition. This could indicate the presence of Si-rich or Ti-rich regions, as was seen in the TiSiN coatings deposited via Arc and PVD Magnetron Sputtering. As a whole the subdomains are much less readily distinguishable, as compared to those seen in the TiSiN system.

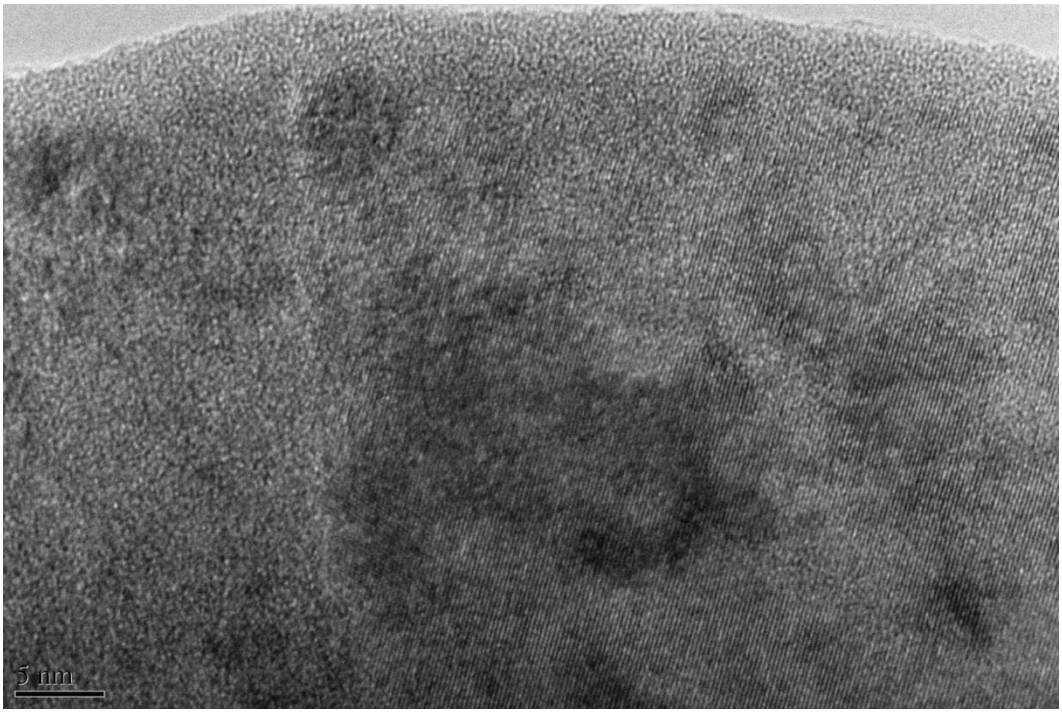

Figure 6-10 High resolution TEM micrograph showing one continuous large grain within a column, with possible subdomains indicated via compositional contrast

While the majority of the columns within the TaSiN coatings appeared to be composed of a single grain, as observed by visible lattice fringes, some regions with more division were found, although even in these regions, individual grains were difficult to distinguish. Figure 6-11 on page 130 shows one such area where subdomains within a single column are discernable from changes in direction of the lattice fringing. In

addition, bright regions, possibly comprised of amorphous content exist in regions between these sub domains.

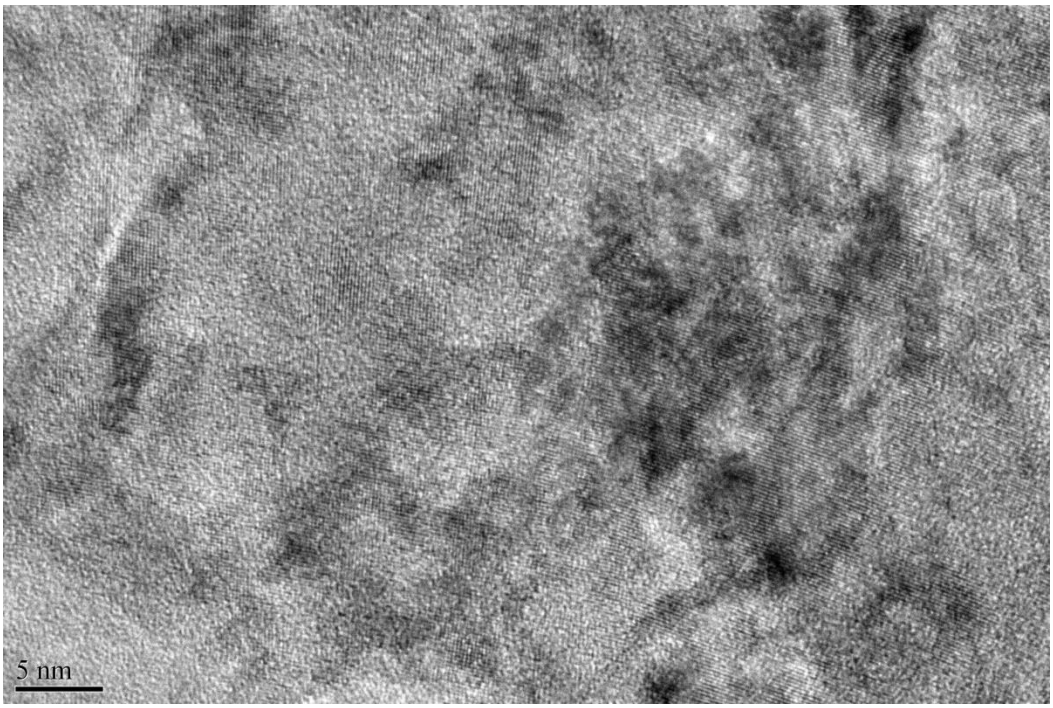

Figure 6-11 A second view of the nanoscale morphology of TaSiN coatings within a column, showing some grain boundaries and loosely defined subdomains inside the column

6.6 Ongoing and Future Work in TaN and TaSiN

In a closely related and currently ongoing project led by labmate, Anna Zaman, the relationship of deposition parameters and the TaN crystal structure obtained are being investigated in detail. In fact, preliminary results suggest that with decreasing percentage of N_2 within the gas mixture during deposition, the FCC TaN phase becomes less prominent, and a shift to harder phases such as orthorhombic and 1:1 TaN hexagonal phases come into play. In fact, coatings processed at conditions of 50 W to the Ta target, 100 V bias to the substrate, and 5% N_2 in the gas mixture showed

remarkable hardness of over 35 GPa in preliminary nanoindentation tests, although these results still need to be investigated further to confirm the exact values. High resolution, low angle XRD shows the presence of solely FCC TaN at all N_2 flows between 10% and 25%, and hardness values never exceed 25 GPa. The high hardness observed in the low Nitrogen flow film is accompanied by quite an interesting XRD result, with the formation of a broad, multiple component peak which likely contains hexagonal and orthorhombic TaN phases emerging. This can be seen (blue curve) in Figure 6-12 on page 131.

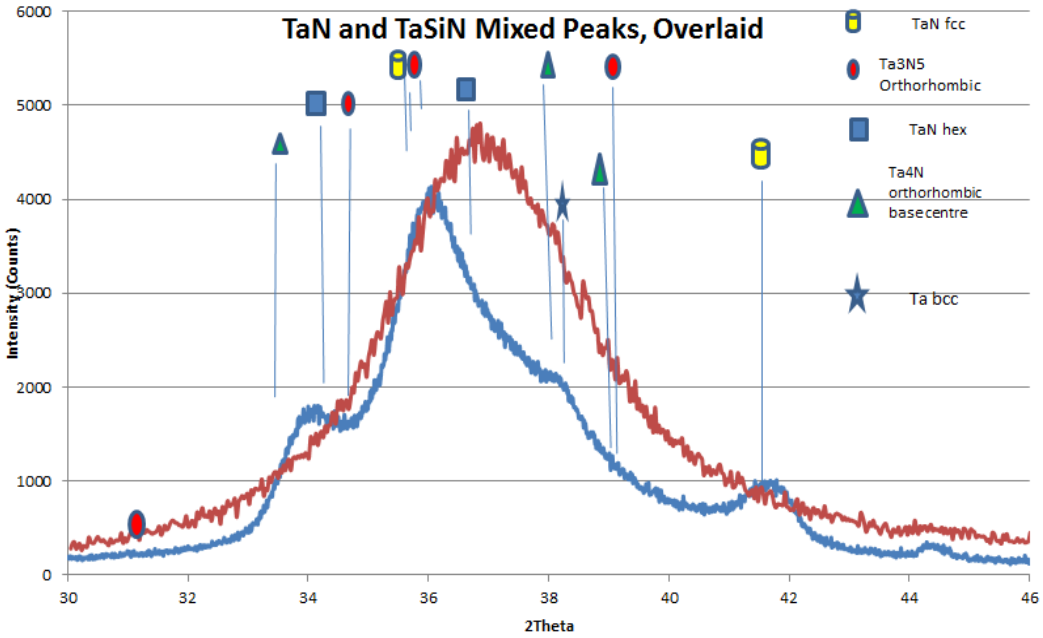

Figure 6-12 Overlaid TaN (blue) and TaSiN (red) multi-component peaks from films processed using identical conditions, with and without power to the Si target.

Based on the excellent mechanical properties of this TaN coating, a TaSiN coating was processed at identical conditions, but Si content was added to the plasma via application of 30W RF power to the Si target. Preliminary results including low angle XRD (red curve in Figure 6-11) and nanoindentation are promising, showing a broad,

likely multi-component peak located in generally the same region of the multi-component TaN peak. Preliminary nanoindentation measurements show a hardness of 33.5 GPa for this thin film. Continued work to understand the relationship between TaN crystalline phases and processing conditions will likely yield an even greater understanding of the TaN and TaSiN systems, allowing for further enhancements of both the mechanical and the oxidation properties of these coatings.

6.7 Summary of PVD Magnetron Sputtered TaSiN Coatings

While it was initially expected that the TiSiN sytem could serve as a model for other MeSiN coating systems, this was not entirely true in the case of the TaSiN system. While initial TaSiN coatings show promising results in terms of oxidation resistance to 550˚C as well as hardness enhancement of about 3.5 GPa as compared to TaN, more work is necessary on the TaSiN system in order to optimize the mechanical and thermal behaviors of the coatings.

Initial TaSiN coatings possessed FCC TaN crystal structure, and an additional FCC (TaSi)N phase was present in certain coatings, particularly under conditions of increasing deposition energies. However, as the power applied to the Ta target was greatly increased, the slightly sub-stoichiometric FCC TaN structure dominated the crystal structure of the coating once again. Increased power to the Ta target resulted in increased hardness of up to 25.5 GPa. However, increased power to the Ta target resulted in higher levels of residual stress within the coatings. In fact residual stresses became so prominent that the coatings cracked the Si wafer substrates onto which they were deposited. In addition, the hardness of the hardest TaSiN coating were severely degraded after annealing to 550˚C in ambient air, while the hardness of the coatings produced using 70 W and 100 W to the Ta target showed only minor decreases in hardness after annealing. This indicates that the incorporation of Si into both the crystal

FCC lattice, as seen in the case of the 100 W coating and into the amorphous nanostructure, as is probable in the 70 W coating, both serve to increase the resistance to oxidation as compared to the coating processed using 100 W to the Ta target.

As expected, increased power to the Ta target resulted in an increased presence of Ta within the coatings, as measured by XPS. Ta and N are sub-stoichiometric in each case, indicating the need to further explore deposition conditions in order to allow for the formation of both Tantalum Nitride and Silicon Nitride phases within the coatings. As Ta power was increased, the deposition rate of the coatings increased. Since Si power was held constant, the Si content decreased with increasing power to the Ta target, as expected.

TEM was used to explore the microstructure of the 100 W TaSiN coating before and after annealing. In general, no major differences to the morphology at the micro or the nano-scale were noted, although the presence of a (likely amorphous) oxide layer of about 20 nm thickness was observed at the surface of the oxidized sample. The TaSiN coatings consisted of columnar microstructure, with thicker, more well defined columns as compared to the previously discussed TiSiN system. While the presence of sub-domains within individual columns was observed, these subdomains were not uniform in size or shape, and were less readily distinguishable from one another than the sub grains in the TiSiN films.

Chapter 7

Conclusions

In this body of work, TiSiN coatings deposited using two different PVD methods were studied with the goal of developing an understanding between the morphology of the coatings at the nanoscale and their excellent mechanical properties. Arc deposited TiSiN showed a hardness of 29.8 and 33.6 GPa for the low and high Si content coatings, respectively. After extensive study of the relationships of bias, power to the Si target, and substrate rotation speed on the mechanical properties of TiSiN coatings processed using the in-house SaNEL Reactive PVD Magnetron Sputtering System, several coatings with excellent hardness were created, with the best having a hardness of 38.9 GPa. In both of these cases, the TiSiN coatings were columnar in microstructure, with nano-scale subgrains or subdomains consistently present throughout the columns.

Relationships between the preferred orientation of the coatings, the presence of Si incorporation into the TiN FCC crystal structure, the residual stress, and the hardness of the as-produced TiSiN coatings were discovered and explored in detail. Although three very different experimental parameters including bias voltage applied at the substrate, power to the Si target, and speed of substrate rotation were varied, common threads were consistently found between the three series. In general, it seems that even very slight changes to the energetic interactions present by way of adjusting bias, target power, or time spent in Ti and Si rich portions of the plasma have consistent effects on the material properties. It was repeatedly found that as films increased in hardness, the (200) texture of the coatings also increased, while the prominence of Si incorporation into the FCC TiN crystal lattice and the residual stresses within the films decreased, regardless of the experimental deposition condition which was varied. Based on this discovery, it seems possible that as the texturing of the coatings increases, the presence

of low angle grain boundaries increases, and therefore, the presence of high angle grain boundaries decreases. The low angle grain boundaries likely lead to decreased levels of residual stress within the coatings, which in turn affects the incorporation of Si into the FCC TiN lattice. This is supported by HRTEM examination, which showed a higher tendency of Si localization around grain boundaries in the higher rotation coatings. These same coatings also displayed a strong TiN (200) texture as well as low residual stresses, and high hardness.

When the processing conditions found to produce excellent TiSiN coatings were applied to the TaSiN system, the resulting as-deposited coatings had hardness varying between 20-25.5 GPa. The coatings showed about 3 GPa of improvement over the hardness of TaN deposited under the same conditions. Additionally, preliminary oxidation studies show promising results, with films processed using lower Ta power conditions displaying little decrease in mechanical properties after annealing in ambient air at 550˚C for 30 minutes. The morphology of the as-deposited TaSiN coatings was once again columnar, with wide, well defined columns containing subtly defined subgrains within them.

Based on an ongoing and closely related Master's Thesis project by Anna Zaman, the conditions within the SaNEL Reactive PVD Magnetron system required for the formation of other phases of TaN besides the relatively soft FCC are being explored. By applying the knowledge gained from this study on the conditions required to process TaN coatings containing the harder TaN hexagonal and Ta_3N_5 orthorhombic phases, the hardness of the preliminary as-deposited TaSiN coatings have now reached levels of approximately 33 GPa.

7.1 Arc Deposited TiSiN Coatings

The Arc deposited TiSiN coatings were found to contain a previously unidentified crystal phase, FCC (TiSi)N with Si replacing some of the Ti atoms within the crystal lattice. In these coatings, TiN and (TiSi)N FCC nanoscale crystalline regions with (200) preferred orientation are defined by lattice fringing and by grain boundaries, in some cases, presumably containing amorphous Si_3N_4 content, according to previously reported high resolution XPS. The (TiSi)N phase was not recognized in initial studies due to its close overlap with the XRD peaks from the stainless steel substrate. The θ-2θ scans previously employed lacked the low depth-sensitivity possible via low angle XRD and were unfortunately not sufficient to identify this phase. In-house low angle XRD analysis showed the presence of a peak at the location of the previously identified substrate peak at very low X-Ray incidence angles which should not allow penetration of the X-Ray into the substrate. This was an early indication of the presence of an FCC (TiSi)N phase. It's presence was later confirmed via electron diffraction of FIB TEM foils of both the low and the high Si coatings. In addition, the presence of this (TiSi)N phase was further supported by localized EDS spectra.

From examination of these coatings, some evidence of Veprek's proposed nc-TiN/a-Si_3N_4 nanocomposite structure was seen, even though the temperature of the substrate was 200˚C lower than the suggested required temperature which Veprek proposes as necessary in order to facilitate the spinodal decomposition of the TiN and the Si_3N_4 phases. However, the hardness and the TEM analysis of the coatings suggest that this relationship could be occurring, at least to some degree. This is likely made possible by the conversion of large amounts of kinetic energy by way of energetic ion bombardment being converted into localized thermal energy at the sight of coating deposition. In addition however, a more complicated relationship between the energy

presence during coating deposition, the presence of Si within the TiN crystal structure, and the mechanical properties emerged, suggesting that energetic processes may play an additional role in the incorporation of Si into the coatings, with certain conditions favoring the formation of amorphous Si_3N_4, while others quite clearly result in Si becoming embedded in the TiN crystal structure. In fact, it is found in this study that the development of the fine microstructure proposed by Veprek consisting of ~10 nm TiN grains embedded in a thin monolayer Si_3N_4 matrix is apparently quite a challenging task. This structure likely requires ideal processing conditions to allow for the required uniformity at the atomic level. Veprek's theoretical model, as well as experimental work, is based largely on TiSiN coatings processed using CVD methods. These methods typically have a much lower energy density present at the surface, which may be greatly impacting the formation of crystalline phases during thin film deposition. Thus, deposition methods employing highly energetic processes with very high deposition rates such as Arc PVD may not be completely capable of forming the fine microstructure with Si content localized solely within a monolayer boundary, instead allowing for additional Si to become embedded in the crystal lattice.

7.2 TiSiN Coatings via Reactive PVD Magnetron Sputtering

Like the Arc deposited coatings, TiSiN films created using Reactive PVD magnetron sputtering methods also contained a (TiSi)N FCC phase, with Si replacing Ti in the crystal lattice. This additional FCC phase was found in increasing prominence as bias voltage applied to the substrate was increased, but it was present in low quantities even in the lowest bias coatings. This further supports the idea that energetic interactions present due to experimental deposition conditions can strongly influence coating crystal structure, which is intimately related to other investigated coating properties including hardness and residual stress.

The effects of several deposition parameters including bias voltage applied to the substrate, power applied to the Si target, and the speed of substrate rotation during coating deposition were explored. It was found that increased bias voltage resulted in coatings with more randomly oriented crystal structure, lower hardness, and higher presence of residual stress within the coating. By varying the bias voltage, coatings varying in hardness between 18.5 and 37.1 GPa were produced. Further revisions to the deposition process including varying Si content and substrate rotation speed increased the maximum hardness attained to a value of 38.9 GPa. While the changes in mechanical properties were less dramatic as these parameters were varied as compared to the bias voltage being varied, it was found that decreased power to the Si target and decreased rotation speed of the substrate during TiSiN coating deposition resulted in coatings with less desirable mechanical properties. Ultimately, after much exploration of a variety of deposition conditions, the highest hardness coating was obtained using 150 W DC power to the Ti target, 60 W RF power to the Si target, 100 V bias applied to the substrate, 550˚C substrate temperature, 25 sccm total gas flow rate, with 25% of the mixture consisting of N_2, and the remainder being Ar, 5 mTorr working pressure, 10.5 cm distance between the targets and the substrate, and 6 RPM substrate rotation.

A consistent relationship between the crystal structure and the mechanical properties of the coatings was established across the three series of coatings. In the case of all three series in which three very different conditions were adjusted, bias to the substrate, power to the Si target, and speed of substrate rotation, similar relationships between the texturing, the localization of Si within the structure, the hardness, and the residual stress were unearthed. In each series, increased TiN (200) texturing correlated with increased hardness, decreased residual stress, and decreased prominence of the (TiSi)N FCC phase, in which Si takes the place of some of the Ti atoms within the lattice.

As texturing is increased, the orientation of the nanoscale crystalline grains within the coating becomes more uniform, and the resulting grain boundaries typically exhibit low angles between the lattice fringing of neighboring crystal structures. This in turn could reduce residual stresses present within the coatings, as well as encourage the localization of amorphous Si content into these regions, in support of Veprek's proposed model. High resolution XPS reinforces this model, showing the presence of amorphous Si_3N_4 within the 3 RPM TiSiN coating.

The morphology, as observed by HRTEM, in the Reactive PVD Magnetron sputtered TiSiN films with the most desirable mechanical properties showed many similarities to the Arc deposited coatings. Although the columns present were finer and feather-like in the Magnetron sputtered coatings as compared to the Arc coatings, subdomains of similar size were once again present within the columns. The subgrains in these films however, were in general more difficult to distinguish from each other, with the subgrain boundaries being thinner and less obvious. The coatings were textured, with both low angle XRD and TEM electron diffration showing a preferred (200) orientation. In fact, when comparing the diffraction patterns of various series of produced films, films with the (200) orientation perpendicular to the growth direction of the coating in general exhibited higher hardness than films processed under similar conditions possessing less texturing. The presence of both a high degree of texturing as well as nanoscale grain size, as estimated by XRD, suggests the presence of low angle grain boundaries. This hypothesis was confirmed by HRTEM, and reinforced by the comparatively low amounts of residual stresses present in the coatings as the hardness increased. In addition, an interesting relationship between substrate rotation speed and morphology emerged, with multilayers of Ti-rich and Si-rich components occurring, but only at low substrate rotation speeds. As rotation speed was increased, these layers lack

the time to form, and a more uniform, non-layered structure results. Although the visible effects on morphology were quite dramatic, the change in mechanical properties in the presence or absence of the multi-layered structure was not substantial.

7.3 TaSiN PVD Magnetron Sputtered Coatings

While it was expected that the sputtering of TaSiN samples could be accurately predicted by the results of the previously described TiSiN study, significant differences were observed. The sputtering rate of Tantalum was nearly three times that of Titanium. The residual stresses were also sufficiently high (5 GPa) as to fracture the Si substrate during the deposition of TaSiN, resulting in the Si wafer fracturing into thousands of tiny, powder-like fragments within the sputtering chamber. Additionally, the preferred phase of crystalline TaN using the same processing conditions as the TiSiN system was the relatively soft FCC phase. Thus, additional studies are ongoing to better understand the deposition parameters necessary for the formation of harder crystalline TaN phases, such as the orthorhombic and stoichiometric hexagonal structures.

To account for differences in Ti and Ta deposition rates, the power to the Ta target was adjusted in order to more closely mimic the deposition rate of the Ti target during the previously discussed TiSiN experiments. Increased power to the Ta target resulted in increased hardness, but it also increased the residual stress present in the coating. In fact, residual stresses were so high that coatings could only be deposited on small fragments of Si wafer in order to avoid fracture after extreme curvature of the Si wafer due to coating residual stresses. Because of the small substrate size, tribological wear testing was impossible.

The crystal structure found within the TaSiN coatings consisted solely of FCC TaN. In the coating processed using the highest power to the Ta target, the peaks are greatly broadened compared to the coatings deposited using lower power to the Ta

target. While some of this broadening is likely due to nano-scale grain size, it may also be due in part to the high residual stresses present in the coating, as well as a possible mixture of Ta:N stoichiometry within the FCC TaN crystal structure due to the excess content of Ta, as measured by XPS within this particular coating. In the coating created using 100W power to the Ta target, an additional (TaSi)N FCC Crystal structure existed, with a lattice parameter approximately 6% smaller than FCC TaN due to replacement of Ta atoms by smaller Si atoms within the crystal lattice. The coating created using the lowest power to the Ta target consisted of FCC TaN only. Little difference was noticed in the crystal structure before and after annealing, indicating that no additional crystalline phases were formed due to film oxidation after heat treatment in air.

The microstructure observed in the TaSiN coatings, as observed via TEM, was columnar, with loosely defined sub-domains present within individual columns. Columns were larger in diameter than the previously investigated TiSiN coatings, and their boundaries were more clearly defined. The opposite was true of the sub-domains present within the columns, however. In a typical column, lattice fringing was continuous across the majority of the column, with possible sub-domains distinguishable by way of lighter and darker areas, presumably due to compositional contrast. In rarer cases, some grain boundaries could be distinguished as lighter areas lacking lattice fringing located immediately adjacent to crystalline regions. These grain boundaries did not typically connect to form distinct grains, however. Instead, the grain boundaries served to distinguish loosely defined sub-domains at the nano-scale.

In an ongoing and closely related project of SaNEL by Anna Zaman, it has been found that a decrease in the Nitrogen flow rate, accompanied by a further reduction in the power applied to the Ta target has the capability to induce the formation of some harder crystalline phases of TaN including hexagonal TaN and orthorhombic Ta_3N_5. In turn,

these findings were applied to the TaSiN system, and coatings hardness has been preliminarily measured at values of above 33 GPa.

7.4 Conclusions

Through the exploration of two different MeSiN thin film nanocomposite systems synthesized using two different methods of physical vapor deposition, a deeper understanding of the relationship between the microstructure and the mechanical properties of the films was obtained. Based on the knowledge gained, coatings with hardness as high as 38.9 GPa were produced in-house. While all films studied in this body of work exhibited columnar nanostructure, deposition parameters had a great effect on the width and definition of the columns. In general, hardness enhancement occurred as the column diameter became smaller and as the columns became more feather-like with less clearly defined boundaries, but still maintained their high density and presence through the thickness of the coating.

The presence of smaller, nano-scale sub-grains or sub-domains was consistently noted through the course of this study. Based on TEM analysis of the Arc TiSiN Low and High Si coatings, as well as the varying rotation TiSiN PVD Magnetron sputtered series, more highly defined sub-grains within the columns resulted in enhancement of the mechanical properties. Coatings which exhibited grains distinguishable via lattice fringing of compositional contrast only consistently displayed lower hardness than coatings with grain boundaries clearly visible via TEM.

While initial TaSiN coatings were lower in hardness than first expected, the system can be further manipulated, with experimental conditions selected in part via the use of the TiSiN body of work as a model system and additional information drawn from a closely related project on the effects of deposition parameters on the crystal structure of TaN. In this way, it is expected that the morphology and the mechanical properties of this

coating material, as well as other MeSiN coating materials, can be further refined in order to create a thin film nanocomposite material exhibiting both high hardness and excellent resistance to oxidation.

References

1. Zhang, R.F. and S. Veprek, *Phase stabilities of self-organized nc-TiN/a-Si(3)N(4) nanocomposites and of Ti(1-x)S(x)N(y) solid solutions studied by ab initio calculation and thermodynamic modeling.* Thin Solid Films, 2008. **516**(8): p. 2264-2275.
2. Veprek-Heijman, M.G.J., et al., *Non-linear finite element constitutive modeling of indentation into super- and ultrahard materials: The plastic deformation of the diamond tip and the ratio of hardness to tensile yield strength of super- and ultrahard nanocomposites.* Surface & Coatings Technology, 2009. **203**(22): p. 3385-3391.
3. Veprek, S., et al., *Superhard nanocomposites: Origin of hardness enhancement, properties and applications.* Surface & Coatings Technology, 2010. **204**(12-13): p. 1898-1906.
4. Veprek, S., et al., *Search for Ultrahard Materials and Recent Progress in the Understanding of Hardness Enhancement and Properties of Nanocomposites.* Nanostructured Materials, Thin Films and Hard Coatings for Advanced Applications, 2010. **159**: p. 1-10.
5. Veprek, S., M.G.J. Veprek-Heijman, and R.F. Zhang, *Chemistry, physics and fracture mechanics in search for superhard materials, and the origin of superhardness in nc-TiN/a-Si3N4 and related nanocomposites.* Journal of Physics and Chemistry of Solids, 2007. **68**(5-6): p. 1161-1168.
6. Veprek, S. and M.G.J. Veprek-Heijman, *The formation and role of interfaces in superhard nc-MenN/a-Si3N4 nanocomposites.* Surface & Coatings Technology, 2007. **201**(13): p. 6064-6070.
7. Veprek, S., et al., *Conditions required for achieving superhardness of >= 45 GPa in nc-TiN/a-Si3N4 nanocomposites.* Materials Science and Engineering a-Structural Materials Properties Microstructure and Processing, 2004. **384**(1-2): p. 102-116.
8. Veprek, S., S.G. Prilliman, and S.M. Clark, *Elastic moduli of nc-TiN/a-Si3N4 nanocomposites: Compressible, yet superhard.* Journal of Physics and Chemistry of Solids, 2010. **71**(8): p. 1175-1178.
9. Veprek, S., et al., *Nanocomposites nc-TiN/a-Si3N4/a- and nc-TiSi2 with hardness exceeding 100 GPa and high fracture toughness.* Nanophase and Nanocomposite Materials Iii, 2000. **581**: p. 321-326.
10. Zhang, R.F., A.S. Argon, and S. Veprek, *Friedel Oscillations are Limiting the Strength of Superhard Nanocomposites and Heterostructures.* Physical Review Letters, 2009. **102**(1).
11. Veprek, S., et al., *Different approaches to superhard coatings and nanocomposites.* Thin Solid Films, 2005. **476**(1): p. 1-29.
12. Veprek, S., A.S. Argon, and R.F. Zhang, *Origin of the hardness enhancement in superhard nc-TiN/a-Si3N4 and ultrahard nc-TiN/a-Si3N4/TiSi2 nanocomposites.* Philosophical Magazine Letters, 2007. **87**(12): p. 955-966.
13. Veprek, S., *The origin of superhardness in TiN/Si3N4 nanocomposites: the role of the interfacial monolayer.* High Pressure Research, 2006. **26**(2): p. 119-125.
14. Musil, J., J. Vlcek, and P. Zeman, *Hard amorphous nanocomposite coatings with oxidation resistance above 1000 degrees C.* Advances in Applied Ceramics, 2008. **107**(3): p. 148-154.

15. Zeman, P., J. Musil, and R. Daniel, *High-temperature oxidation resistance of Ta-Si-N films with a high Si content.* Surface & Coatings Technology, 2006. **200**(12-13): p. 4091-4096.
16. Zeman, H., J. Musil, and P. Zeman, *Physical and mechanical properties of sputtered Ta-Si-N films with a high (>= 40 at %) content of Si.* Journal of Vacuum Science & Technology A, 2004. **22**(3): p. 646-649.
17. Olowolafe, J.O., et al., *Effect of composition on thermal stability and electrical resistivity of Ta-Si-N films.* Thin Solid Films, 2000. **365**(1): p. 19-21.
18. Chung, C.K. and P.J. Su, *Material characterization and nanohardness measurement of nanostructured Ta-Si-N film.* Surface & Coatings Technology, 2004. **188**: p. 420-424.
19. Chung, C.K., A. Nautiyal, and T.S. Chen, *Low-temperature resistivity and microstructure of reactive magnetron co-sputtered Ta-Si-N thin films.* Journal of Physics D-Applied Physics, 2010. **43**(29).
20. Musil, J. and P. Zeman, *Hard a-Si3N4/MeNx nanocomposite coatings with high thermal stability and high oxidation resistance.* Designing of Interfacial Structures in Advanced Materials and their Joints, 2007. **127**: p. 31-36.
21. Veprek, S., *Recent Research for new superhard materials: Go nano!* J. Vac. Sci. Technol. A, 2013. **31**(5).
22. Veprek, S., *The search for novel, superhard materials.* Journal of Vacuum Science & Technology A, 1999. **17**(5): p. 2401-2420.
23. Veprek, S. and A.S. Argon, *Mechanical properties of superhard nanocomposites.* Surface & Coatings Technology, 2001. **146**: p. 175-182.
24. Hauert, R. and J. Patscheider, *From alloying to nanocomposites - Improved performance of hard coatings.* Advanced Engineering Materials, 2000. **2**(5): p. 247-259.
25. Zhang, R.F. and S. Veprek, *Metastable phases and spinodal decomposition in Ti(1-x)Al(x)N system studied by ab initio and thermodynamic modeling, a comparison with the TiN-Si(3)N(4) system.* Materials Science and Engineering a-Structural Materials Properties Microstructure and Processing, 2007. **448**(1-2): p. 111-119.
26. Zeman, P., et al., *Structure and properties of hard and superhard Zr-Cu-N nanocomposite coatings.* Materials Science and Engineering a-Structural Materials Properties Microstructure and Processing, 2000. **289**(1-2): p. 189-197.
27. Veprek, S., et al., *Different mechanisms leading to superhard coatings: Stable nanocomposites and high biaxial compressive stress.* Surface Engineering 2001 - Fundamentals and Applications, 2001. **697**: p. 27-32.
28. Musil, J., et al., *Hard and superhard nanocomposite Al-Cu-N films prepared by magnetron sputtering.* Surface & Coatings Technology, 2001. **142**: p. 603-609.
29. Carvalho, S., et al., *PVD grown (Ti,Si,Al)N nanocomposite coatings and (Ti,Al)N/(Ti,Si)N multilayers: structural and mechanical properties.* Surface & Coatings Technology, 2003. **172**(2-3): p. 109-116.
30. Prilliman, S.G., et al., *Strain and deformation in ultra-hard nanocomposites nc-TiN/a-BN under hydrostatic pressure.* Materials Science and Engineering a-Structural Materials Properties Microstructure and Processing, 2006. **437**(2): p. 379-387.
31. Zhang, R.F. and S. Veprek, *Phase stabilities and spinodal decomposition in the Cr1-xAlxN system studied by ab initio LDA and thermodynamic modeling: Comparison with the Ti1-xAlxN and TiN/Si3N4 systems.* Acta Materialia, 2007. **55**(14): p. 4615-4624.

32. Sheng, S.H., R.F. Zhang, and S. Veprek, *Study of spinodal decomposition and formation of nc-Al2O3/ZrO2 nanocomposites by combined ab initio density functional theory and thermodynamic modeling.* Acta Materialia, 2011. **59**(9): p. 3498-3509.
33. Ivashchenko, V.I., et al., *First-principles study of TiN/SiC/TiN interfaces in superhard nanocomposites.* Physical Review B, 2012. **86**(1).
34. Konca, E., et al., *Transfer of 319 Al alloy to titanium diboride and titanium nitride based (TiAlN, TiCN, TiN) coatings: effects of sliding speed, temperature and environment.* Surface & Coatings Technology, 2005. **200**(7): p. 2260-2270.
35. Cheng, Y. and Y.F. Zheng, *Characterization of TiN, TiC and TiCN coatings on Ti-50.6 at.% Ni alloy deposited by PIII and deposition technique.* Surface & Coatings Technology, 2007. **201**(9-11): p. 4909-4912.
36. Cheng, Y.H., T. Browne, and B. Heckerman, *Influence of CH4 fraction on the composition, structure, and internal stress of the TiCN coatings deposited by LAFAD technique.* Vacuum, 2010. **85**(1): p. 89-94.
37. Cheng, Y.H., T. Browne, and B. Heckerman, *TiCN coatings deposited by large area filtered arc deposition technique.* Journal of Vacuum Science & Technology A, 2010. **28**(3): p. 431-437.
38. Musil, J., et al., *Relationships between hardness, Young's modulus and elastic recovery in hard nanocomposite coatings.* Surface & Coatings Technology, 2002. **154**(2-3): p. 304-313.
39. Musil, J., et al., *Hard nanocomposite coatings prepared by magnetron sputtering.* Advanced Materials Forum I, 2002. **230-2**: p. 613-622.
40. Musil, J., et al., *ZrN/Cu nanocomposite film - a novel superhard material.* Surface & Coatings Technology, 1999. **120**: p. 179-183.
41. Dawson, P.T. and S.A.J. Stazyk, *The Preparation and Characterization of Transition-Metal Nitride Films.* Journal of Vacuum Science & Technology, 1982. **20**(4): p. 966-967.
42. Fix, R.M., R.G. Gordon, and D.M. Hoffman, *Synthesis of Early Transition-Metal Nitride Thin-Films by Apcvd.* Abstracts of Papers of the American Chemical Society, 1989. **197**: p. 374-INOR.
43. Holl, M.M.B., R.L. Laduca, and P.T. Wolczanski, *Early Transition-Metal Nitride Complexes and Their Relation to Solid-State Nitrides.* Abstracts of Papers of the American Chemical Society, 1990. **200**: p. 327-INOR.
44. Nose, M., et al., *Influence of Si content and sputtering condition on the microstructure and mechanical properties of r.f.-sputtered transition metal nitride films.* Electron Microscopy: Its Role in Materials Science, 2003: p. 149-156.
45. Sarakinos, K., et al., *Structural factors determining the nanomechanical performance of transition metal nitride films.* Surface Engineering 2004 - Fundamentals and Applications, 2005. **843**: p. 311-316.
46. Cheng, Y.H., T. Browne, and B. Heckerman, *Nanocomposite TiSiN coatings deposited by large area filtered arc deposition.* Journal of Vacuum Science & Technology A, 2009. **27**(1): p. 82-88.
47. Pogrebnjak, A.D., et al., *Structures and properties of hard and superhard nanocomposite coatings.* Physics-Uspekhi, 2009. **52**(1): p. 29-54.
48. Prochazka, J., et al., *Conditions required for achieving superhardness of >= 45 GPa in nc-TiN/a-Si3N4 nanocomposites.* Materials Science and Engineering a-Structural Materials Properties Microstructure and Processing, 2004. **384**(1-2): p. 102-116.

49. Schwaller, P., et al., *Nanocomposite hard coatings: Deposition issues and validation of their mechanical properties.* Advanced Engineering Materials, 2005. **7**(5): p. 318-322.
50. Veprek, S. and S. Reiprich, *A concept for the design of novel superhard coatings.* Thin Solid Films, 1995. **268**(1-2): p. 64-71.
51. Veprek, S., S. Reiprich, and S.H. Li, *Superhard Nanocrystalline Composite-Materials - the Tin/Si3n4 System.* Applied Physics Letters, 1995. **66**(20): p. 2640-2642.
52. Veprek, S. and A.S. Argon, *Towards the understanding of mechanical properties of super- and ultrahard nanocomposites.* Journal of Vacuum Science & Technology B, 2002. **20**(2): p. 650-664.
53. Hao, S.Q., B. Delley, and C. Stampfl, *Role of oxygen in TiN(111)/SixNy/TiN(111) interfaces: Implications for superhard nanocrystalline nc-TiN/a-Si3N4 nanocomposites.* Physical Review B, 2006. **74**(3): p. -.
54. Thornton, J.A., *Influence of Apparatus Geometry and Deposition Conditions on Structure and Topography of Thick Sputtered Coatings.* Journal of Vacuum Science & Technology, 1974. **11**(4): p. 666-670.
55. Thornton, J.A., *High-Rate Thick-Film Growth.* Annual Review of Materials Science, 1977. **7**: p. 239-260.
56. Zhang, R.F. and S. Veprek, *On the spinodal nature of the phase segregation and formation of stable nanostructure in the Ti-Si-N system.* Materials Science and Engineering a-Structural Materials Properties Microstructure and Processing, 2006. **424**(1-2): p. 128-137.
57. Kim, K.H., et al., *Synthesis and mechanical evaluation of nanocomposite coating layer of nc-TiN/a-Si3N4 on SKD 11 steel by sputtering.* Journal of Materials Processing Technology, 2002. **130**: p. 283-288.
58. Kim, K.H., S.H. Kim, and J.K. Kim, *Influence of deposition conditions on the microstructure and mechanical properties of Ti-Si-N films by DC reactive magnetron sputtering.* Thin Solid Films, 2002. **420**: p. 360-365.
59. Nose, M., et al., *Influence of sputtering conditions on the structure and properties of Ti-Si-N thin films prepared by r.f.-reactive sputtering.* Surface & Coatings Technology, 2003. **174**: p. 261-265.
60. Cheng, Y.H., et al., *Influence of Si content on the structure and internal stress of the nanocomposite TiSiN coatings deposited by large area filtered arc deposition.* Journal of Physics D-Applied Physics, 2009. **42**(12).
61. Tjong, S.C. and H. Chen, *Nanocrystalline materials and coatings.* Materials Science & Engineering R-Reports, 2004. **45**(1-2): p. 1-88.
62. Kim, S.H., J.K. Kim, and K.H. Kim, *Influence of deposition conditions on the microstructure and mechanical properties of Ti-Si-N films by DC reactive magnetron sputtering.* Thin Solid Films, 2002. **420**: p. 360-365.
63. Cheng, Y.H., et al., *Mechanical and tribological properties of nanocomposite TiSiN coatings.* Surface & Coatings Technology, 2010. **204**(14): p. 2123-2129.
64. Cheng, Y.H., et al., *Internal stresses in TiN/Ti multilayer coatings deposited by large area filtered arc deposition.* Journal of Applied Physics, 2008. **104**(093502).
65. Ee, Y.C., et al., *Barrier property of TiSiN films formed by low frequency, high density inductively coupled plasma process.* Surface & Coatings Technology, 2005. **198**(1-3): p. 291-295.
66. Chung, C.K., et al., *Thermal stability of Ta-Si-N nanocomposite thin films at different nitrogen flow ratios.* Surface & Coatings Technology, 2006. **201**(7): p. 3947-3952.

67. Chung, C.K., et al., *Effect of the target shuttering on the characteristics of the Ta-Si-N thin films by reactive magnetron co-sputtering.* Surface & Coatings Technology, 2009. **204**(6-7): p. 1071-1075.
68. Chung, C.K. and P.J. Su, *Material characterization and nanohardness measurement of nanostructured Ta-Si-N film.* Surface & Coatings Technology, 2004. **188-89**: p. 420-424.
69. Chung, C.K., et al., *Fabrication and characterization of nanostructured Ta-Si-N films.* 2007 2nd IEEE International Conference on Nano/Micro Engineered and Molecular Systems, Vols 1-3, 2007: p. 10-131214.
70. Valleti, K., et al., *Studies on phase dependent mechanical properties of dc magnetron sputtered TaN thin films: evaluation of super hardness in orthorhombic Ta(4)N phase.* Journal of Physics D-Applied Physics, 2008. **41**(4).
71. Liu, X., et al., *Effect of deposition and annealing temperature on mechanical properties of TaN film.* Applied Surface Science, 2011. **258**(3): p. 1033-1037.
72. Bunshah, R.F., *Handbook of deposition technologies for films and coatings : science, technology, and applications*. 2nd ed. Materials science and process technology series. Electronic materials and process technology. 1994, Park Ridge, N.J.: Noyes Publications. xxvi, 861 p.
73. Rickerby, D.S. and A. Matthews, *Advanced surface coatings : a handbook of surface engineering*. 1991, Glasgow New York: Blackie ;Chapman and Hall. xiii, 368 p.
74. Logothetidis, S., E.I. Meletis, and G. Kourouklis, *New approach in the monitoring and characterization of titanium nitride thin films.* Journal of Materials Research, 1999. **14**(2): p. 436-441.
75. Hultman, L., *Thermal stability of nitride thin films.* Vacuum, 2000. **57**(1): p. 1-30.
76. Hao, S.Q., B. Delley, and C. Stampfl, *Role of oxygen in TiN(111)/SixNy/TiN(111) interfaces: Implications for superhard nanocrystalline nc-TiN/a-Si3N4 nanocomposites.* Physical Review B, 2006. **74**(3).
77. Hao, S.Q., et al., *Superhard nitride-based nanocomposites: Role of interfaces and effect of impurities.* Physical Review Letters, 2006. **97**(8).
78. Ivashchenko, V.I., et al., *Comparative first-principles study of TiN/SiNx/TiN interfaces.* Physical Review B, 2012. **85**(19).
79. Veprek, S. and A.S. Argon, *Mechanical properties of superhard nanocomposites with high thermal stability.* Mechanical Properties of Nanostructured Materials and Nanocomposites, 2004. **791**: p. 25-30.
80. Moto, K., T. Boom, and S. Veprek, *The role of nc-TiN surface coverage by a-Si3N4 for the control of room temperature and in-dry-air oxidation resistance of nc-TiN/a-Si3N4/a- and nc-TiSi2 nanocomposites.* Advanced Materials Processing Ii, 2003. **437-4**: p. 403-406.
81. Veprek, S., *Superhard nanocomposites: design concept, properties, present and future industrial applications.* European Physical Journal-Applied Physics, 2004. **28**(3): p. 313-317.
82. Veprek, S., *Reproducibility of deposition and industrial applications of stable superhard nanocomposites.* Transactions of Nonferrous Metals Society of China, 2004. **14**: p. 19-24.
83. Ribeiro, E., et al., *Characterization of hard DC-sputtered Si-based TiN coatings: the effect of composition and ion bombardment.* Surface & Coatings Technology, 2004. **188**: p. 351-357.
84. Vaz, F., et al., *Young's modulus of (Ti,Si)N films by surface acoustic waves and indentation techniques.* Thin Solid Films, 2002. **408**(1-2): p. 160-168.

85. Vaz, F. and L. Rebouta, *Superhard nanocomposite Ti-Si-N coatings.* Nitrides and Oxynitrides 2, 2002. **383**: p. 143-149.
86. Niederhofer, A., et al., *The role of percolation threshold for the control of the hardness and thermal stability of super- and ultrahard nanocomposites.* Surface & Coatings Technology, 2001. **146**: p. 183-188.
87. Ali, M., et al., *Effect of cathodic arc PVD parameters on roughness of TiN coating on steel substrate.* Current Applied Physics, 2010. **10**(2): p. 471-474.
88. Veprek, S., et al., *Degradation of superhard nanocomposites by built-in impurities.* Journal of Vacuum Science & Technology B, 2004. **22**(2): p. L5-L9.
89. Veprek, S., P. Karvankova, and M.G.J. Veprek-Heijman, *Possible role of oxygen impurities in degradation of nc-TiN/a-Si3N4 nanocomposites.* Journal of Vacuum Science & Technology B, 2005. **23**(6): p. L17-L21.
90. Veprek, S., et al., *The issue of the reproducibility of deposition of superhard nanocomposites with hardness of >= 50 GPa.* Surface & Coatings Technology, 2006. **200**(12-13): p. 3876-3885.
91. Veprek, S. and M.G.J. Veprek-Heijman, *Limits to the preparation of superhard nanocomposites: Impurities, deposition and annealing temperature.* Thin Solid Films, 2012. **522**: p. 274-282.
92. Adjaottor, A.A., et al., *Effect of substrate bias on sputter-deposited TiCx, TiNy and TiCxNy thin films.* Surface & Coatings Technology, 1995. **76**(1-3): p. 142-148.
93. Ali, M., E. Hamzah, and M.R. Toff, *Friction coefficient and surface roughness of TiN-coated HSS deposited using cathodic arc evaporation PVD technique.* Industrial Lubrication and Tribology, 2008. **60**(2-3): p. 121-130.
94. Veprek, S., *Recent progress in superdhard nanocomposites: Preparation, properties and industrial applications.* Nanostructured Thin Films and Nanodispersion Strengthened Coatings, 2004. **155**: p. 23-34.
95. Riekkinen, T., et al., *Reactive sputter deposition and properties of TaxN thin films.* Microelectronic Engineering, 2002. **64**(1-4): p. 289-297.

Biographical Information

Jessica Mooney completed a Bachelor of Science in Biomedical Engineering at Texas A&M University in 2009. She focused on the materials track within Biomedical Engineering, and she had over two years of experience as an undergraduate researcher in the field of Single Walled Carbon Nanotube (SWNT) reinforced polymer thin film materials for electroactive applications, working with Dr. Zoubeida Ounaies.

In 2010, Jessica joined the University of Texas at Arlington's BS to Ph.D. Program, and began research with Dr. Efstathios I. Meletis's Surface and Nano Engineering Laboratory studying High Temperature, High Hardness Materials with a focus in Transition Metal Silicon Nitride Coatings. In 2011, She presented at the ICMCTF International Conference in San Diego. She attended and presented at the LSAMP National Science Foundation's National Joint Annual Meeting in 2012, and she presented her research at the Texas Society for Microscopy Conference in Grapevine, TX in 2013. In addition, her research was presented as a poster by Dr. E. I. Meletis at the International IC4N Conference in Greece. Jessica's research was supported by the National Science Foundation's Louis Stokes Alliance for Minority Participation from 2010-2012.

During her graduate education, Jessica completed two internships with Alcon Laboratories, a Novartis Company, in Fort Worth, Texas. She worked in the Research & Development of IOLs, implantable lenses for use after cataract surgery. In January of 2014, she will begin a full time job as a process engineer in IOL R&D working on polymer materials science and accommodative IOLs at Alcon.